Winter 2015

Novel techniques for quasi three-dimensional nanofabrication of Transformation Optics devices

Paul R. West
Purdue University

Recommended Citation

West, Paul R., "Novel techniques for quasi three-dimensional nanofabrication of Transformation Optics devices" (2015). *Open Access Dissertations*. 591.
https://docs.lib.purdue.edu/open_access_dissertations/591

Graduate School Form 30
(Revised 08/14)

PURDUE UNIVERSITY
GRADUATE SCHOOL
Thesis/Dissertation Acceptance

This is to certify that the thesis/dissertation prepared

By Paul R. West

Entitled

NOVEL TECHNIQUES FOR QUASI THREE-DIMENSIONAL NANOFABRICATION OF TRANSFORMATION OPTICS DEVICES

For the degree of Doctor of Philosophy

Is approved by the final examining committee:

Alexandra Boltasseva	Vladimir Shalaev
Alexander Kildishev	Minghao Qi
Xianfan Xu	

To the best of my knowledge and as understood by the student in the Thesis/Dissertation Agreement, Publication Delay, and Certification/Disclaimer (Graduate School Form 32), this thesis/dissertation adheres to the provisions of Purdue University's "Policy on Integrity in Research" and the use of copyrighted material.

Approved by Major Professor(s): Alexandra Boltasseva

Approved by: Venkataramanan Balakrishnan 01/15/2015

Head of the Department Graduate Program Date

NOVEL TECHNIQUES
FOR
QUASI THREE-DIMENSIONAL NANOFABRICATION
OF
TRANSFORMATION OPTICS DEVICES

A Dissertation

Submitted to the Faculty

of

Purdue University

by

Paul R. West

In Partial Fulfillment of the

Requirements for the Degree

of

Doctor of Philosophy

May 2015

Purdue University

West Lafayette, Indiana

I dedicate this thesis to my parents, Rob and Jan, for providing their support, and every opportunity for my education.

ACKNOWLEDGMENTS

I would like to start by acknowledging some of the people, without who none of this work would have been possible.

Sasha, six years ago we both came to Purdue with empty lab space and empty offices. It's amazing to look back on how far we have come in just the last few years, and it makes me proud to have been a part of our research group. Thank you for giving me the freedom to explore my ideas and chase my curiosities in research. Your kindness and encouraging presence helped me through graduate schools most grueling days. Thank you for giving me the opportunity to help teach your classes and summer programs. I learned so much more than science and research in graduate school, and I owe so much of that to you.

Vlad, you pushed us to focus on the grand challenges, the breakthroughs that would make a difference. I could work hard with the knowledge that our projects would have a huge impact in the field - looking back on it, you were absolutely right! You also taught us that there is a human aspect of our research the relationships between people are worth even more. You helped me realize I could do more than I thought I was capable of, and my respect for you made me want to live up to your expectations.

Alex, when I was looking back through the slides for my final defense, I realized that your impact could be seen on nearly every slide. Whether it was an idea you had, a simulation you taught me to do, or just giving me feedback on my presentation your help was so important to my work, and I really dont know how I could have done it without you. Your courage and perseverance inspired me to fight on and keep working, even when times were tough. When I would be struggling with a difficult problem, it was always such a relief when you would come by the office to ask how research was going, or just how I was doing. Not every graduate student has a mentor

who not only helps, but really cares about their students, and I am so glad to have had someone like you.

I would like to thank my family, for providing me the support, and opportunities I needed to succeed. My parents, who pushed me to always do my best and kept me in school. My three sisters: Erin, Elaine, and Adrienne - it's not easy following in the footsteps of three such successful siblings, but I'm trying to keep up!

Natalie van Hoose, thank you for all your patience, help, and support during our time at Purdue - I couldn't have done it without you. Most of all, thank you for teaching me to see with a new light, challenging me to think in new ways, and showing me how to become a better person.

Finally, I would like to thank all of my past and present group members with whom I spent the majority of my last six years. I learned so much from every one of you. Not only did you help me with research topics, but you provided a great environment in which to thrive. Outside of work, I have developed close friendships with many of you. Thank you for being there for me - you have been my home away from home while at Purdue.

TABLE OF CONTENTS

Page

LIST OF TABLES

LIST OF FIGURES

Figure Page

SYMBOLS

m	mass
c	velocity of light
c_0	velocity of light in free space
ϵ	complex permittivity of a material
ϵ'	real part of the complex electric permittivity of a material
ϵ"	imaginary (lossy) part of the complex electric permittivity of material
μ	material's magnetic permeability

ABBREVIATIONS

AFM	Atomic Force Microscope
AZO	Aluminum doped Zinc Oxide
CMOS	Complimentary Metal Oxide Semiconductor
DSP	Double-Side Polished (silicon wafer)
EBL	Electron Beam Lithography
EM	Electromagnetic
FDTD	Finite Difference Time Domain
FEM	Finite Element Method
FESEM	Field Emission Scanning Electron Microscope
FIB	Focused Ion Beam
GLAD	Glancing Angle Deposition
GRIN	Graded Index
GZO	Gallium doped Zinc Oxide
HMM	Hyperbolic Metamaterial
HSQ	Hydrogen Silsesquioxane
IR	Infrared
ITO	Indium Tin Oxide
LRSPP	Long Range Surface Plasmon Polariton
LSPR	Localized Surface Plasmon Resonance
MDC	Metal Dielectric Composite
NIR	Near Infrared
NSOM	Near-Field Scanning Optical Microscopy
PDOS	Photonic Density of States
QCM	Quartz Crystal Monitor

RIE	Reactive Ion Etching
RPM	Revolutions Per Minute
SEM	Scanning Electron Microscope (refers to FESEM)
SERS	Surface Enhanced Raman Spectroscopy
SPP	Surface Plasmon Polariton
TO	Transformation Optics
UV	Ultraviolet

ABSTRACT

West, Paul R. Ph.D., Purdue University, May 2015. Novel Techniques for Quasi Three-Dimensional Nanofabrication of Transformation Optics Devices. Major Professor: Alexandra E. Boltasseva.

Current nanofabrication is almost exclusively limited to top-down, two-dimensional techniques. As technology moves more deeply into the nano-scale regime, fabrication of new devices with quasi three-dimensional geometries shows great potential. One excellent example of an emerging field that requires this type of non-conformal 3D fabrication technique is the field of “Transformation Optics. This field involves transforming and manipulating the optical space through which light propagates. Arbitrarily manipulating the optical space requires advanced fabrication techniques, which are not possible with current two-dimensional fabrication technologies. One step toward quasi three-dimensional nanofabrication involves employing angled deposition allowing new growth mechanisms, and enabling a new realm of quasi three-dimensional fabrication.

Transformation optics also has potential for having a huge impact on one of the most fundamental and impactful aspects of optics - the capability of fully controlling and manipulating the phase of light. For this purpose, dielectric metamaterial arrays can be fabricated, altering the phase of light transmitted through the structures, while maintaining a high transmittance (low reflection). By fabricating these structures with a high-index material (such as silicon), a large gradient in phase can be implemented by adjusting the material’s effective filling fraction. Using these dielectric metamaterial arrays, anomalous refraction and focusing is demonstrated in films with thicknesses less than one wavelength.

1. PLASMONIC MATERIALS - CHALLENGES AND APPROACHES

The field of Transformation Optics allows for a strong manipulation of an optical wave as it passes through an artificially created material. In order to have this strong control over an incident field, many devices require metallic components (with negative permittivity) to have complete control over the material's permittivity. The study of a wave's behavior with these metals, (known as plasmonics), is a research area merging the fields of optics and nanoelectronics by confining light with relatively large free-space wavelength to the nanometer scale - thereby enabling a family of novel devices. Current plasmonic devices at telecommunication and optical frequencies face significant challenges due to losses encountered in the constituent plasmonic materials. These large losses seriously limit the practicality of these metals for many novel applications. Research in materials plays an important role in transforming ideas into next-generation electrical and plasmonic technologies. Currently, plasmonic and metamaterial devices have a lack of feasible materials (especially metals), required to realize useful devices While current plasmonic technologies primarily rely on silver and gold, there are many other materials that exhibit metallic properties and provide advantages in device performance, design flexibility, fabrication, integration, and tunability. This paper provides an overview of alternative plasmonic materials along with motivation for each material choice and important aspects of fabrication. A comparative study of various materials including metals, metal alloys and heavily doped semiconductors is presented. The performance of each material is evaluated based on quality factors defined for each class of plasmonic devices. Most importantly, this paper outlines an approach for realizing optimal plasmonic material properties for specific frequencies and applications, thereby providing a reference for those searching for better plasmonic materials.

1.1 Introduction

The speed of information processing has seen rapid growth in the past few decades from the progress in scaling down the sizes of devices in micro- and nanoelectronics. However, researchers are experiencing major difficulties in reaching speeds over a few tens of GHz using this scaling approach due to fundamental limitations from RC-delays and power dissipation in the devices. In contrast, photonics offers bandwidth in the THz range [1]. However, conventional photonic elements, such as optical fibers, require physical dimensions on the order of the wavelength of light (about a micron) due to diffraction limitations. The difference in physical size between nanometer-scale electronics and micrometer-scale photonic elements yields an incompatibility between the two types of devices. Plasmonics merges the high bandwidth offered by photonics and the nano-scale integration offered by nanoelectronics by coupling a photons energy with a free-electron gas, creating a subwavelength, oscillating mode known as a plasmon [2–5]. Because plasmonic devices are capable of subwavelength confinement, plasmonics forms the basis of the research area of nanophotonics. Plasmonics and the recent birth of metamaterials [6–8] (for recent review on optical metamaterials see [9]) and Transformation Optics (TO) [10–12] are currently driving the development of a family of novel devices with unprecedented functionalities such as subwavelength waveguides [4, 13, 14], optical nanoantennas [15–24], superlenses [7, 25–28], optical invisibility cloaks [11, 29–32], hyperlenses [33–36], planar magnifying hyperlens and light concentrators [8, 37, 38].

Because the plasmon phenomenon in optical and telecommunication frequencies typically originates from the collective oscillations of free charges in a material due to an applied electromagnetic field, plasmonic devices generally require metallic components, which have an abundance of free electrons. These free electrons provide the negative real permittivity that is an essential property of any plasmonic material. However, metals are plagued by large losses, especially in the visible and ultra-violet (UV) spectral ranges, arising in part from interband electronic transitions. Even the metals with the highest conductivities suffer from large losses at optical frequencies [39, 40]. These losses are detrimental to the performance of plasmonic devices, seriously limiting the feasibility of many plasmonic applications. In an attempt to mitigate material losses, optical gain materials can be combined with metallic structures [41–55]. However, even the best gain materials available are barely enough to compensate the losses in the metal. Because these losses are inherent to the constituent materials, alternative plasmonic materials with lower losses are required to develop robust plasmonic devices. Lower losses in such improved plasmonic components can be readily compensated with existing gain materials.

Plasmonics could have a large impact on applications at telecommunication and optical frequencies, and hence we begin this review with a survey of several potential plasmonic materials (also see [56]). We compare the relative merits of these potential materials within the context of novel plasmonic devices to gain insight into the suitability of each material in particular applications. In Sect. 1.2, we provide a brief background on the various electromagnetic losses associated with solids at frequencies in and near the visible range. In Sect. 1.3, we review the optical properties of various plasmonic materials and also discuss the methodologies adopted in choosing potential low-loss materials for plasmonics. Specifically, Sects. 1.3.1, 1.3.2, and 1.3.3 review metals, metal-alloys, heavily doped wide-band semiconductors, and graphene respectively. We formulate the figures-of- merit (or quality factors) for various classes of plasmonic devices to effectively compare the performances of plasmonic materials in Sect. 1.4. Finally, in Sect. 1.5, we present a comparative study of the performance of the various potential materials based on figures-of-merit and other practical criteria. We conclude the paper with a discussion that quantitatively identifies the best of the reviewed material choices for each class of devices for various regions of the visible and near-infrared (NIR) ranges.

1.2 Background

Polarization describes a materials interaction with electromagnetic waves. While polarization can be electrical and/or magnetic in nature, the magnetic polarization of naturally occurring materials is negligible for frequencies higher than several hundred THz. The electrical polarization can be described by the materials complex electrical permittivity or dielectric function, denoted by $\epsilon(\omega)$. While the real part of the dielectric function (denoted by ϵ_1 or ϵ') describes the strength of the polarization induced by an external electric field, the imaginary part (denoted by ϵ_2 or ϵ'') describes the losses encountered in polarizing the material. Thus, a low loss material is associated with small values of ϵ''.

Primary loss mechanisms in the NIR, visible, and soft UV frequencies may be broadly classified as arising from phenomena related to conduction electrons and bound electrons (interband effects) [57]. Losses for conduction electrons arise from electron-electron and electron-phonon interactions, and from scattering due to lattice defects or grain boundaries. Because the conduction electrons have a nearly continuum of available states, their interaction with an electromagnetic field is well approximated by classical theory. The Drude theory [58] describes this phenomenon by treating conduction electrons as a three-dimensional free-electron gas. According to the generalized Drude theory, the permittivity of a material can be written as follows:

$$\epsilon(\omega)' + i\epsilon(\omega)'' = \epsilon(\omega) = \epsilon_{int} - \frac{\omega_p^2}{\omega(\omega + i\Gamma)}, \tag{1.1}$$

$$\omega_p^2 = \frac{ne^2}{\epsilon_0 m^*}. \tag{1.2}$$

In Eq. (1.1), $\gamma = 1/\tau$ where τ is the mean relaxation time of conduction electrons, and ϵ_{int} is a contribution due to interband transitions; it is unity for the case of a perfectly free-electron-gas. The plasma frequency (ω_p) is given by Eq. (1.2), where n is the conduction electron density, and the effective optical mass of conduction

Table 1.1
Drude model parameters for metals. ω_{int} is the frequency of onset for interband transitions. Drude parameters tabulated are not valid beyond this frequency.

Material	ϵ_{int}	$\omega_p(eV)$	Γ (eV)	ω_{int} (eV)
Silver [39,59,60]	3.7	9.2	0.02	3.9
Gold [39,60]	6.9	8.9	0.07	2.3
Copper [39,59,60]	6.7	8.7	0.07	2.1
Aluminum [61,62]	0.7	12.7	0.13	1.41

electrons is m^*. In general, ϵ_{int} depends on wavelength (which is typically accounted by including the Lorentz oscillators terms [57]), but for some spectral ranges it can be roughly approximated as constant (see Table 1.1). Also, Γ can depend on the size of the plasmonic particle. According to the classical theory, the total damping rate, Γ, is the sum of damping rates due to electron-electron scattering, electron-phonon scattering and lattice defects or grain-boundary scattering. The boundary scattering rate depends on the size of the plasmonic particle, so that the relaxation rate for a spherical particle of size R can be approximated as:

$$\Gamma = \Gamma_\infty + A\frac{v_F}{R}, \tag{1.3}$$

where Γ_∞ is the relaxation constant of the bulk material, v_F is the Fermi velocity; A depends on details of the scattering process, and is typically on the order of unity [57,63,64]. For simplicity, below we assume that $\Gamma = \Gamma_\infty$.

Because plasmonic applications require materials with negative ϵ_0, Eq.(1.1) clearly indicates that this requirement is satisfied for materials with a plasma frequency higher than the desired frequency of application. Because metals tend to have large plasma frequencies and high electrical conductivity, they have traditionally been the materials of choice for plasmonics. In Table 1, we summarize the material parameters for high-conductivity metals as reported in the literature. Among the metallic elements, silver has the smallest Γ and is the best-performing choice at optical frequencies. Gold, which has a larger Γ than silver, is often the metal of choice at lower NIR frequencies, having the advantage of being chemically stable in many environments. However, gold has high interband losses in the visible spectrum for wavelengths below or about 500nm. Similarly, copper is plagued by large interband losses over most of the visible spectrum. Thus, silver and gold have predominately been the materials of choice for plasmonic applications around the optical frequencies. However, future plasmonic applications demand even lower losses to fully exploit their potential.

Interband transitions, which form a significant loss mechanism in materials at optical frequencies, occur when electrons jump to higher, empty energy levels caused by absorption of incident photons. In metals, when a bound electron absorbs an incident photon, the electron can shift from a lower energy level to the Fermi surface or from near the Fermi surface to the next higher empty energy level. Both of these processes result in high loss at optical frequencies.

In semiconductors and insulators, valence electrons absorbing the energy from a photon shift into the conduction band, resulting in loss. This loss manifests as an increase in ϵ'', and can be treated using the formalism of the Lorentz oscillator model. The two-level description of the absorption process results in a simple Lorentz model given by Eq. (1.4) [65]:

$$\epsilon_{lk}(\omega) = \frac{f_{lk}\omega_p^2,_{lk}}{\omega_{lk}^2 - \omega^2 - i\omega\Gamma_{lk}}. \tag{1.4}$$

Here, f_{lk} corresponds to the strength of the oscillator at energy levels l and k, ω_{lk} is the resonant frequency corresponding to the difference between the energies of levels l and k, Γ_{lk} is the damping in the oscillator accounting for non-zero line-width of the peak, and $\omega_{p,lk}$ is similar to the plasma frequency given by Eq. (1.2) with the difference that n here refers to the concentration of electrons in the lower occupied state. When there are many of such interacting energy levels, the effective permittivity can be expressed as a summation over all allowed Lorentzian terms. This is a popular approach utilized in the Drude-Lorentz model to reasonably approximate the dielectric function of metals [66]. In general, solids with a periodic lattice have electronic energy levels which exist as bands instead of discrete levels, requiring a Joint-Density-of-States description and integration over all the allowed transitions at any given photon energy (a more detailed discussion of this formulation is found in [65]).

To illustrate the impact of interband transitions on losses in a material, Fig. 1.1 shows the imaginary part of permittivity for copper. The free-electron and interband transition contributions to loss are shown along with the values extracted from experimental results [39]. The peak in the experimental ϵ'' curve at 2.1 eV clearly corresponds to interband transitions; this peak is the result of electronic transitions from the filled L3 band to the Fermi surface [59]. Similarly, the peak at 5.2 eV is due to $X_5 \rightarrow X_{40}$ transitions and $L2 \rightarrow L1$ transitions [59]. Table 1 shows the frequency ω_{int} that marks the onset of significant loss due to interband transitions in several selected metals.

The direct transitions discussed above form an important loss mechanism in both semiconductors and insulators. In direct bandgap semiconductors, the bandgap corresponds to the onset of interband transitions. In indirect bandgap semiconductors, indirect transitions contribute to loss for photon energies exceeding the bandgap before the direct transitions set in. For photon energies below the bandgap, there can be appreciable losses due to various mechanisms such as trap-assisted transitions (*e.g.* nitrogen levels in GaP:N [67]), generation of excitons (especially for wide bandgap semiconductors and insulators [68–70]) and transitions between impurity levels [71].

1.3 Survey of Alternative Plasmonic Materials

This section focuses on potential candidates for low-loss plasmonic materials in the NIR, visible, and near-UV spectral ranges. Various metals, metal-alloys, metallic com- pounds and semiconductors that can offer advantages as plasmonic materials are

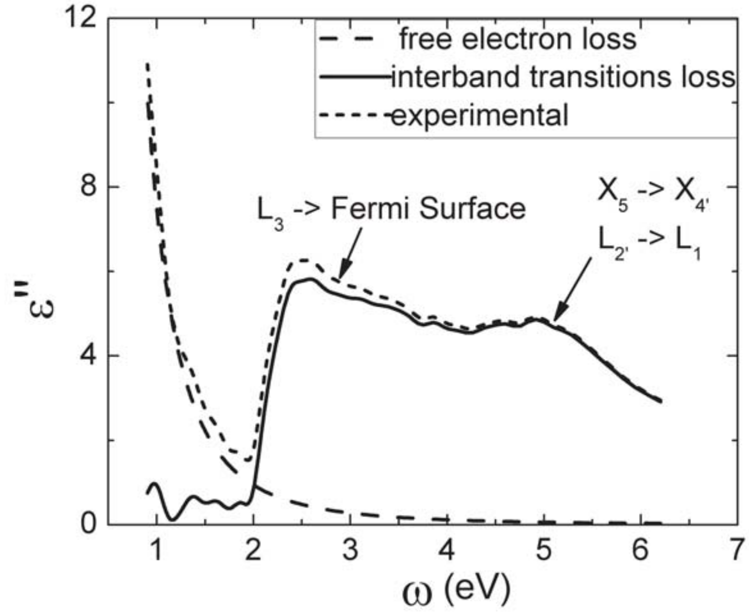

Fig. 1.1. The losses in Cu shown as the sum of interband losses and free electron losses [39, 59]. Annotations identify the interband transitions responsible for peaks in ϵ''

identified and discussed in terms of their relevant properties. Discussion is categorized into subsections based on the class or type of material reviewed. Metals are considered first, followed by metal-alloys in the second subsection. The third subsection focuses on doped semiconductors, while the last discusses graphene.

1.3.1 Metals as Candidates for Plasmonics

As discussed in Sect. 1.2, metals are candidates for plasmonic applications because of their high conductivity. Among metals, silver and gold are the two most often used for plasmonic applications due to their relatively low loss in the visible and NIR ranges. In fact, almost all of the significant experimental work on plasmonics has used either silver or gold as the plasmonic material. Silver has been used for the demonstration of a superlens [26, 27], a hyperlens [35], a negative-refractive-index material in the visible range [72], and extraordinary optical transmission [73]. Gold was used for the first demonstration of a negative-refractive-index material in the NIR [74], many studies on Surface-Enhanced Raman Scattering (SERS), the fabrication of plasmon waveguides, and numerous Localized Surface Plasmon Resonance (LSPR) sensors (see for instance, [75]). While metals other than silver and gold have been used in plasmonics, their use is quite limited, as their losses are higher than those of silver and gold. For instance, platinum and palladium have been used as plasmonic materials in systems where the catalytic activity of the plasmonic material is important to the overall device functionality [76, 77]. In addition, nickel films have been reported to have surface plasmon-coupled chemiluminescence, which may merit the use of nickel in particular plasmonic applications.

Among the alkali metals, sodium and potassium have the lowest losses [78, 79]. In fact, these losses are comparable or even better than that of silver. Although there have been several theoretical studies on alkali metals [79], they will not be discussed in this section, as their potential has not been experimentally verified to our knowledge. In pure elemental form, these alkali metals are very reactive to air and water, and therefore they must be stored in mineral oil or Ultra High Vacuum (UHV) environments to avoid highly energetic and dangerous reactions. Such extreme restrictions have made fabrication with alkali metals prohibitive. While depositing alkali metals can be a straightforward process, accomplished with an alkali metal dispenser, other fabrication and characterization obstacles must be overcome before alkali metals find use in plasmonics. In the following section, we will discuss low-loss noble metals (silver, gold and copper) and aluminum. The plots of ϵ' and ϵ'' of these four metals along with potassium and sodium are shown in Fig. 1.2

As previously mentioned, silver has the lowest loss in the visible and NIR ranges. However, in terms of fabrication, silver degrades relatively quickly and the thickness threshold for uniform continuous films is around 1223nm [80–82], making silver less suitable for TO devices (discussed in Sect. 5). Additionally, silver losses are strongly dependent on the surface roughness [57]. Gold is the next-best material in terms of

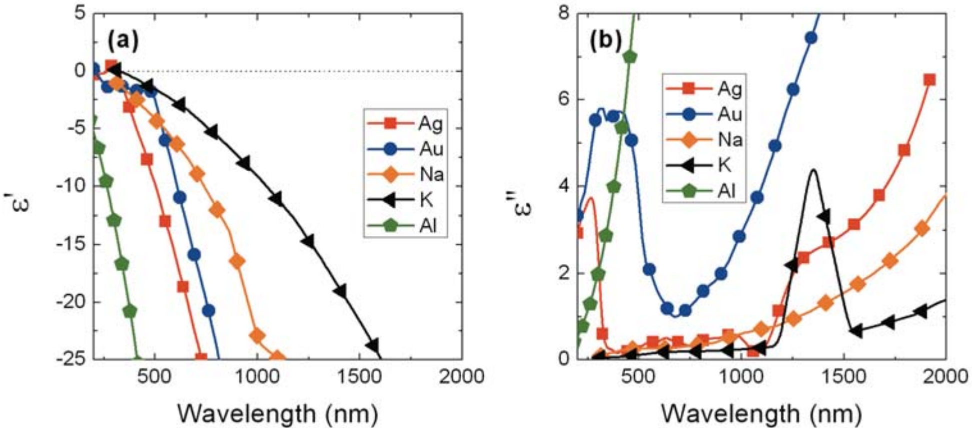

Fig. 1.2. Real (a) and imaginary (b) parts of the permittivities of Ag, Au, Na, K, and Al. The data for Ag, and Au are taken from [39], and those of Al, Na, and K are from [78]

loss in the visible and NIR ranges. Compared with silver, gold is chemically stable and can form a continuous film even at thicknesses around 1.57nm [83, 84]. It is very important to note that films deposited with thicknesses below the percolation threshold are semi/discontinuous with drastically different optical properties compared to uniform films [85, 86]. These fabrication complications make these materials undesirable at thicknesses below the percolation threshold when continuous films are needed. Silver and gold films can be fabricated by various physical vapor deposition (PVD) techniques and nanoparticles and metal-coated nanoparticles can be synthesized by liquid chemical methods. Typical PVD methods include electron-beam/thermal evaporation and sputtering. In liquid chemical methods, chloroauric acid ($H[AuCl_4]$) and silver oxide (Ag_2O)/silver nitrite ($AgNO_4$) are commonly used for gold and silver, respectively.

Because copper has the second-best conductivity among metals (next to silver), it is expected to exhibit promising plasmonic properties. Indeed, ϵ'' of copper is comparable to that of gold from 600-750nm. Considering the cost of silver and gold, copper would be a good candidate to replace silver and gold as a plasmonic material if the performance of copper were tolerable. Unfortunately, fabricating devices with copper is challenging, as it easily oxidizes and forms Cu_2O and CuO. A systematic study of the oxidation effects on copper for LSPR modes is found in [87]. In their results, Chan et al. have demonstrated that oxide-free nanospheres exhibit a sharp and narrow LSPR peak comparable to that of silver and gold.

Aluminum has not been an attractive plasmonic material due to the existence of an interband transition around 800nm (1.5 eV), resulting in large ϵ'' values in the visible wavelength range (see Fig. 1.2). However, in the UV range, ϵ' is negative even at wavelengths smaller than 200nm where ϵ'' is still relatively low. Thus aluminum is a better plasmonic material than either gold or silver in the blue and UV range. It is important to note that the ϵ' values of silver and gold do not become positive until wavelengths greater than 326nm and 207nm, respectively. Aluminum is easily oxidized and very rapidly forms an aluminum oxide (Al_2O3) layer under atmospheric conditions, making device fabrication with aluminum challenging. The thickness of this Al_2O3 layer is typically 2.5-3nm [88], and the presence of this oxide layer results in a red shift in LSPR peak position [89]. Despite these challenges, aluminum has been used in plasmonic systems in the UV-blue spectral region such as to study LSPR [88, 89], surface plasmon polariton (SPP) propagation [90], surface-enhanced fluorescence [91, 92], and Raman spectroscopy [93, 94].

1.3.2 Metallic Alloys

Metallic alloys, intermetallics and metallic compounds are potential candidates for alternative plasmonic materials owing to their large free electron densities. This section primarily discusses the various techniques employed to tune the optical characteristics of metals by making alloys. Metallic compounds such as magnesium diboride (MgB_2) are not discussed here due to their poor performance as plasmonic materials around optical frequencies [95–99]. Similarly, intermetallics such as silicides, which are reported to be plasmonic materials, will not be discussed owing to their large losses in the NIR and visible spectrum [100–105].

Noble-Transition Alloys

Because of the strong plasmonic performance of noble metals, one approach to improve these materials is by shifting their interband transitions to another (unimportant) part of the spectrum. This can be achieved by alloying two or more elements to create unique band structures that can be fine- tuned by adjusting the proportion of each alloyed material.

Noble-transition metal alloys are one interesting set of potential alternative plasmonic candidates. Bivalent transition metals, such as Cadmium and Zinc, when doped into monovalent noble metals contribute one extra electron to the free-electron plasma [106]. This results in n-type doping of noble metals, which raises the Fermi level, increases ω_p, and shift the threshold for interband transitions, thereby modifying the optical spectra of the alloy. By changing the Fermi level of a metallic layer, one can, in principle, reduce the absorption at a specific wavelength. This could be accomplished, for example, by shifting the Lorentzian peak to some other wavelength that is unimportant for a particular application. This process of manipulating and fine-tuning a materials electronic band structure to achieve desirable electronic properties is referred to as band engineering.

The particular experiment detailed in [106] involved n-doping gold with cadmium and employed samples with pre-determined stoichiometries that were purchased from commercial vendors. Alloying gold and cadmium creates a unique band structure, shifting the peak losses to new frequencies and resulting in higher losses in one frequency range, with simultaneously lower losses in another range. To illustrate this point, Fig. 1.3 shows a simulation demonstrating how doping gold with cadmium shifts the interband transition peaks, confining high losses to one region while lowering losses almost everywhere else in the spectrum. This method of raising the Fermi level by small amounts can continue for low doping levels (<10% volume), but the technique will break down as the doping levels become high enough to significantly modify the materials band structure. This technique may be extended to different material combinations, creating unique band structures optimized for specific frequencies and applications.

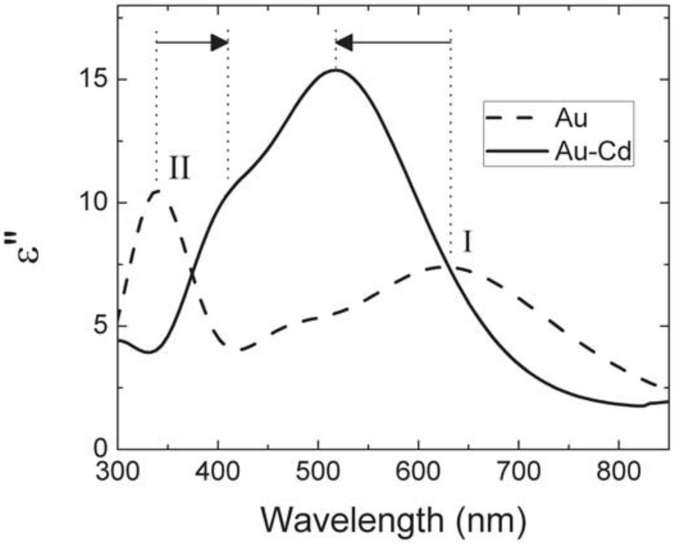

Fig. 1.3. By courtesy of Dr. M. Noginov and Dr. V. Gavrilenko, Norfolk University [106]) Numerical simulation detailing the shift in interband transition peak and modified band structure when Au [39] is doped with 3.3 at.% Cd. The dashed curve shows the imaginary permittivity for the undoped gold, while the solid curve is the result for the doped alloy. The doping process combines the losses from peaks I & II into a single, confined high-loss region, while leaving lower losses elsewhere.

Alkali-Noble Inter-Metallic Compounds

Alkali-noble metal inter-metallic compounds are another group of candidates for low-loss metals because the Group I alkali metals exhibit the strongest free-electron-like behavior [107]. As far back as 1978 [108], the permittivity of Li_2AgIn was experimentally measured, exhibiting zero-loss permittivity values at 2 eV without mention of the implication of this result for plasmonic devices. Note that this paper presents data showing negative losses, which raises some doubts about the accuracy of measurements or parameter extraction. While many alkali-noble metal binary compounds have been presented as alternative plasmonic materials [107], the compound predicted to show the most promise is potassium gold (KAu), which has been calculated to have zero interband losses below its unscreened plasma frequency at 1.54 eV. However, because of Drude losses, the crossover point is 0.5 eV. Because KAu does not have negative ϵ values in the telecommunication and visible frequency ranges, it cannot be considered a plasmonic candidate for applications in these spectral ranges.

Fabrication of alkali-noble compounds can be challenging. Just bringing two metals of significantly different properties together to form an alloy can be a non-trivial task. The vapor pressures of potassium and gold differ by 10 orders of magnitude and their surface energies differ by an order of magnitude, making the alloying process difficult. Assuming these compounds behave similarly to pure alkali metals, these highly reactive alloys must either be characterized in-situ or be passivated prior to removing them from the fabrication chamber in order to prevent rapid oxidation. Passivation would allow for further optical characterization of the fabricated sample using ellipsometry, prism coupling, SPP propagation, and other techniques, but the passivation itself may alter the surface properties of the sample as well as limit applicability of such films for real device fabrication. Because such compounds have not been extensively studied in the past, the phase, stoichiometry and growth kinetics of these alloy systems are not well understood.

1.3.3 Semiconductors

Semiconductors are conventionally regarded as dielectric materials for frequencies above several hundred THz. However, semiconductors can actually exhibit a negative real permittivity in this spectral region under certain circumstances [109–112]. Due to the ease of fabrication and flexibility in tuning their properties such as carrier concentration, semiconductors are also potential materials for plasmonics. In order to qualify as a low-loss plasmonic material, the bandgap and plasma frequency of the semiconductor both must be larger than the frequency range of interest. While a large plasma frequency ensures a negative real permittivity, a large bandgap ensures almost no interband transition losses. Semiconductors can exhibit negative ϵ' in IR frequencies when heavily doped [109–111] or in resonance (*e.g.* phonon resonance in silicon carbide [78, 112, 113]). Because resonance is a narrow-band phenomenon and phonon resonance occurs at low frequencies, here we con- sider only heavily doped semiconductors as possible low- loss plasmonic materials. Thus, a wide bandgap, heavily doped semiconductor with high carrier mobility can qualify as a low loss plasmonic material around the optical frequencies.

Despite the abundance of semiconductors with large bandgap values ($>$ 1.5 eV) and high carrier mobilities, very high doping levels are necessary to bring the crossover frequency of semiconductors into the optical range, and achieving these doping levels is challenging. Hoffman et al. [111] reported that doping gallium arsenide to 7×10^{18} cm^{-3} can raise the crossover frequency (where ϵ' changes from negative to positive) to about 9μm. However, to bring the crossover frequency near the optical range, a doping level of at least 3×10^{20}cm^{-3} is required. The necessity of doping semiconductors so heavily raises concerns about the solid solubility limit, the fraction of dopants that would be active, and doping compensation effects [114, 115]. Another major concern at such high doping levels is retaining the high carrier mobility that is essential for low losses. Due to these issues, plasmonics in the optical spectrum has remained mostly out-of-reach for semiconductor materials.

However, indium-tin-oxide (ITO) has been shown to be a potential plasmonic material in the NIR region [116–120]. ITO is a transparent, conducting oxide typically consisting of 90% wt indium oxide (In_2O3) and 10%wt tin oxide (SnO_2). ITO has been widely studied in the field of optoelectronics. Because ITO is non-stoichiometric, predictions show its plasma frequency can be engineered between 0.44 eV and 6.99 eV by varying the tin (Sn) doping level in In_2O_3 up to 45%wt. Experimentally, the plasma frequency has been measured between 0.78 and 2.13 eV [110,121,122]. Robusto et al have demonstrated SPPs in ITO between 1.8μm and 1.9μm [116], which was followed by many other groups [117–120] reporting SPPs in the NIR region. Therefore, ITO appears to be an appealing plasmonic material in the NIR and optical frequency ranges.

Because ITO is a non-stoichiometric compound, its optical properties largely depend on the growth/deposition processes and annealing conditions, including the temperature and ambient gasses [110]. Sputtering and laser ablation techniques have reliably produced quality films of ITO [123]. Post-deposition annealing in nitrogen has been shown to produce more conductive and less transparent films due to increased oxygen vacancy (V_O) defects [124]. On the other hand, less conductive and more transparent films are produced by annealing ITO in an oxygen ambient [124]. In our own experiments, we have observed significant changes in the dielectric function of e-beam evaporated ITO films annealed in different ambient environments, as shown in Fig. 1.4. While ITO films annealed in oxygen do not show negative ϵ' in the spectrum of interest, the films annealed in nitrogen ambient do show negative real permittivity. Fig. 1.4 also shows that ITOs properties depend on the annealing temperature. A higher annealing temperature increases the conductivity of the ITO film and reduces the loss within the wavelength range of interest. It is important to note that the loss in ITO films is comparable to that of silver in the NIR range but is significantly lower than the losses in silver at longer wavelengths.

Other than ITO, high performance conductive zinc oxides such as Aluminum Zinc Oxide (AZO) and Gallium Zinc Oxide (GZO) can be promising low-loss alternatives in NIR. These conductive zinc oxides are widely studied for applications in transparent electronics. Based on the optical characteristics of these films reported in literature, we have found that AZO and GZO can have significantly lower loss than silver at telecommunication wavelengths which are of particular importance for photonics and nanophotonics applications (see Fig. 1.5) [125–127]. While AZO can exhibit losses

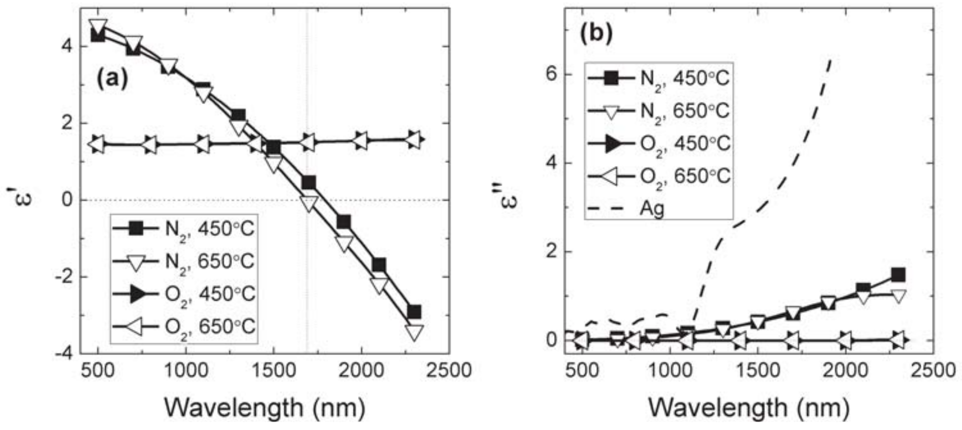

Fig. 1.4. Real (a) and imaginary (b) parts of permittivity of ITO annealed at various conditions (N_2, 450°C; N2, 650°C; O_2, 450°C; O_2, 650°C).

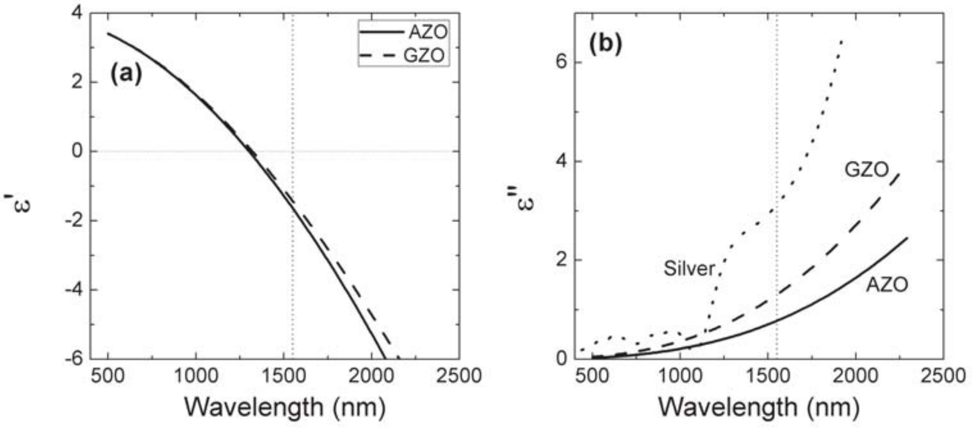

Fig. 1.5. Real (a) and imaginary (b) parts of permittivity of AZO and GZO obtained from parameters reported in reference [125]. The losses in AZO and GZO are much smaller than that of silver [39] at the telecommunication wavelength.

more than three times lower than that of silver at the wavelength of 1.5μm, GZO being only slightly inferior to AZO, can exhibit lower losses too.

Similar to other conductive oxides, AZO and GZO are non-stoichiometric, and deposition conditions play a crucial role in achieving the desired properties. High quality thin films of AZO and GZO may be produced by sputtering or laser ablation. Deposition temperature, oxygen partial pressure during deposition and dopant concentration must be optimized in order to achieve low loss as well as negative real permittivity [109, 125–129]. For example, M. H. Yoon et al. report that large doping of zinc oxide does not necessarily increase the carrier concentration [130]. In AZO, a large doping level results in the formation of $ZnAl_2O_4$, which does not increase carrier concentration, but adversely affects the carrier mobility through increased scattering. This causes the zero-cross-over of real permittivity to shift towards longer wavelengths. We observe this happening in Pulsed Laser Deposited (PLD) AZO films with 2%wt Al_2O_3. Evidently, lower Al_2O_3 concentration of about 0.8 %wt produces AZO films with ϵ' -cross-over at a wavelength smaller than 1.5μm [125]. With losses being much smaller than in silver at this wavelength, AZO is a promising low-loss alternative material for plasmonics in NIR.

Aside from oxide semiconductors, III-V semiconductors (*e.g.* GaAs, GaN, GaP) and SiC are potential candidates for plasmonics in the NIR and optical spectral ranges. However, heavy doping could again be a problem that must be addressed when considering these materials as options for alternative plasmonic materials.

1.3.4 Graphene

Graphene is another material that has generated excitement in the research community due to its unique band structure and high carrier mobility [131–134]. Graphene is a two-dimensional system - enabling excitation of surface plasmons (SP) similar to the surface plasmons on metal/dielectric interfaces. However, these two-dimensional plasmons in graphene exhibit a dispersion relation different compared to plasmons in three dimensions [135–137]. Some schemes for plasmon based THz oscillators in graphene have already been proposed in literature [138–140]. These plasmon modes can possibly exist up to near-IR frequencies. However, in order to evaluate the potential of graphene as an alternative low loss plasmonic material, the losses in the plasmon modes must be evaluated [141].

It can be expected that interband transitions contribute significantly to losses because of the zero band-gap in graphene. These interband transitions occur above a threshold determined by Fermi energy and plasmon wavevector [136]. However, this threshold can be shifted to frequencies beyond the region of interest by larger doping, which increases the Fermi energy. It has already been experimentally demonstrated that the interband threshold can be tuned by varying electrical doping [142]. Below the interband threshold, the losses are primarily due to impurity scattering and excitation of optical phonons together with electron-hole pairs. Jablan et al. have analyzed the electron relaxation times due to different loss mechanisms in graphene, and demonstrate that graphene may inherently contain lower losses relative to conventional metal/dielectric interfaces up to frequencies corresponding to 0.2 eV [141]. Initial theoretical estimates indicate that graphene is a good plasmonic material for THz applications. However, at NIR frequencies, losses in graphene may still be comparable to noble metals. This makes graphene less attractive as an alternative plasmonic material at the telecommunications and visible wavelengths.

1.4 Quality Factors

Quality factors, or figures-of-merit, form a common platform to compare the performances of various materials used in different applications over a wide frequency band. Although the loss in a material characterized by ϵ'' is a necessary indicator of performance, the real part of permittivity ϵ' is also important in quantifying the overall material quality in many devices. Because the field distribution in a material depends on ϵ' and the loss depends on ϵ'', performance metrics or quality factors for a plasmonic material are generally a function of both ϵ' and ϵ''. Considering that different applications can have different definitions for the quality factors [143–146], our discussion is focused on four major classes of plasmonic devices: LSPR based devices, SPP waveguides, TO devices and superlens. It is important to note that the following discussions are valid only in the range of frequencies for which ϵ' is negative. For metals and metal-like materials such as heavily doped semiconductors, this translates to frequencies below the crossover frequency. It should also be noted that in the following discussion, the term metal is used for both metals and metal-like materials for brevity.

In the first part of this section, the quality factors of LSPR and SPP systems are considered and are denoted as QLSPR and QSPP, respectively. LSPR and SPR systems produce local field enhancement at the surface of metallic components. Hence their quality factors can be defined as follows:

$$Q_f = \frac{(Enhanced\, local\, field)}{(Incident\, field)} \tag{1.5}$$

Quality factor for LSPR depends significantly on the shape of the metal nanoparticles. For a sphere, Q_{LSPR} is given by Eq. (1.6):

$$Q_{LSPR}(\omega) = \frac{-\epsilon'(\omega)}{\epsilon''(\omega)}. \tag{1.6}$$

For a cigar-shaped spheroid, Eq. (1.6) becomes Eq. (1.7):

$$Q'_{LSPR}(\omega) = \frac{\epsilon'(\omega)^2}{\epsilon''(\omega)}. \tag{1.7}$$

For SPR, the quality factor Q_{SPR} assumes the same form as Eq. (1.6). Q_{SPP} can be defined as the ratio of the real part of the propagation wavevector (k'_x) to the imaginary part (k''_x) [147]:

$$Q'_{SPP}(\omega) = \frac{k'_x(\omega)}{k''_x(\omega)} = \frac{\epsilon'_m(\omega) + \epsilon_d(\omega)}{\epsilon'_m(\omega)\epsilon_d(\omega)} \frac{\epsilon'_m(\omega)^2}{\epsilon''_m(\omega)}, \tag{1.8}$$

where ϵ_m is the permittivity of the metal, and ϵ_d is the permittivity of the surrounding dielectric material. If $|\epsilon'_m| \gg \epsilon_d$, Eq. (1.8) can be simplified as follows:

$$Q'_{SPP}(\omega) = \frac{\epsilon'(\omega)^2}{\epsilon''(\omega)}. \tag{1.9}$$

It may be noted that Q_{SPP} has the same form as Q'_{LSPR} defined for spheroid nanoparticles. The quality factors for LSPR and SPP are shown in Fig. 1.6. This figure does not include semiconductors and alloys, as their quality factors are much lower than the rest. Eqs. (1.6) & (1.9) explain how Q_{LSPR} and Q_{SPP} become large when a material has a large, negative ϵ' and a small ϵ''. These equations clearly convey why conventional plasmonic materials such as silver and gold, which have a large, negative ϵ' and a low ϵ'', have been the plasmonic materials of choice for most applications.

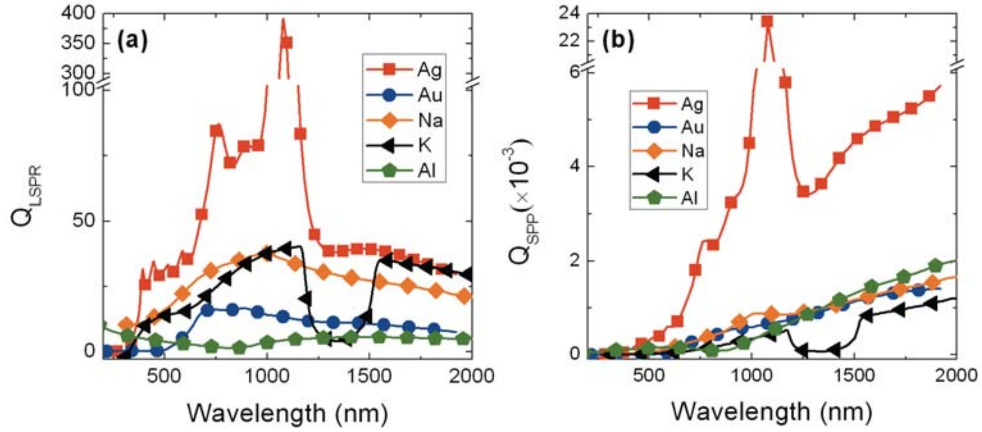

Fig. 1.6. Quality factors for localized surface plasmon resonances (Q_{LSPR}) is shown in panel (a), and surface plasmon polaritons quality factor (Q_{SPP}) is shown in panel (b). The permittivity values used to calculate the presented quality factors are the same as those shown in Fig. 1.2

Transformation optics (TO) devices, however, require a different figure of merit due to the nature of TO devices. These devices typically need materials with a real part of *effective* permittivity close to zero at the operating frequency [12]. Thus, TO devices require the response of metallic components to be nearly balanced by that of dielectric components (which typically have $\epsilon_d \sim 1$). Hence, for practical values of metal filling factors, the magnitude of ϵ'_m of metal must be comparable in magnitude (and opposite in sign) to that of the dielectric component. Thus, plasmonic components of TO devices operate near their crossover frequency where ϵ' is negative and small in magnitude. Thus, in this case, only the losses (ϵ'') are relevant in defining the quality factor:

$$Q_{TO} = \frac{1}{\epsilon''_m} \text{ (where } -\epsilon'_m \sim \epsilon_d \sim 1) \tag{1.10}$$

We now turn our attention to the superlens and its resolution limits. The resolution limit of superlens can be defined through Eq. (1.11):

$$\frac{\Delta}{d} = \frac{-2\pi}{\ln\left(\frac{-\epsilon''}{2\epsilon'}\right)} \tag{1.11}$$

where Δ is the minimum resolvable feature size and d is the thickness of the superlens [148]. The value Δ/d can be considered as the normalized resolution of the superlens. For the purpose of comparative studies using quality factors, we define the inverse of Δ/d as the superlens quality factor Q_S. For the sake of comparison, the host material is assumed to be air, hence ϵ' of the superlens is set to -1 for the following discussion. Therefore, Q_S can be expressed as:

$$Q_S = \frac{d}{\Delta} = \frac{-\ln\frac{\epsilon''}{2}}{2\pi} \text{ (where } \epsilon' = 1). \tag{1.12}$$

Quality factors give a quantitative assessment of the performance of plasmonic materials in their respective categories. However, practical considerations arising from fabrication and integration issues must be considered before choosing the best material.

1.5 Comparative Studies

A summary of the figures-of-merit for various materials discussed in the previous sections is provided in Table 1.2. While quality factors describe how well a material will perform for various applications, there are limiting issues in terms of processing and fabrication. For example, alkali metals are difficult to work with because they are extremely reactive in air ambient environments. Thus, alkali metals have not been used in plasmonic applications regardless of their high quality factors. In addition, silver and aluminum are not ideal materials for the fabrication of plasmonic devices because these materials easily oxidize when exposed to air, which can significantly alter their plasmonic properties. Other fabrication issues can arise in particular designs, such as the formation of extremely thin metallic films and the controlled synthesis of metallic nanoparticles.

Table 1.2
Table comparing various plasmonic metals researched in this study

	LSPR & SPR		SPP		TO Devices	Superlens	Comments
Material	Maximum Q_{LSPR} (λ)	Q_{LSPR} (1.5μm)	Maximum Q_{SPP} (λ)	Q_{SPP} (1.5μm)	Q_{TO} (λ)	Q_S (λ)	
Ag*	392 (1.08μm)	39.3	23413 (1.08μm)	4530	1.82 (326nm)	0.3 (339nm)	Good for LSPR & SPP
Au*	16.66 (0.89μm)	10.63	1410 (1.94μm)	1140	0.29 (207nm)	-0.13 (252nm)	Good for LSPR
Al	13.56 (0.113μm)	5.55	2677 (2.5μm)	1315	26.32 (82nm)	0.52 (114nm)	Good for LSPR in UV
Na*	37.8 (1.00μm)	27.3	1889 (2.25μm)	1179	NA***	0.48 (312nm)	Difficult to process
ITO*	2.72 (2.3μm)	NA**	16 (2.3μm)	NA**	1.54 (1.69μm)	0.13 (1.88μm)	Good for TO in NIR
AZO	3.28 (2.26μm)	1.46	33.1 (2.5μm)	2.33	2.16 (1.3μm)	0.179 (1.46μm)	Good for TO in NIR
GZO	1.8 (2.3μm)	0.923	15.96 (2.5μm)	1.01	1.22 (1.32μm)	0.087 (1.48μm)	Good for TO in NIR
*	Ag and Au data ends at 2μm, Na, K data ends at 2.25μm, and ITO data ends at 2.3μm.						
**	Crossover frequency for these materials occurs at a wavelength above 1.55μm. Thus, quality factors are not applicable at the telecommunication wavelength.						
***	Crossover frequency data is not available.						

Therefore, despite the fact that sodium and potassium have the highest Q_{LSPR} and Q_{SPP} values next to silver, they are extremely difficult to work with, and are therefore probably not practical from a fabrication standpoint. In most cases, silver is by far the best material in terms of quality factor, but it is associated with problems such as oxidation and cost. Aluminum has the advantage of having an extremely high plasma frequency, and it is the only reviewed material that acts as a metal in the UV part of the spectrum. However, aluminum also oxidizes quite easily, which can cause issues in terms of fabrication.

Quality factors for TO devices and superlens indicate that alkali metals can be a good choice. However, they have problems with processing and hence are not the material of choice. Aluminum has a high Q_{TO} value, but is probably not particularly good for TO applications. This is due to the fact that at the Al crossover wavelength of 81nm, the thickness of the aluminum layer can be at most 8nm for effective medium theory to hold. In this range, film roughness, as well as the formation of oxidation layers, could be detrimental to the plasmonic properties of the aluminum structure. However, Aluminum will perform well as a superlens, if these issues can be resolved. Silver also suffers from similar fabrication problems. From the alkali-noble metal alloys, KAu is a possible candidate for TO or superlens applications in terms of the materials quality factor, but there are serious challenges with the synthesis and chemical stability of KAu. In contrast, doped zinc oxide and indium-tin-oxide are realistic choices for TO devices in the NIR range including the telecommunication wavelength, which is particularly important for nanophotonics circuitry. With the optimization of processing conditions, these materials can outperform silver for TO applications, potentially enabling unsurpassed control of light on the nanoscale.

1.6 Conclusions

We have discussed the optical properties of different plasmonic materials, including a comparison of their predicted performance metrics in terms of quality factors. The comparative study shows that there is not a single clear choice for the best low-loss plasmonic material for all applications. Our comparison demonstrates that silver dominates all of the materials we considered in terms of its quality factors in LSPR and SPP applications in the visible and NIR ranges. However, silver is not the clear choice as a low-loss plasmonic material for other applications such as TO and superlens. Even though alkali metals and aluminum have high quality factors for TO devices and superlens, they pose processing challenges. Thus, silver is the best material for a superlens in the near UV. In NIR, AZO may be the best material for TO devices and superlensing, followed by ITO and GZO. Furthermore, these oxide semiconductors can work well at the telecommunication wavelength, which makes them very important substitutes for conventional materials such as gold and silver.

A materials quality factor describes how well a material performs, but it does not give insight into other aspects such as ease of processing and feasibility of integration. A final choice of materials requires a trade-off between quality factor, fabrication practicality, and cost. As an example, the material cost of gold and silver prohibit their wide-scale adoption in cost-driven markets such as photovoltaics.

With the rapid development of nanophotonics, it is clear that there will not be a single plasmonic material that is suitable for all applications at all frequencies. Rather, a variety of material combinations must be fine-tuned and optimized for individual situations or applications. While several approaches and materials have been presented, the problem of losses in plasmonic materials remains open-ended. An improved plasmonic material has the potential to make an enormous impact on both optics and nanoelectronics by allowing for a new generation of unparalleled device applications. We expect the comparative study presented herein to be useful in the elimination of poor choices, and it will serve as a guide in making the optimum choice for a low-loss plasmonic material in various applications.

2. NANOWIRES GROWN WITH GLANCING ANGLE DEPOSITION (GLAD)

Exploring and developing new and higher performance-based plasmonic materials is the first step for practical and realizable Transformation-Optics devices. However, many applications need non-conformal and films with gradient thicknesses that are not possible with traditional, top-down, 2-Dimensional fabrication. As technology moves forward towards Transformation Optics and other electronic technologies, innovation relies on new and 3D fabrication techniques.

2.1 Comparing Traditional PVD to GLAD

Physical Vapor Deposition (PVD) is an extremely common and developed technique used for depositing thin films on substrates. Using this technique, energy is added to the source material - causing it to evaporate under vacuum. The evaporated material will travel in a linear "line-of-sight" manner from the source to the substrate. The sample is typically held directly above the source material at an angle normal to the deposition. The films deposited in this manner onto the substrate will typically be planar and uniform in thickness due to the relatively even deposition flux across the substrate. When a mask is applied on the substrate, the line-of-sight nature of the evaporation will deposit material relatively evenly both on the top of the mask, and onto the substrate through the mask opening(s).

As opposed to typical deposition systems (where the sample's angle and rotation are fixed), Glancing Angle Deposition is a PVD process that allows full control over the angle and rotation of the sample. With these added degrees of control, many of the previous assumptions about the films deposited in PVD evaporation must be reconsidered when the sample is rotated and/or the flux is deposited at an angle.

Using Glancing Angle Deposition (GLAD), this line-of-site behavior can be exploited to produce a variety of films with non-planar geometries for new optical and electrical devices. For example, when the substrate is rotated to a large, glancing angle (above about 65°), nanowires will grow (not continuous films). When materials are deposited at an angle over a mask, non-planar films can be formed behind the mask. Similarly, when materials are deposited on an angle over non-planar structures, non-uniform structures can be created along curved surfaces. This fabrication approach shows great promise in the Transformation Optics and metamaterials community to develop materials with unprecedented control over the flow of light. A variety of interesting and exciting devices can be fabricated using this fabrication technique that would be difficult or impossible to do without it.

2.2 Background

Historically, most Glancing Angled Deposition (GLAD) fabrication has been focused on various types of nanowire fabrication. When a small amount of material is first deposited on a substrate, rather than forming a thin and continuous film, the material will begin by forming small islands. A good example of this process is when silver is deposited on a silica substrate. For those unfamiliar with Ag thin film deposition on Silica, the growth mechanisms involved are actually quite nontrivial, and have been studied extensively in the past. Due to surface energy differences between Ag and Silica, rather than forming a smooth continuous film, Ag will transition from small island formations to a percolated film, and eventually continuous films at around 0-10nm, 10-20nm, and 20nm respectively. When Ag is deposited on a Silica substrate at a glancing angle (larger than $\sim$65 °), a very different growth mechanism occurs. At low deposition thicknesses, islands will form at random locations on the substrate (similar to traditional evaporations). However, because the material flux is incident at such high angles, the small islands will cast shadows behind them blocking the silver from depositing onto these areas. Because this shadowing effect allows for the Ag to be deposited in some areas while not others, growth will only occur in the non-shadowed areas effectively creating nanowires. This growth mechanism is somewhat similar to the way in which trees grow in a forest. After the seeds are randomly arranged on the forest floor, only the seeds that get sun will grow into trees. As the trees become larger, they will capture more light, and continue growing, while those left in the shadow will no longer grow. An illustration of this nanowire growth mechanism is shown in Fig. 2.1.

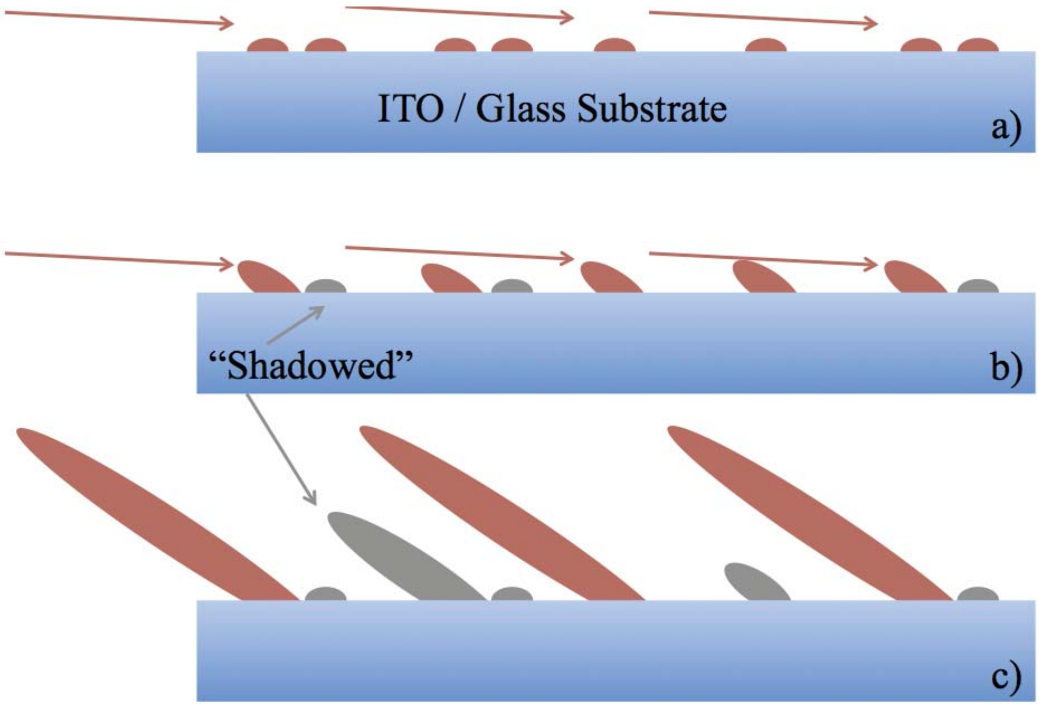

Fig. 2.1. Growth mechanism for nanowire growth using GLAD. The red arrows represent silver deposited at an oblique angle to the substrate. The red ellipses represent actively growing nanowires, while the gray ellipses represent the nanowires that have been shadowed and are no longer growing.

One detail of importance in Fig. 2.1 is that the nanowires grow parallel to one another, but not antiparallel to the incident flux (as might be expected). This angle of growth can be very roughly approximated using Eq. (2.1)

$$\beta = \alpha - arcsin\left(\frac{1 - cos(\alpha)}{2}\right) \tag{2.1}$$

where α is the angle of material deposition, and β is the angle of nanowire growth [42] but a more exact calculation for the growth angle would involve many other variables, including what material is deposited, vacuum pressure, substrate temperature, evaporation rate, etc.

Preliminary fabrication testing of nanowire growth was conducted by depositing silver on a silicon dioxide substrate. Simultaneously, wires were also grown on a silicon dioxide substrate with a very thin (15nm) ITO coating. Side- and top-views of this fabricated sample are shown in Fig 2.2. The side view displays the deposition angle, and the angle of wire growth. The top view shows nanowires with aspect ratios of more than 11:1.

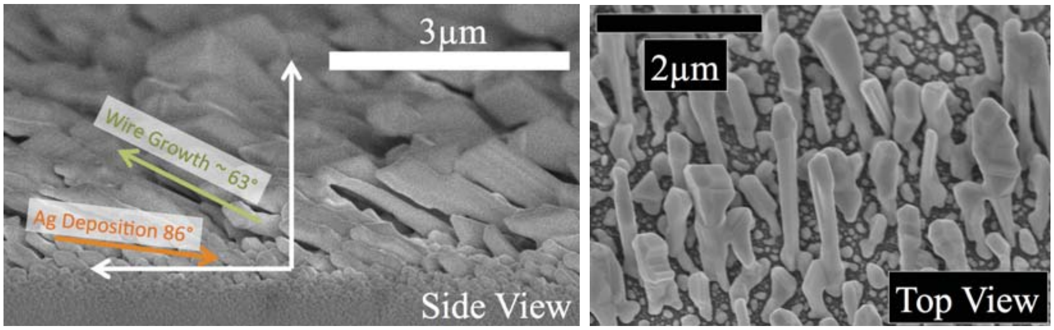

Fig. 2.2. Side and top views of the randomly grown array of Ag nanowires

2.3 Random Nanolasing

A laser/spaser can be created around randomly oriented structures that scatter light randomly. In the case where these random structures scatter light in a “loop”, an efficient feedback system can be formed. Gain medium surrounding these random structures can provide the required amplification when it is properly pumped. Silver nanowires grown with GLAD techniques can provide very large arrays of nanowires either randomly or periodically, and can act as a feedback system for random nanolasing. The strong scattering from the nanowires provide a high probability of forming a coherent feedback loop, depending on the length, density, and periodicity (random or periodic) of the structures.

In order to test the effect that length of the nanowires have on lasing, three different samples were fabricated with different amounts of material deposited (400nm, 700nm, and 1000nm). Due to the growth mechanisms described in the GLAD Fabrication Chapter 2 “Nanowires grown with Glancing Angle Deposition”, we know that over these deposition thicknesses, the randomly grown nanowires will change from randomly positioned and sized islands to very short nanowires, and finally to random nanowires with strong variation in lengths and structures. Images of the three fabricated samples are shown in Fig 2.3.

2.4 Experimental Results

The samples were then covered with R6G-PVA (10nM)and pumped using a Nd:YAG Laser (532nm, 800ps, 1Hz) using an optical setup shown in Fig. 2.4

The output intensity from the 3 different samples were measured and compared to a glass wafer without any nanowires grown on it. The results can be seen below in Fig. 2.5a. It is clear that the nanowires greatly enhance the lasing intensity, and that longer nanowires show a greater enhancement than the shorter wires. To further demonstrate the lasing effect, the samples were pumped with different powers and the output intensity was measured. Results from this study can be seen in Fig. 2.5b

These randomly arrayed nanowires clearly show the behavior expected of a lasing source. There is still ongoing work to determine some of the finer details of lasing in these structures. First, the lasing could be purely from the strong electromagnetic field enhancement that these nanowires are expected to exhibit, and not from a coherent feedback from the random wires. To completely understand this, simulations of the structures should be performed to determine the field behavior around indi-

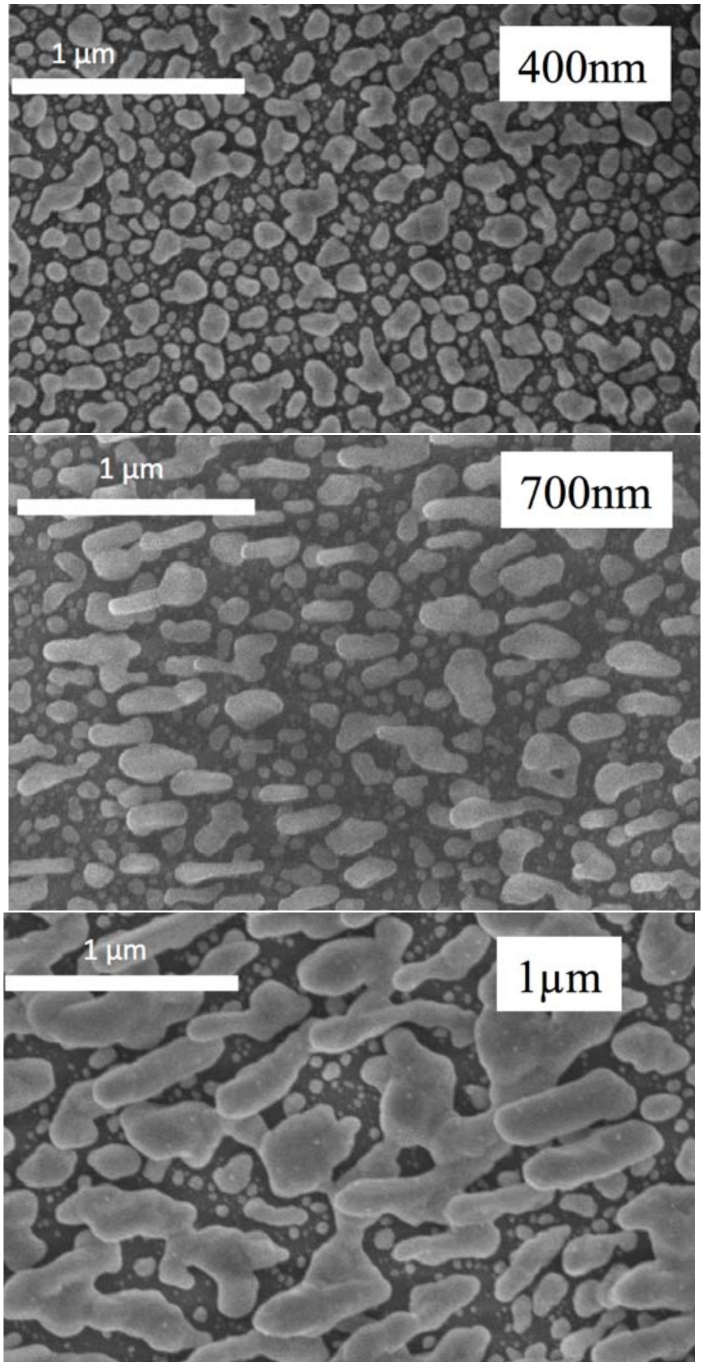

Fig. 2.3. Three nanowire samples grown by GLAD with three effective deposition thicknesses (400nm, 700nm, 1μm).

vidual and paired nanowires to understand how the field behaves with individual and paired nanowires. Secondly, the randomly arrayed nanowires should be compared

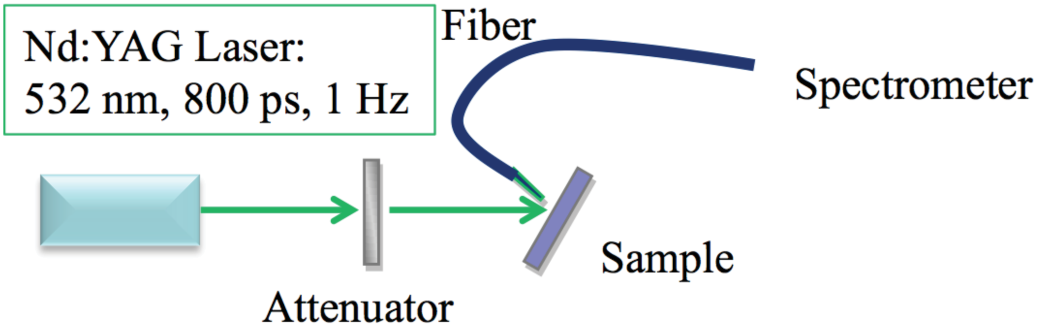

Fig. 2.4. The setup for nanolasing optical measurements

with nanowires of uniform periodicity. Comparing these structures and having strong simulation results should help us understand more precisely the nature of lasing in this nanowire sample

2.5 Advanced Nanowire Growth Techniques

While these linearly grown nanowires are interesting, they barely scratch the surface of what is possible with the GLAD system. Another relatively simple nanowire growth technique using GLAD that would be almost impossible with traditional fabrication techniques is a “chevron” nanowire 2.6. For this chevron geometry, the substrate was rotated 180° in the middle of the deposition. After the substrate is rotated, the continued GLAD deposition will continue growing the nanowires in the opposite direction. This technique can be repeated several times to create a “zig-zag nanowire.

If the substrate is rotated by small increments during deposition, a chiral or helical structure can be fabricated via Glancing Angle deposition. Here the substrate was rotated 90° in 10 small steps while the entire 2μm of silver was deposited. Rather than depositing the chiral structures randomly onto a flat substrate, Zinc Oxide wires were grown on a glass substrate by Professor Nicholas Kotov’s student Bongjun Yeom at the University of Michigan. The ZnO template and the silver nanowires grown on the template can be seen in Fig. 2.7. Because the deposition of the silver will only

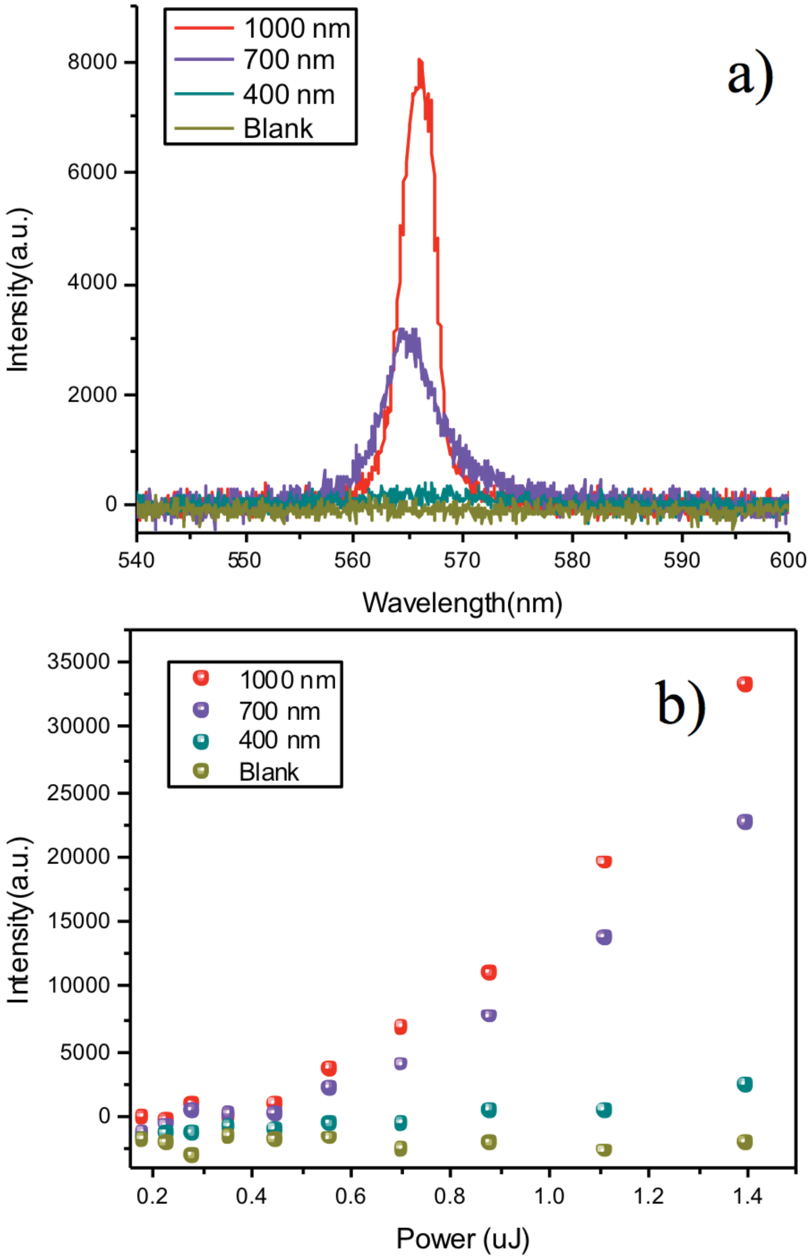

Fig. 2.5. a) The intensity spectrum for the 3 nanowire samples compared to a blank glass sample. b) The output intensity as a function of the input pumping power. Both curves show characteristic behavior for lasing

be on the topmost regions of the template (seen in Fig. 2.1), the wires will tend to grow only on the tips of the ZnO nanowires - acting as a quasi-seeding layer. In

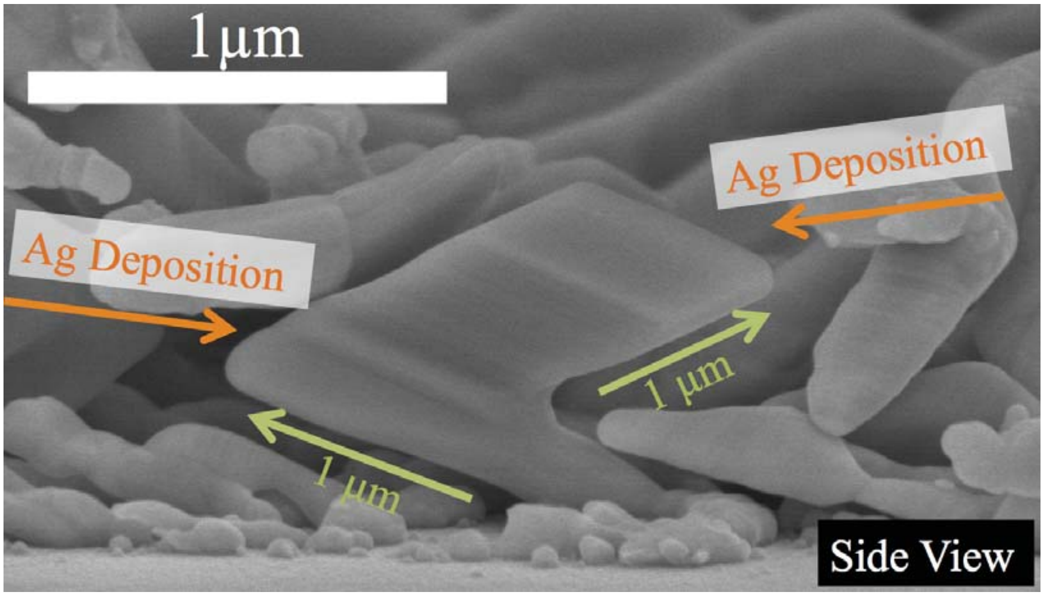

Fig. 2.6. "Chevron nanowire - grown by rotating the sample 180° in the middle of the deposition.

this figure, crystalline structure of the silver can be observed along the growth of the nanowire. While the nanowires grow due to the line-of-sight nature of the Glancing Angle Deposition, after the material is initially deposited, the atoms will tend to settle in a crystalline manner, rather than a purely "line-of-sight" fashion.

2.6 Nanowires Grown on a Seeded Template

Like trees randomly growing in a forest, the nanowires previously described will grow from random locations, and grow to different sizes and geometries. However, by properly seeding locations for the nanowires to grow, the fabricated structures will be uniform in period and geometry. This seeding can be accomplished by first creating a thin film of the material at desired locations on the substrate using traditional e-beam lithography. However, this seeding method must be approached carefully. Seeding the wires too closely will cast shadows that prevent neighboring wires from growing. Seeding the wires too far from one another will allow wires to grow from

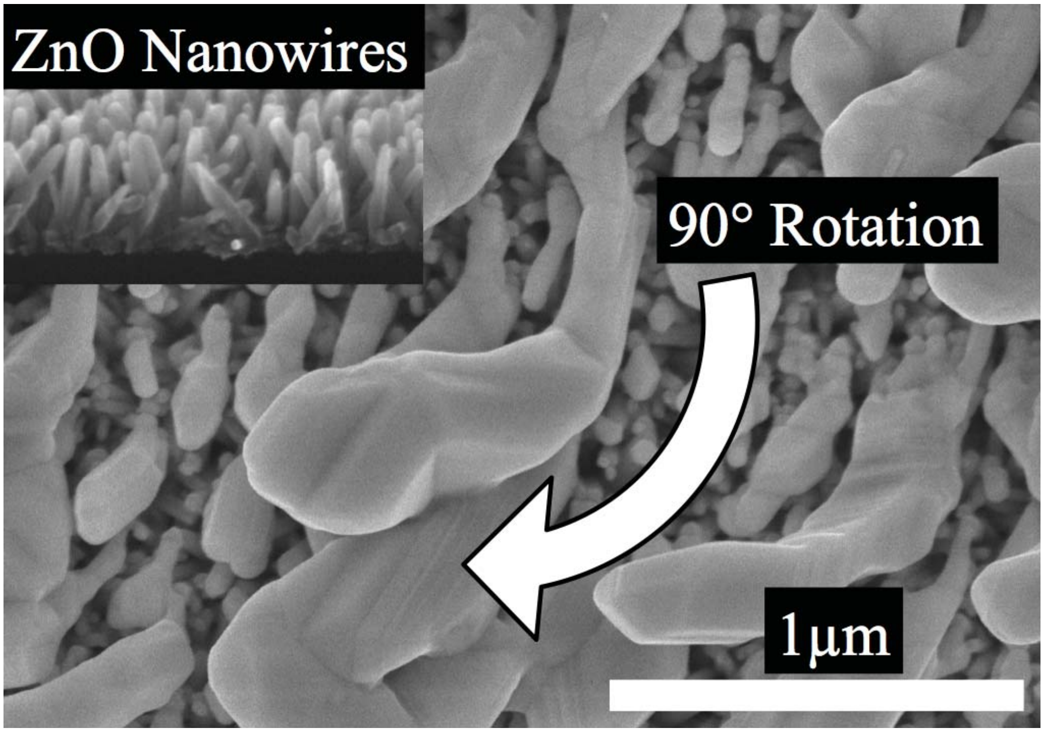

Fig. 2.7. Silver chiral structures with 90° counter-clockwise rotation grown on a ZnO nanowire template

undesirable locations. Size of the seeding area is also critical as a seeding area that is too large will allow several nanowires to grow from one location. Seen in Fig. 2.8, a seeded template of Hydrogen Silsesquioxane (HSQ) was made using e-beam lithography. Here, we see that the silver will grow only from this seeded template, and not from the flat substrate. The nanowires grown in this fashion are clearly more uniform in size, shape, and length.

2.7 Complex Nanowires from Previous Literature

Several techniques of Glancing Angle Deposition have been reported in literature [149–151]. These mentioned papers describe techniques for several advanced techniques exploiting the GLAD phenomena. While all the structures described above have been grown with silver on an un-cooled substrate, Glancing Angle Deposition

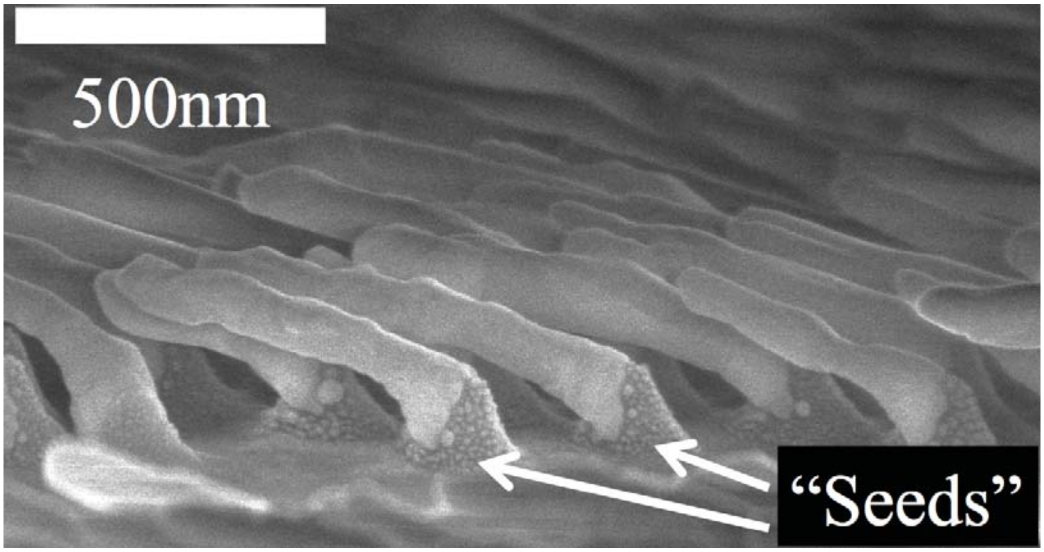

Fig. 2.8. Silver nanowires grown from a seeded template. As the nanowires only grow from the seeded template, their size is more uniform in size, shape, and length

can be exploited to make nanowires of more complexity by depositing materials will less surface energy on a cooled substrate. Fig. 2.9 shows several structures made from MgO on a cooled substrate. This combination allows for nanowire growth of higher aspect ratios of complex shapes, such as helices and chevron structures.

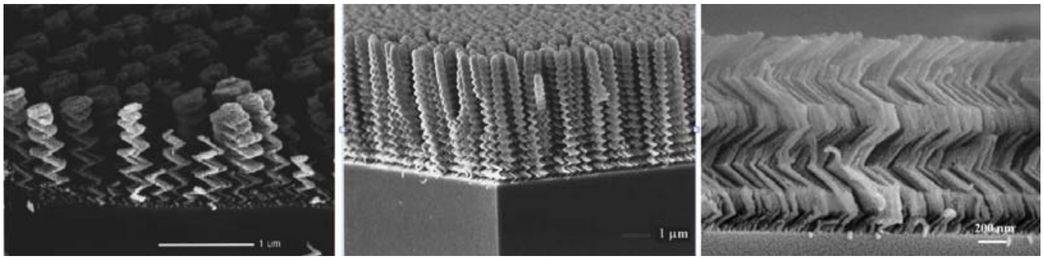

Fig. 2.9. Various types of nanowire growth via GLAD techniques

3. GLANCING ANGLE DEPOSITION ON CURVED AND SPHERICAL SURFACES

3.1 Introduction

When materials are deposited via PVD on curved surfaces, non-uniform films can be created. Using Glancing Angle Deposition (GLAD), the line-of-site behavior of physical vapor deposition can be exploited to produce a variety of films with non-planar geometries for new optical and electrical technologies. This fabrication approach shows great promise in the Plasmonics and Transformation Optics and metamaterials community to develop materials with unprecedented control over the flow of light. A variety of interesting and exciting devices - ranging from non-diffraction limited lenses to nanolasers can be created using this angled deposition that would be difficult or impossible to do without this technique.

3.2 Angled Deposition on Curved Surfaces

In physical vapor deposition, the source material will be evaporated in a “line of sight” manner, and the film deposition thickness is determined (in large part) by the effective surface area that is exposed to the source material being evaporated. In the case of a planar substrate, film thicknesses will be uniform because the effective surface area is constant. However, in the case of a non-planar surfaces, the amount of deposited material will change with the effective surface area. For example, in the case of spherical particles, the material deposited at an angle normal to the particle will receive the full amount of deposited flux, the edges of the particle will receive only a glancing (close to zero) amount of material, and there will be some distribution in film thickness across the sphere. An example of the thickness gradient created when a material is deposited at an angle on a sphere is shown in Fig. 3.1. By rotating the angle of the substrate, an angled deposition can be performed at any angle (between 0° and 180°) over the spherical particle to create this curved distribution of film thickness from any angle around the sphere.

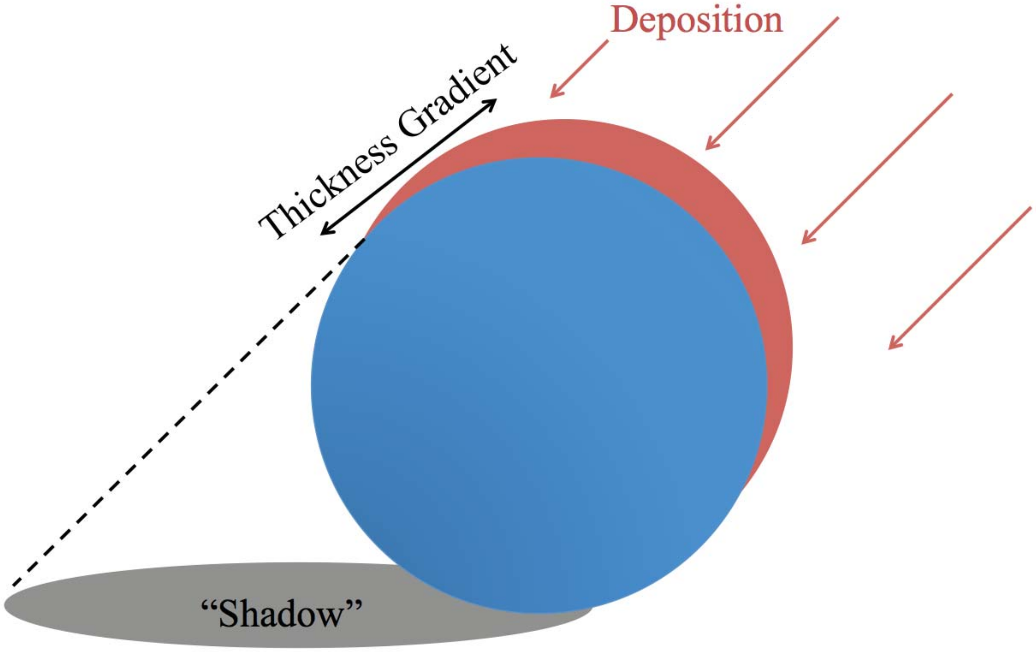

Fig. 3.1. Schematic of angled PVD deposition on a spherical surface. A gradient in thickness is created due to the varying amounts of surface exposed at the angle of deposition

As an example of this film thickness gradient, Fig. 3.2 shows the result of depositing 40nm of silver on a 5μm SiO_2 microsphere at an angle of 45°. The growth dynamics of silver films on SiO_2 has been studied in depth and thin film formations has been previously analyzed. When the effective deposited thickness is below 10nm, silver will form isolated "islands". When the effective thickness is around 10nm, the film will become percolated, and when the effective thickness approaches 20nm, the film will become continuous. In Fig. 3.2 we see a clear effective thickness gradient of deposited silver across the microsphere. Because the total deposited film on the sphere is 40nm, the entire spectrum of this film growth can be seen along the film, from a continuous layer on the upper right (∼20nm), through the percolated film, islands, and eventually uncoated SiO_2.

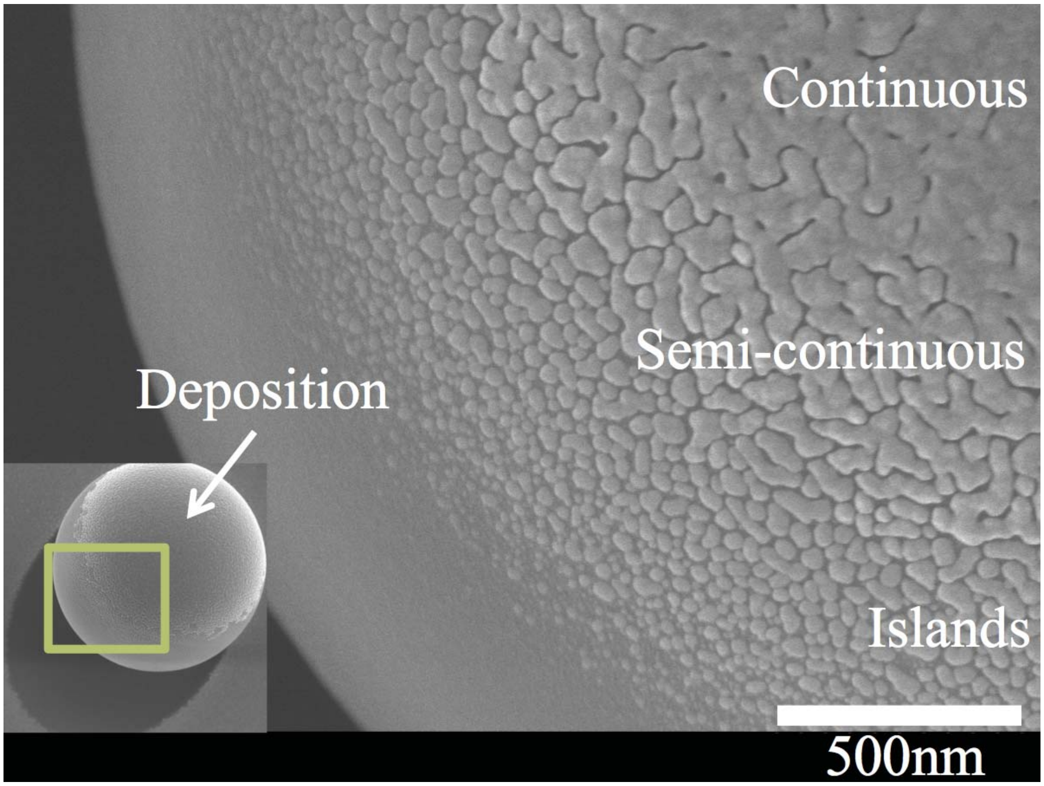

Fig. 3.2. A 40nm silver deposited at a 45° angle over a 5μm SiO_2 microsphere. A distribution in effective thickness can be seen ranging from no coverage through full continuous coverage.

Multiple layers of different materials can be deposited in this manner to create "core-shell" structures of alternating materials. By depositing each material at a large angle ($\sim 86°$) and continuously rotating the substrate during deposition, the outside edges of the sphere will be coated with continuous films, while the top of the structure will receive a glancing deposition of material. As noted in section 2.2, nanowires can be grown by depositing the source material at large angles close to 90° and care must be taken to prevent these wires from growing at the glancing angles (top of the sphere). If silver is deposited directly onto SiO_2 at large angles, the silver films will have very rough and discontinuous surfaces, even with larger deposition thicknesses. In Fig. 3.3, five alternating layers of silver and SiO_2 are deposited on a 5μm microsphere at an angle of 86° without germanium wetting layers. Despite their relatively large total deposited thicknesses (100nm), the films are extremely rough and discontinuous. At the top of the structure (Fig. 3.3b), the films are especially rough due to the shadowing effects occurring at glancing angles (similar to nanowire growth).

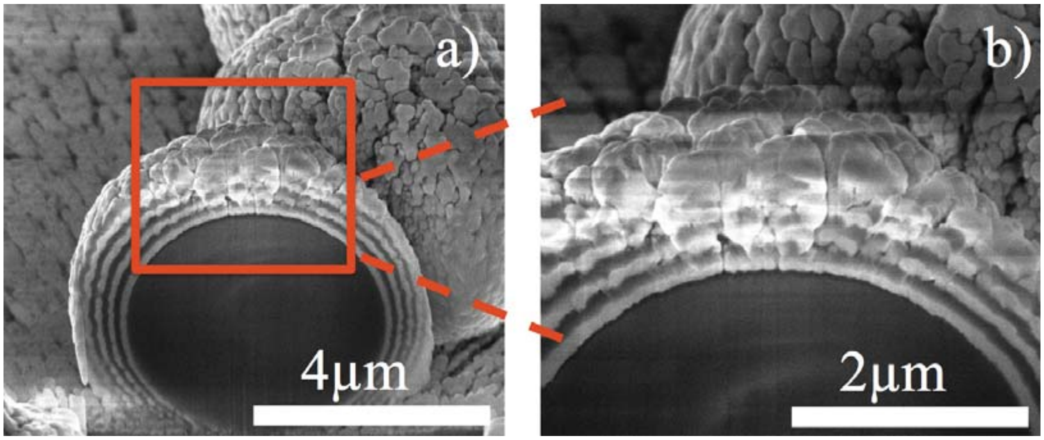

Fig. 3.3. Deposition of silver on SiO_2 microsphere without germanium wetting layer. Despite the films' relatively large thicknesses, layers are rough and discontinuous. The top of the structure is especially rough, due to the shadowed, "nanowire"-like growth of the films at sharp glancing angles

Because of its prominence in the optical community as an outstanding optical and plasmonic material, great effort has been invested into developing techniques for depositing silver films as thin as possible. One technique allowing for smooth and continuous silver film growth on SiO_2 is by depositing a very thin ($\sim$ 1nm) germanium wetting layer before the silver. This wetting layer promotes thin and continuous growth of silver on SiO_2 down to thicknesses below 7nm. To create continuous and uniformly deposited films on spheres, special measures must be taken into account during deposition. Firstly, the sample must be rotated for a short time to deposit a small thickness of material over the area of discontinuous growth. Depositing small amounts of material over these small islands that will form in regions of glancing deposition angles will smoothen the regions surface and prevent nanowires from forming. Secondly, employing a wetting layer (germanium) allows for more smooth films of silver, which will help with surface roughness and minimize nanowire growth on the top of these structures. An example of such a core-shell structure can be see in Fig. 3.4. Here, 1nm germanium wetting layers were applied between each silver/SiO_2 interface, and the deposition angle was continually changed during the substrate rotation to provide continuous and relatively smooth layer coverage, despite the layer thicknesses being relatively thin (just $\sim$13nm)

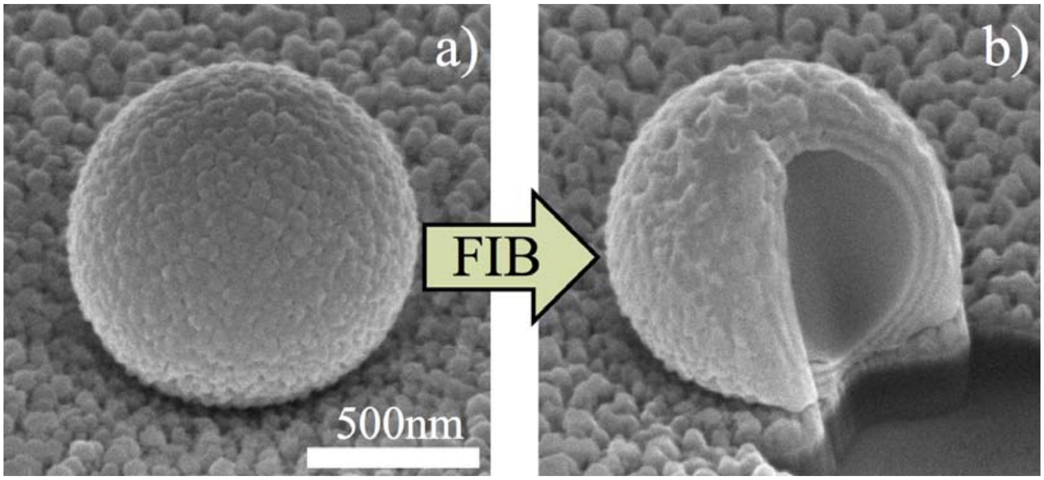

Fig. 3.4. 1μm SiO_2 microsphere before (a) and after (b) FIB cut. Although layers are only $\sim$13nm each, they remain relatively smooth and continuous

There has been recent interest in the optics community of making non-uniform layer thicknesses on curved surfaces for devices such as a planar hyperlens and optical concentrator. By depositing materials at glancing angles onto the microspheres, it is possible to create films that have a greater thickness on the sides of the sphere and taper to thin films on the top of the sphere. Fig. 3.5 shows such a sphere with tapered thicknesses across the side and top of a sphere. These curved layers of varying thickness can be fabricated by depositing alternating layers of silver and SiO_2 at glancing angles (86°).

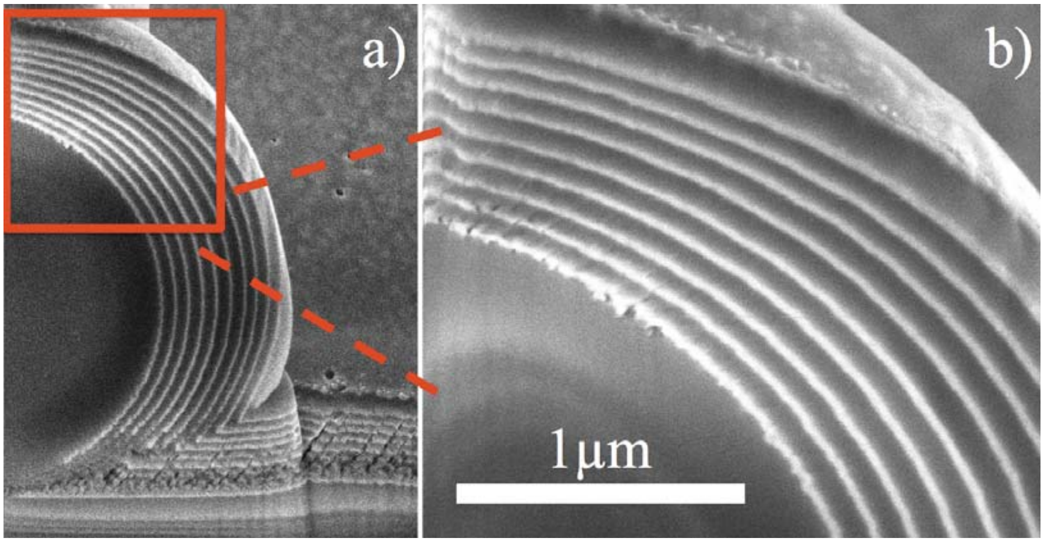

Fig. 3.5. Gradient film thicknesses around a 5μm microsphere. Fig.3.5a shows the entire microsphere, while Fig.3.5b is an inset of the sphere, showing the difference in film thicknesses between the top and sides of the sphere.

3.3 Comments

When growing thin films on curved surfaces, there are several additional notable effects that must be taken into consideration beyond the purely "line of sight" nature of the deposition. First, surface diffusion will have an impact on the final structure. The effects of surface diffusion is nontrivial and depends on several variables, including the material properties of the deposited material and its underlying layer, substrate temperature, and deposition rate. While employing germanium as a wetting layer will improve the growth of silver on SiO_2, other parameters (such as substrate temperature monitoring and cooling) are not available for observation or manipulation in this system. Secondly, it should be noted that although material can be deposited all around the outside of the sphere, there will always be an opening at the bottom of the sphere, where no material can be deposited. This opening can be seen in the bottom of Fig. 3.5a. Third, only the deposition onto the *sphere* has been discussed in this chapter. In practice, deposition on the substrate around the sphere (see, for example Fig. 3.5) is unavoidable and its existence should be accounted for in device design.

4. SHADOWED ANGLED DEPOSITION FOR THICKNESS TAPERED THIN FILM HYPERBOLIC HYPERBOLIC METAMATERIALS AND WAVEGUIDES

4.1 Introduction

Typically, in Physical Vapor Deposition (PVD) grown thin films, layers will be deposited at an angle normal to the substrate, which creates planar films that are uniform in thickness. However, when a source material is deposited in a PVD evaporation at an angle over a mask, a "shadowed" region is created behind the mask. This region will have a gradient amount of material deposited over the mask, which will lead to a gradient in film thickness across the substrate. A schematic of this angled shadowed deposition technique is shown in Fig. 4.1. While this concept may seem trivial, the ability to create non-planar films of non-uniform thicknesses enables a new field of nanofabricated devices with a higher degree of control over deposited films' thickness. This fabrication technology enables a family of devices with smooth gradients in electrical and optical properties. This chapter will explain how multilayered films of alternating metal/dielectric layers can be fabricated with tapered thickness profiles, and chapter 6 discusses two examples of a device that requires this fabrication technology.

4.2 Tapered Silver Films on Uniform SiO_2

As a source material is deposited at an angle over a mask via PVD, a gradient in deposited layer thickness can be deposited (Fig. 4.1). The first type of shadow deposited film described is a multilayered metal (silver)/dielectric (SiO_2) structure

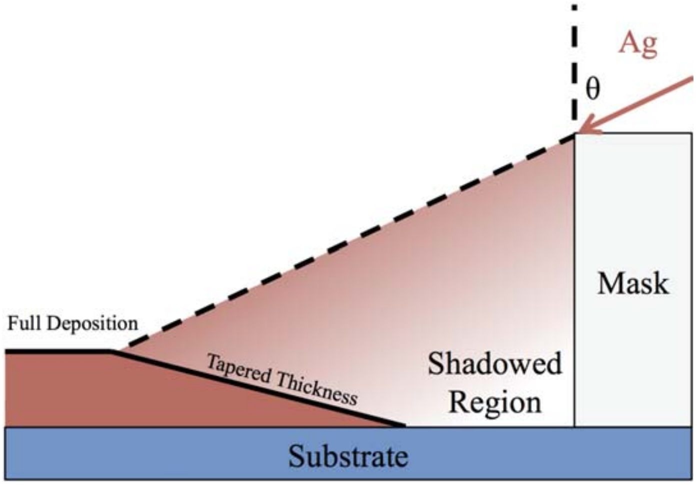

Fig. 4.1. Depositing material at an angle over a mask will produce a shadowed region behind the mask with a tapered deposition thickness profile.

where the silver thickness tapers from 20nm down to 0nm (continuous below 7nm), and the SiO_2 thickness is a constant 58nm across the substrate.

First, a Kapton® tape mask ($\sim 60\mu$m) is applied to the glass substrate before loading the sample into the chamber. Upon loading the sample , a 1nm germanium wetting layer is deposited at an angle normal to the substrate (0°). Next, the sample is rotated to 20°, and a 20nm silver film is deposited. By depositing the silver film at an angle, a "shadowed" region is present behind the Kapton® tape mask, which will receive a distribution of deposited material. Regions of the sample that are more than 20° from the top of the tape will receive the full 20nm of deposited silver. Regions of the substrate below 20° will receive a distribution of deposited material. As a combination of this gradient of flux and surface diffusion, the shadowed region behind the tape will have a silver film whose thickness tapers between 20nm down to 0nm. SiO_2 can then be deposited normal to the substrate to create a film of uniform thickness (or at an angle to create a film with gradient thickness). The process can then be repeated many times to create multilayer structures with aligned tapered thickness films.

The length of this tapered region may be increased by rotating the angle of flux during the deposition. For example, holding the substrate at 20°, but sweeping ± 2° will increase the length of the tapered region of the film. Fig. 4.2 shows layers of silver tapering in thickness from 20nm down to zero, while the SiO_2 layer thicknesses remain constant at 58nm. Here, 45 layers in total were deposited (15 each of SiO_2, Ge, and Ag).

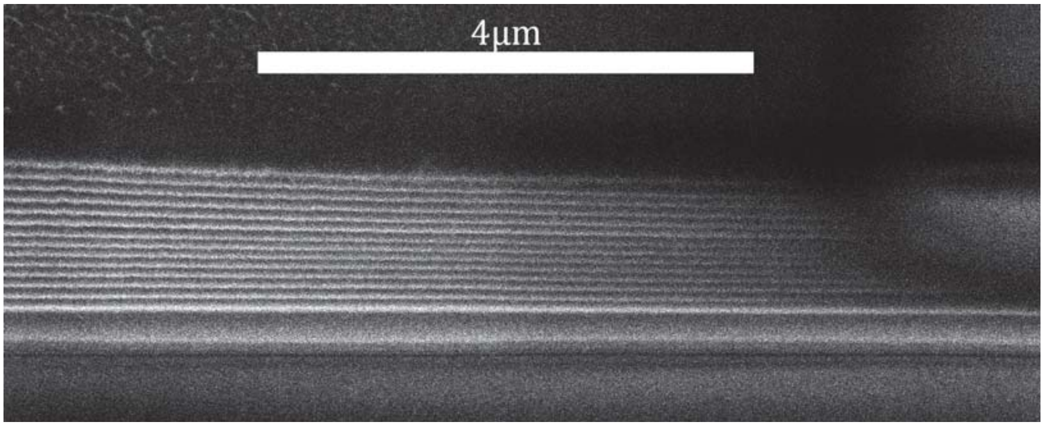

Fig. 4.2. Alternating metal / dielectric layers with subwavelength thickness

4.3 Tapered SiO_2 films on Uniform Silver

While the previous section described a technique for creating a gradient films with thicknesses tapering down to zero, here focus is on continuous films with non-planar and non-uniform thicknesses. Rather than tapering the thickness of the silver film, the SiO_2 thickness is tapered in this case. Using similar angled deposition techniques, these films may also be realized.

By adjusting the thickness of one material (dielectric), while keeping the thickness of the other material constant, the *effective* properties of the composite material vary with their relative filling fraction. The fabrication of this class of material begins similarly, with a mask over which the materials are deposited. In this case, each material is first deposited at a normal angle (0°) to the substrate. After the desired thickness for one part of the structure (thickness 1) is achieved, the deposition angle is rotated, creating a shadowed region with tapered thickness. The material continues to be deposited at this angle until the final thickness of the second part of the structure (thickness 2) is achieved. Through these means, a two (or more) sectioned effective metamaterial can be fabricated with smooth transitions between sections. Fig 4.3 shows such a fabricated structure. Here, there are 15 layers each of silver and SiO_2 (with 15 germanium wetting layers). The silver films here have a uniform thickness of 10nm across the entire structure, while the SiO_2 thickness varies between 30nm and 100nm. This change of thickness changes the metal filling fraction, which in turn changes the effective permittivity of the material in the in-plane and out-of-plane directions.

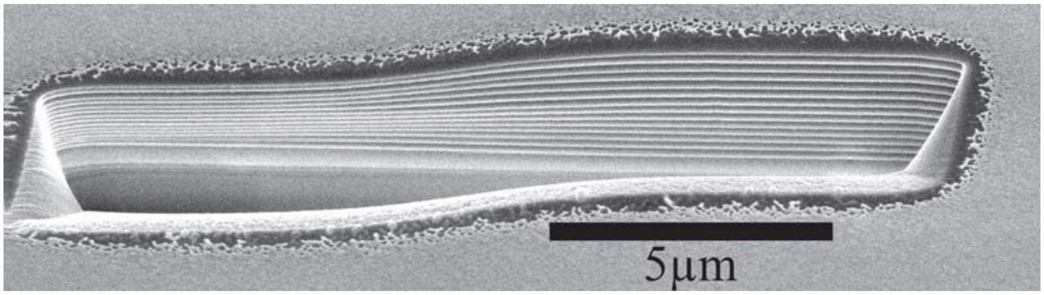

Fig. 4.3. 15 alternating silver/SiO_2 layers. Each silver layer has a uniform thickness of 10nm. Each SiO_2 layer has a thickness that tapers between 30nm and 100nm

The strong change in metallic filling fraction across the substrate is enough to make the material's in-plane permittivity an effective positive (dielectric) at one side (thick) of the structure, and an effective negative permittivity (metal) on the other (thin) side of the structure. This strong change in effective optical properties of the film have very interesting properties for a field or wave passing along this adiabatically tapered film.

4.4 Planar Magnifying Hyperlens

One exciting application for the fields of Transformation Optics and metamaterials is to develop devices with resolution less than the diffraction limit. Feature sizes less than the diffraction limit have their spatial information contained in waves with large wave vectors or k-vectors. Because normal dielectric materials (such as air, glass, etc.) only allow waves with finite (and relatively small wave vectors) to propagate through them. In contrast, hyperbolic metamaterials (HMMs) *do* allow large k-vectors to propagate through them. While the large k-vectors can propagate inside the HMM, they cannot propagate through air, as the high-k waves are evanescent, and lost in the far-field. Rather than using planar HMM layers, the layers can be curved to magnify the image of the object. If there is enough magnification to bring the feature sizes of the object larger than the diffraction limit, the features can indeed propagate into the far-field, where they can be detected through conventional optical techniques. Therefore, a magnifying hyperlens can provide resolution much below the diffraction limit in the far-field. While a magnifying hyperlens has been demonstrated using a curved, cylindrical structure, there remains a desire to have a hyperlens that is planar, such that it can be more easily integrated with conventional optical microscopes. For this reason, we have developed a metamaterial that has hyperbolic dispersion (to allow high-k waves to propagate), curved on one side (to provide the required magnification), and planar on the other side (to easily integrate into conventional optical systems).

4.5 Design and Fabrication

As discussed previously in Section 4.3, a wedge-like structure can be fabricated that is hyperbolic, curved on one side, and planar on the other side. As the curvature of the layers will determine the device's magnification, the curvature should be as large as possible. As can be seen in Fig. 4.3, the final curvature (and magnification) of the structure will become larger as more curved layers are consecutively stacked upon one another. Unfortunately, because the metal (silver) used in the HMM is lossy, more added layers will lead to more loss. Therefore, there is a direct tradeoff in this structure between magnification and internal losses (depending on the metal used).

4.6 Simulations and Remarks

While this fabrication technique of making the curved wedge structure does provide magnification, limitations in the fabrication process dictate the limitations of the final curvature of the structure. Because the structure in Fig. 4.3 is the largest curvature achievable with this technique, we used this structure to simulate the amount of achievable magnification. Using a COMSOL FEM model, the HMM structure was simulated with two slits in a chromium (used for blocking the light) mask. Here, the two slits are separated by a distance of 1100nm. One of the slits is on the flat region, where the feature will travel straight through the structure, while the other slit is positioned on the curved part of the structure, where its features will be magnified. The image is detected in the far-field, and the magnification can be defined as the ratio between the separation of the two slits, and the separation of the two intensity peaks detected in the far-field. Upon simulating this structure, the results can be seen in Fig. 4.4.

These simulations are useful, but unfortunately do not provide the results we hoped for. On one side of the wedge, the two slits are separated by 1100nm. Upon passing through the HMM wedge structure, the separation in intensity peaks is approximately 1300nm. While there is some magnification, it is only a factor of about 1.18, or 18% larger. As previously mentioned, adding more layers to this structure would indeed increase the magnification, unfortunately, it would also provide greater losses, to which this device is already very sensitive. In conclusion, while this device does, in principle demonstrate magnification is possible, the magnification is not nearly enough to be useful in a practical device. However, using metallic films

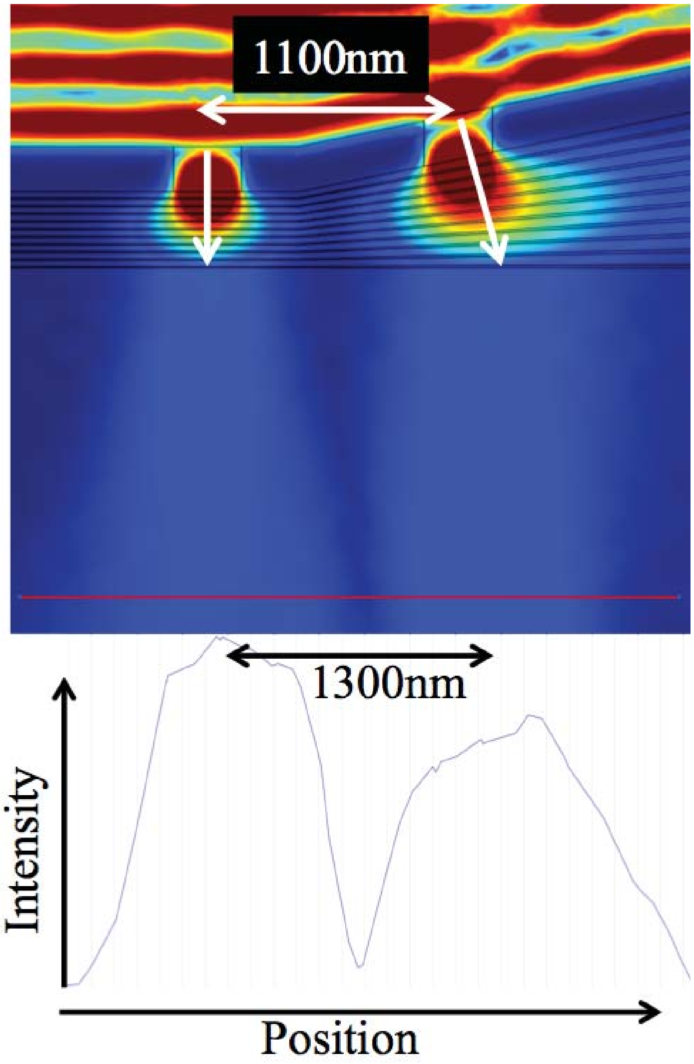

Fig. 4.4. Simulations used to calculate the magnification induced from the HMM wedge structure.

with lower losses would allow one to increase the number of layers used, which could provide the greater curvature needed for a planar magnifying hyperlens.

5. INTRODUCTION TO HYPERBOLIC METAMATERIALS

Bulk materials have a dielectric permittivities $\epsilon(\lambda) = (\epsilon' + i\epsilon'')$. While the real part of the dielectric function (ϵ') describes the strength of the polarization induced by an external electric field, the imaginary part (ϵ'') describes losses associated with the materials electric response. Metals (by definition) have a negative ϵ', due to their free-electron behavior at the wavelength of operation, while dielectric materials have (by definition) a positive ϵ'. By stacking alternating layers of metal and dielectric with subwavelength thicknesses (Fig. 5.1), this "metamaterial" exhibits effective permittivities in the in-plane and out-of-plane directions, which can be approximated by Effective Medium Theory (EMT). Here, the permittivity in-plane (x-y, or $\epsilon_{\|}$) can be approximated by Eq.(5.1), the out-of-plane permittivity ($\epsilon_{\perp}$) can be approximated by (5.2), and the relationship between k-vectors in the 3 directions is described by Eq. (5.3).

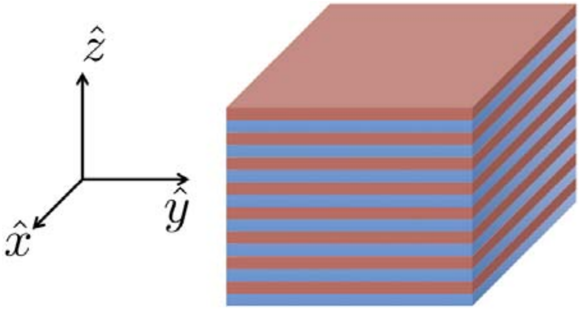

Fig. 5.1. Alternating metal / dielectric layers with subwavelength thickness and coordinate system used.

$$\epsilon_{\|} = f_m \epsilon_m + (1 - f_m)\epsilon_d \tag{5.1}$$

$$\epsilon_{\perp}^{-1} = \frac{f_m}{\epsilon_m} + \frac{1 - f_m}{\epsilon_d} \tag{5.2}$$

$$\frac{k_x^2 + k_y^2}{\epsilon_{\perp}} + \frac{k_z^2}{\epsilon_{\parallel}} = \left(\frac{\omega}{c}\right)^2 \tag{5.3}$$

In these equations, ϵ_m is the real part of the permittivity of the constituent metal layers, while ϵ_d is the permittivity of the dielectric layers. The variable f_m is the volumetric metal filling fraction, $\epsilon_{\parallel}$ is the permittivity in the in-plane ($\hat{x}$ and $\hat{y}$) directions, and $\epsilon_{\perp}$ is the permittivity in the out-of-plane ($\hat{z}$) direction. One can see from these equations that as the metal filling fraction is increased, the effective permittivities will eventually become negative. In the range where the in-plane permittivity is negative and the out-of-plane permittivity is positive, the dispersion relation between k_y and k_z will exhibit a hyperbolic profile. One-quarter of a cross-section of the dispersion relations for air, SiO_2, and an HMM are shown in Fig. 5.2.

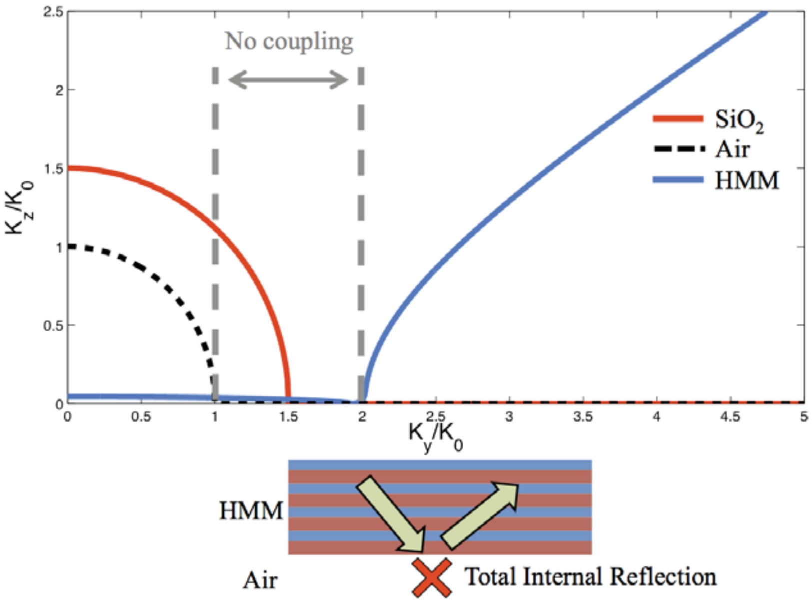

Fig. 5.2. Dispersion relations for air, SiO_2, and an HMM structure, demonstrating how waves propagating in the $\hat{z}$-direction cannot be coupled to air or SiO_2 because the y-components of the wave vectors cannot be matched.

Simple dielectric materials, such as air and SiO_2, have ellipsoidal (or spherical) dispersion relations. Waves propagating in these media have relatively small wave-vectors that are bound to their dispersion curves. The name “Hyperbolic Metamaterial” comes from the shape of the dispersion profile for this class of materials, which is a hyperboloid as shown in Fig. 5.2. The hyperbolic dispersion relation illustrates how an HMM can support unbounded k-vectors that can be extremely large in magnitude.

For these reasons, HMMs have been of great interest to the optics community, and have been used for several devices with unprecedented optical performances. The resolution of conventional optical systems is limited by the Abbe diffraction limit. In these systems, the resolution is limited by Eq. (5.4). Feature sizes smaller than d have large k-vectors that will evanescently decay in media that cannot support the large-k wave vectors. Because HMMs *do* support large k-vectors, subwavelength features are preserved when traveling through the HMM. By curving the planar HMM layers into a cylindrical structure, the features can be magnified to sizes above the diffraction limit and these low-k waves can propagate into the far-field. In this way, sub-diffraction limited features can be imaged in the far-field - a device known as a hyperlens.

$$d = \frac{\lambda}{2nsin(\theta)} \tag{5.4}$$

As the photonic density of states (PDOS) is proportional to the volume of the shell enclosed between two isofrequency contours in the k-space, HMMs can have a PDOS that is much greater than that of dielectric media. An emitter’s spontaneous emission is determined by the surrounding material’s PDOS. An HMM can provide a coupled emitter with a nearly infinite broadband set of additional decay channels that can ultimately enhance the emitters spontaneous emission through the Purcell effect. Because the PDOS is proportional to the maximum k-vector in the surrounding medium cubed ($PDOS \sim k_{max}^3$), every small increase in the maximum wave-vector in the system can lead to a drastic enhancement of the PDOS. This approach has produced valuable results towards improving the efficiency of broadband single photon sources (such as Nitrogen Vacancy centers in nanodiamonds) [152]. However, the high-k modes, which are evanescently coupled into the HMM are very difficult to outcouple, due to a very large momentum mismatch. The next Chapter 6: "Tapered Hyperbolic Metamaterial Waveguides" is devoted to designing, simulating and fabricating a device that drastically enhances an emitter's PDOS, *and* provides an efficient method for outcoupling the high-k waves.

6. TAPERED HYPBERBOLIC METAMATERIAL WAVEGUIDES

6.1 Introduction

Due to the extremely large Photonic Density of States (PDOS) of HMMs, they have the potential for drastically enhancing the spontaneous emission rate of single-photon emitters. Using HMMs for enhanced single-photon emission has been previously studied [152], and a two-fold increase in emission rate was measured by placing the single-photon emitters in close vicinity to a TiN/AlScN structure exhibiting hyperbolic dispersion. While placing the emitters above an HMM clearly enhances the emission rate of single-photons, the enhancement goes into high-k waves of the HMM and cannot be detected in the far-field. One proposed method for extracting the high-k waves from the HMM is by surrounding the emitter by a "bulls-eye" grating structure [153]. This technique should be avoided as it is narrow-band, and does not take full advantage of the broadband nature of HMMs.

6.2 Outcoupling High-k Waves from HMMs

One of the distinguishing characteristics of HMMs is that they support propagation of high-k waves. However, the challenge in taking full advantage of these materials is the extracting (out-coupling) these high-k waves into free space. Fig. 6.1a illustrates this problem. For a wave incident on a material in the $\hat{z}$-direction, the in-plane (x- and y-component) of the field must be conserved. It is therefore impossible to couple light between the HMM and air or SiO_2, as the k-vector cannot transfer between the materials while conserving k_y (Fig. 6.1). A wave at this HMM/dielectric interface will be evanescent, and quickly decay.

In contrast to waves propagating in the $\hat{z}$-direction, waves propagating in the $\hat{y}$-direction must conserve the z-component of the k-vector. In this case, it *is* possible to couple light between HMMs and dielectrics such as air and SiO_2 while preserving the z-component of the wave-vector. In figure 6.1a, we can see that coupling is possible when the magnitude of the $\hat{z}$-component of the wave is less than that shown in the green dashed line.

Typically, dielectric materials and HMMs are classified as two distinct material groups. However, here we examine the behavior of these metamaterials as they transition between dielectric and HMMs by varying the constituent metal filling fraction. Figure 6.1b shows the dispersion relation for HMMs of different metallic filling fractions, ranging from 0% (pure dielectric) to 35% (clearly HMM). This figure assists in the understanding of waves propagating in and between metamaterials of different metallic filling fractions.

For waves propagating along the HMM in the in-plane ($\hat{y}$) direction, the k_z component of the field must be conserved. As the field traverses between materials, the k-vector will pass between dispersion curves in a horizontal manner, as shown in Fig. 6.1b. From this figure, it can be seen that wave vectors transform from k_3 to k_2 as the metal filling fraction changes between 23% and 35%. The wave vector can also transform from k_2 to k_1 as the wave passes from the HMM with 35% filling fraction into air (along the green line in Fig. 6.1b). It *is* possible for wave vector k_3 to directly convert into k_1, however, this coupling transition will have higher reflective losses (as reflection is determined by the difference in magnitude of k-vectors).

While extracting light from the HMM into air is clearly important, the enhancement of the PDOS must also be analyzed. The enhancement of the PDOS is proportional to the cube of the maximum k-vector of the surrounding HMM (k^3_{max}). Wave vector k_3 is larger in magnitude than k_2 and will have a significantly larger enhancement of the PDOS. Likewise, k_2 will have a significantly enhanced PDOS compared to k_1. While considering the possibility of using these single photons in a practical device however, outcoupling these high-k waves must be considered. While k_3 shows greater enhancement, outcoupling the enhanced modes of vector k_3 into free space is very inefficient due to the large wave vector mismatch between k_3 and k_1. Conversely, vector k_2 has better coupling efficiency to k_1, but a much lower enhancement of PDOS (compared to k_3). Ideally, one would like a metamaterial waveguide that can exploit the benefits of both filling fractions of HMMs. This can be accomplished with a waveguide where one end would have a maximum enhancement of PDOS, and the other end of the waveguide would have optimal coupling between the HMM and free space. Between the two HMMs, a smooth transition would provide a medium for the large k-vectors to be converted into low-k vectors while eliminating reflective losses by adiabatically tapering the metal filling fraction of the HMM.

While a tapered waveguide can be designed to optimize the outcoupling of high-k waves into free-space, these structures can also be used to quench the high-k modes traversing through a tapered waveguide. In the previous example, high-k waves are first created in the HMM region of lower metal filling fraction, and are converted into lower-k modes as they pass into the HMM with higher metal filling fraction. By using the waveguide in a reverse manner and decreasing the metal filling fraction (greatly increasing the magnitude of the wave vector), high-k waves of an HMM can be quench. By introducing high-k waves into the HMM in a region of high metal filling fraction, the waves can pass along the waveguide into a region with lower metal filling fraction (eg. from vector k_2 to k_3 in Fig. 6.1b). In this case, the magnitude of the k-vector will grow very quickly into very high-k modes, where the energy will quickly be quenched as the metal filling fraction approaches zero.

The goals of this work is to demonstrate that high-k waves can be coupled out of HMMs, and finally, to demonstrate a waveguide that can optimize *both* enhancement of PDOS, *and* outcoupling into free-space. Using a similar design, a parallel goal is to demonstrate an adiabatically tapered waveguide with decreasing metal filling fraction will quench the high-k waves passing through.

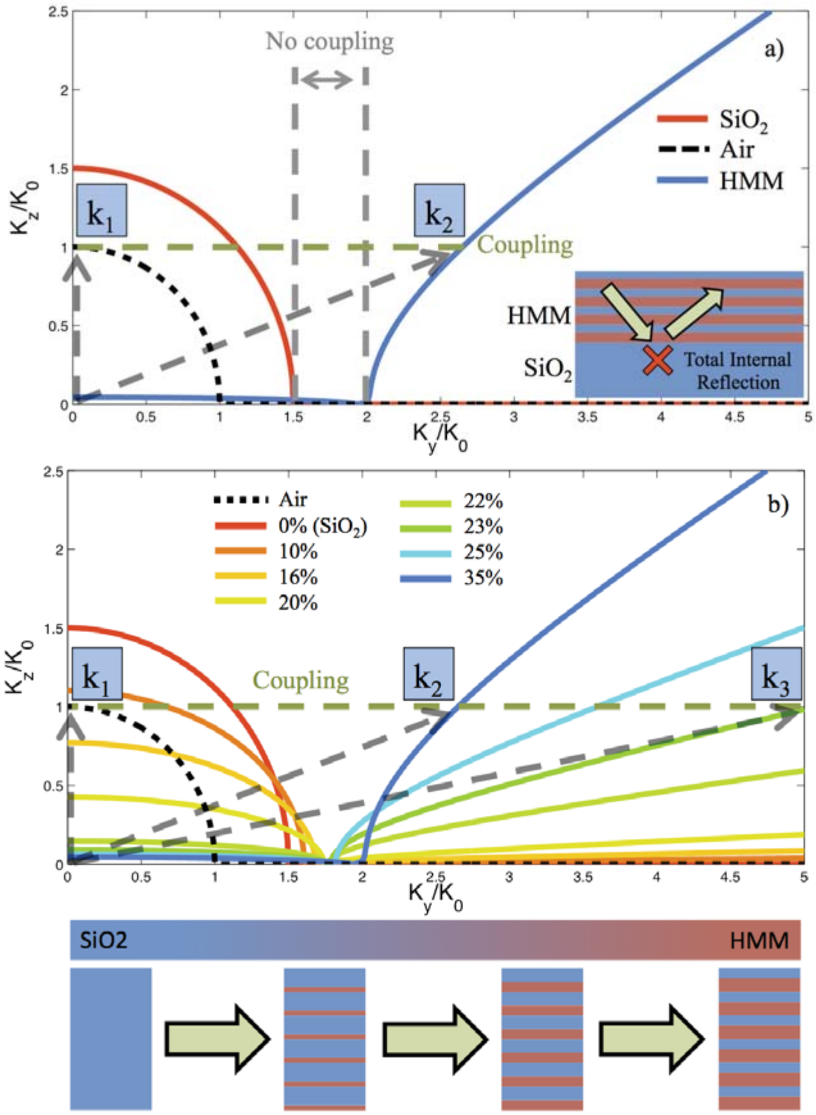

Fig. 6.1. Dispersion relations for various dielectric and HMM structures. Fig. (a) demonstrates how waves propagating in the $\hat{z}$-direction cannot be coupled to air or SiO$_2$. Waves propagating along the y-axis *can* be coupled to SiO$_2$ or air, as they have matching $\hat{z}$-components of their respective wave-vectors. Fig. (b) shows how the dispersion relation for various dielectric and HMMs change as a function of metallic filling fraction.

6.3 Design

From of Fig. 6.1b, it is evident that HMMs with lower filling fractions are better for supporting and propagating very high-k waves, while HMMs with higher filling fractions will couple into free-space more efficiently. The design for the adiabatically tapered HMM waveguide will therefore proceed as follows: First, an HMM is chosen with a metal filling fraction for an optimized enhancement of the PDOS. The emitting source should be place in this region to optimize the source's emission enhancement. When choosing the filling fraction of this HMM, It is critical that the k_z component of the field one would like to outcouple must lie below the k_z component of the material of which the wave will eventually be outcoupled (shown as the green dashed line in Fig. 6.1b). Next, an HMM with a different metal filling fraction is chosen which has k_y components that will be outcoupled as close to the surrounding dielectric as possible. The purpose of the HMM in this region is to minimize reflection between the HMM and the surrounding dielectric, which is satisfied when the k-vectors of two regions are matched as closely as possible. Finally, the two regions of the HMM will be joined by an adiabatically tapered waveguide structure.

The tapering of this waveguide allows the large k-vectors (e.g. k_3) to smoothly and efficiently transition into smaller k-vectors (e.g. k_2) through an impedance matched region that will minimize reflection. The length of the tapered transition should be larger than the operating wavelength to avoid abrupt transitions (large reflections), while not being too long - as material losses in the constituent metal will decrease the device's internal efficiency (the length would be on the order of 1μm). The number of layers deposited in the structure should be at least 5 (of each Ge/Ag/SiO_2) so that the structure behaves as an HMM, although the number of layers can be increased if the desired size of the outcoupling end of the waveguide is required to be larger. The waveguide should be abruptly truncated at the end of the tapered region on the outcoupling side to avoid unnecessary losses. The emitter should be place on top of the HMM with optimized enhancement of the PDOS (e.g. k_3), and as close as possible to the tapered region. The enhanced emission will travel into this HMM, through the adiabatically tapered waveguide, and outcoupled into air (or other dielectric medium) with maximized outcoupling efficiency (as seen in Fig. 6.2b).

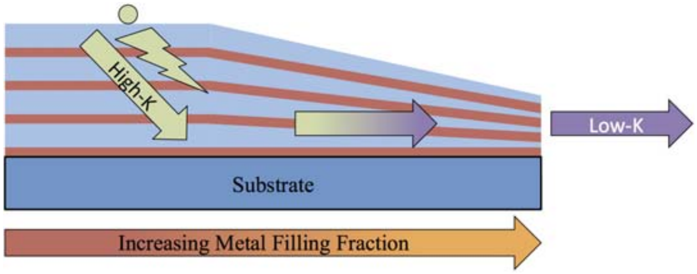

Fig. 6.2. Outcoupling of enhance emission of single-photon emitters

For the case of quenching in tapered HMM waveguides, the design should be reversed. Rather than designing the waveguide's dispersion relation to transform high-k waves into low-k waves to be outcoupled, for quenching, the high-k wave should be transformed into *very* high-k waves that cannot couple into free-space and will quickly die in the tapered region of the waveguide. In this case, as the waves move along the tapering of the waveguide, the metal filling fraction should taper down to zero. In practice, this tapering can happen in two ways: First, the metal film thicknesses can *decrease* down to zero. While in practice it is very difficult to bring the thickness of a silver film perfectly down to zero, the films can certainly be continuous below 7nm, which can correspond with a very low metallic filling fraction. The second option is to *increase* the dielectric film thickness while leaving the metal thickness the same - which also decreases the metal filling fraction. Similar to the outcoupling structure, the length of this tapered region should also be larger than the wavelength to avoid abrupt transitions in the waveguide and prevent large reflections. A schematic for the quenching tapered waveguide is shown in Fig. 6.3 where the metal film thickness tapers down to zero.

6.4 Simulations

Using a commercial Finite Element Method (FEM) software package (COMSOL Multiphysics), multilayer HMM structures with different metal filling fractions were simulated to find how well waves in HMMs outcouple to air. For both the simulated

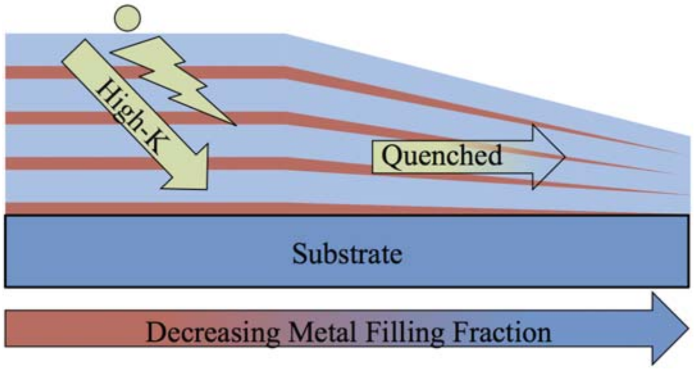

Fig. 6.3. Quenching of high-k waves passing through metamaterial with decreasing metallic filling fraction

structures shown in Figure 6.4, the scatterers (at equal distances from each end of the waveguide) are cut adjacent to the tapering. In Figure 6.4a, the modes propagating along the tapered region clearly encounter significant propagation loss as the magnitude of k increases with the decreasing metal filling fraction. Thus, device 1 is a possible solution for efficient light absorption (i.e. in-line waveguide termination). Alternatively, the design 2 simulation reported in Figure 6.4b predicts the possibility of tapering to convert the high-k HMM modes into waves with lower-k which can outcouple more efficiently into air. The power outcoupled from the tapered HMM section (right of Figure 6.4b) into air is 10% larger than the power outcoupled from the non-tapered HMM (left Figure 6.4b). Additionally, the final filling faction of design 2 can be further optimized to maximize the outcoupled power for a certain range of high-k modes. Design 1 has been tested to verify the feasibility of in-plane out-coupling, and design 2 is still under investigation to confirm the predicted improvement of the outcoupling efficiency

As expected, the outcoupling efficiencies are greater when the magnitude in k-vectors across the HMM/Air interface match more closely (see Fig. 6.1b). From the chart in Fig. 6.1, the HMM with 35% metal filling fraction clearly has the highest outcoupling efficiency and should be used to outcouple from the HMM to air. However, although the HMM with 35% metal filling fraction provides the best

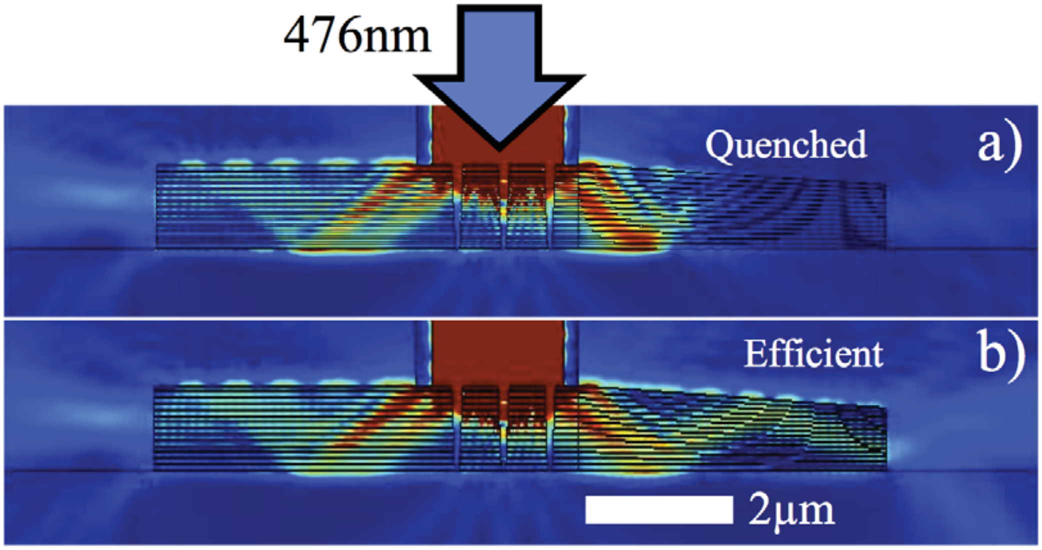

Fig. 6.4. Outcoupling efficiencies of HMMs with various metal filling fractions (a). Simulated outcoupling for one of the more high-efficient modes (b).

outcoupling, the magnitude of the k-vector in this HMM is not nearly as large as that of the HMMs with lower metal filling fractions, and will therefore have a much lower enhancement in PDOS.

6.5 Fabrication

The fabrication process for these tapered waveguide structures is explained in greater detail in Chapter 4.3, but a brief description specific to the design above is presented here. First, a ($\sim 60\mu m$) Kapton® tape mask is applied to an SiO_2 substrate before loading the sample into the chamber. Upon loading the sample into the evaporation chamber, a very thin (~1nm) germanium wetting layer is deposited followed by a 16nm silver layer at a normal angle of incidence. Next, SiO_2 is deposited normal to the substrate until the thickness is 30nm (corresponding with a 35% metal filling fraction). The substrate is then rotated 20° and the SiO_2 continues depositing until the final thickness is 48nm (corresponding with a 25% metal filling fraction). Rotating the structure during the deposition will create a shadowed region with a tapered thickness profile that transitions between the two HMM regions. The steps for depositing the three materials should be repeated until the final total number of layers is deposited. A schematic for this fabrication procedure and final fabricated structure (although with different filling fractions) can be seen in Fig. 6.5

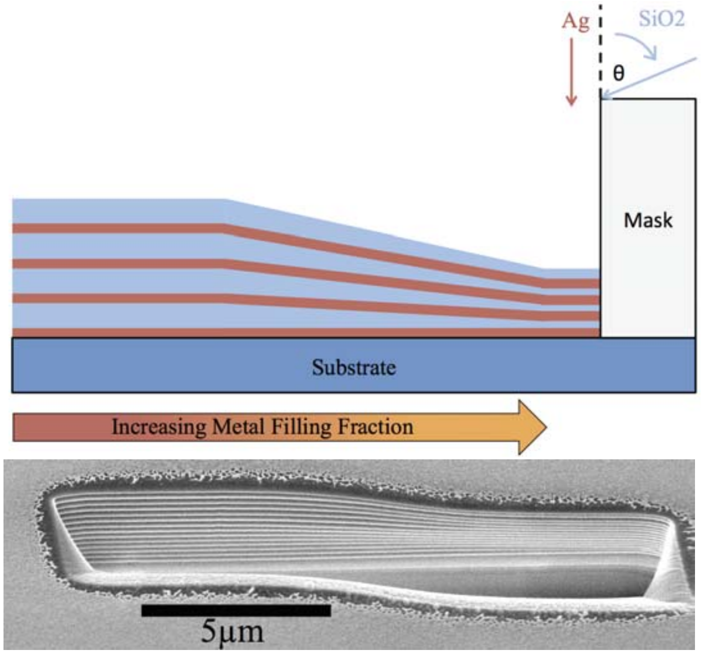

Fig. 6.5. Outcoupling of enhance emission of single-photon emitters

The fabrication method for creating the quenching tapered waveguide can also be fabricated using an angled deposition technique. First, a (1nm) germanium wetting layer should be deposited normal to the substrate. This wetting layer is crucial when tapering the silver film, because without it, the silver will not be continuous for thicknesses below 20nm, and the films will be rough and non-continuous as the metal filling fraction decreases. For creating the tapered structure where the silver film thickness tapers down to zero, the silver film can be deposited over the Kapton® tape mask - providing a shadowed region that will create a region of tapered film thickness. The thickness will taper down from 20nm in the more metallic HMM region, down to 0nm in the fully dielectric region. After each silver layer, SiO_2 will be deposited at an angle normal to the substrate to create SiO_2 films which are uniform in thickness. Because the metal film thicknesses taper down to zero, and the SiO_2 thicknesses are constant, the metal filling fraction will taper from an HMM to a pure (SiO_2) dielectric. A fabrication schematic and SEM image of the final quenching tapered HMM waveguide can be seen in Fig. 6.6.

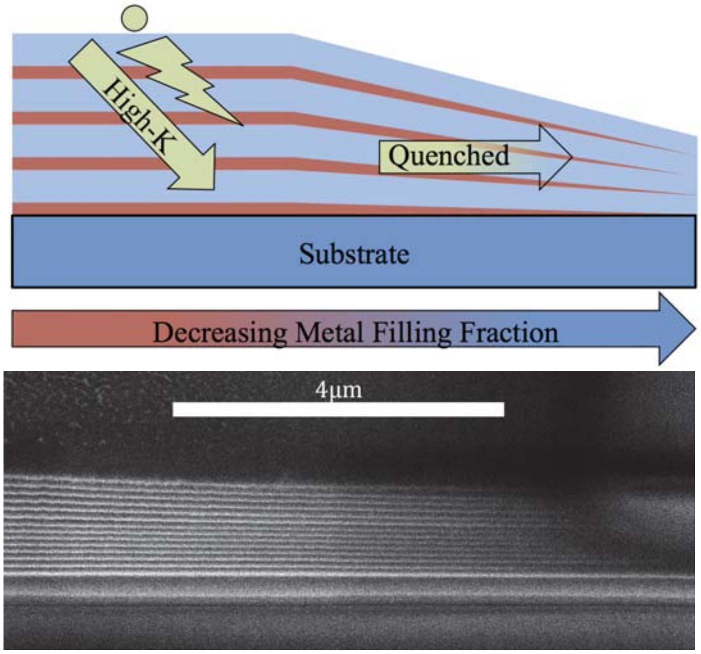

Fig. 6.6. Outcoupling of enhanced emission of single-photon emitters

6.6 Conclusions

While HMMs provide a medium with extraordinary fundamental optical properties (including extremely high PDOS), HMMs have until this point, remained elusive for use in practical devices because their extraordinary optical properties are difficult to observe in the far-field. These properties (including enhanced emission from single photon emitters, and super-resolution) are contained within high-k waves that can propagate within HMMs, but evanescently decay in dielectric media (which have bounded k's). To this point, methods for converting these high-k waves into the far-field have been impractical and inefficient. Here we propose a design for outcoupling broadband high-k waves from an HMM with relatively high efficiencies. Rather than outcoupling in the out-of-plane direction, high-k waves can be converted into low-k waves in the in-plane direction. Furthermore, the enhancement of the PDOS and the impedance matching for outcoupling can be *independently* optimized by using HMMs of different filling fractions. These HMMs can then be linked by a tapered transition region, which converts high-k waves into low-k waves (or vice versa) with impedance matching for reduced reflection. Most importantly, this technique allows for both an optimized enhancement in PDOS *and* optimized outcoupling of the high-k waves into free-space.

7. ALL-DIELECTRIC FULL-PHASE CONTROLLED METASURFACES

7.1 Introduction

Controlling and manipulating the phase of an electromagnetic (EM) wave is a fundamental technique in optics and optical devices. While there are devices which currently serve this purpose, there remains a need for optical devices that are smaller, thinner, more efficient, broadband, and in many cases, Complementary Metal Oxide Semiconductor (CMOS) compatible.

Recently, researchers have expanded the knowledge of controlling the phase of light at a planar boundary - leading to a modification of Snell's Law (one of the most fundamental laws in optics) [154]. Most of the related work in this field involves altering the phase of an incident wave at the boundary of two dielectric materials by using arrays of plasmonic (metal) antennas with different geometries, which have a plasmonic response, leading to discrete phase discontinuities. This new field has recently gained attention in the metamaterials community, and many various demonstrations have been conducted, including a focusing lens [155], extraordinary reflection/refraction [154], three-dimensional holograms [156], waveplates [157], birefringence [158] and others.

While these various devices have been shown to function, they rely on plasmonic surface structures, which suffer from high losses, and very low efficiencies (currently 10% or below in transmission mode [157]), especially at optical and infra-red frequencies. Additionally, these metasurfaces only work for specific input polarization, and very specific antenna design to achieve the required phase distribution.

To this end, the phase (or wavefront) and polarization of incident light can be modulated by using metasurfaces - specifically designed, subwavelength metamaterial structures on a substrate's surface. Metasurfaces are designed to abruptly and precisely shift the phase, amplitude or polarization of incoming light. Metasurfaces are able to fully control the phase within a thin layer (less than the free-space wavelength) after transmitted through, or reflected by the metasurface. These optically thin metasurfaces are desired over 3-Dimensional (3-D) optical materials, due to their relatively simplistic fabrication, and reduced thickness. Existing metasurfaces rely on plasmonic (metal) structures to achieve the desired phase shift. These structures depend on a plasmonic resonance, making them inherently lossy and narrowband. In contrast to plasmonic metasurfaces, dielectric metasurfaces completely eliminate losses within the metasurface, greatly improve efficiencies, and operate broadband, all while remaining very thin - less than one free-space wavelength. Furthermore, these binary structures can all be fabricated simultaneously with a single lithography and etching process.

7.2 Detailed Description

In contrast to existing metasurfaces, all-dielectric, subwavelength, lossless, metasurfaces with full (2π radians) phase control, and much higher efficiency have been developed. These surfaces are also very thin (less than the wavelength of light in free-space). Additionally, because this technology is not reliant on any resonant effects (such as plasmonic or phononic), the phase modulation is broadband. In this chapter, dielectric is defined as a material with positive real-part of permittivity (ϵ') at the operation wavelength that does not exhibit a metallic (plasmonic) response, and this definition *does* include semiconductors such as silicon. Similar to plasmonic metasurfaces, dielectric metasurfaces can still be very thin - smaller than the free-space wavelength.

When a plane wave is incident on the boundary of two dielectric materials with a "step"-like geometry as shown in Fig 7.1, the phase of the wave will shift by a phase given in Eq. (7.1) [159]

$$\Delta\phi = \frac{height \times 2\pi\Delta n}{\lambda_0} \tag{7.1}$$

where λ_0 is the wavelength of incident light in free space, $\Delta n = n_{high} - n_{low}$ where n_{high} is the material with high index, and n_{low} is the surrounding medium with low index. In order to achieve full phase control ($\Delta\phi = 2\pi$), the height (or depth) of these various structures should be at least (7.2)

$$height = \frac{\lambda_0}{\Delta n}. \tag{7.2}$$

For example, if the substrate is Silicon ($n_{silicon} = 3.48$) surrounded by air ($n_{air} = 1.00$), the metasurface thickness should be at least 626nm for 1.55μm incident light.

In other words, having an abrupt step in height of one material can bring an abrupt change in phase $\Delta\phi$ of 2π. However, what is desirable for most applications is the ability to have *full* control over phase modulation (*any* angle *between* 0 and 2π) at any location on the metasurface, as shown in fig 7.1

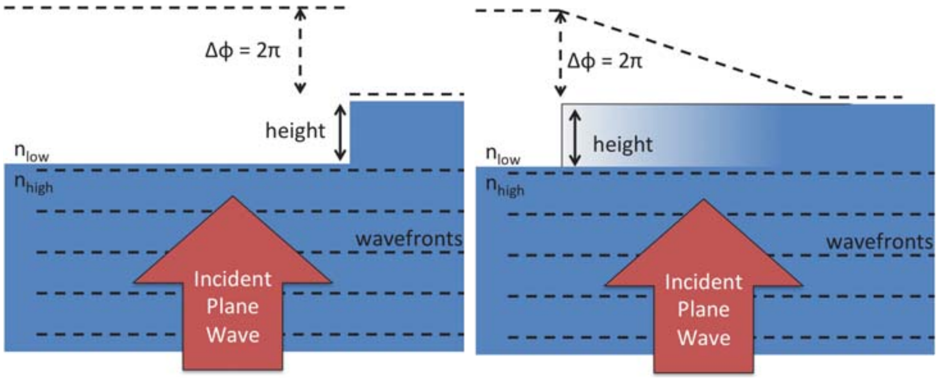

Fig. 7.1. The figure on the left shows an abrupt change in height, resulting in a 2π phase shift. The figure on the right shows a gradient transition from n_{low} to n_{high}, providing any phase between 0 and 2π

In order to achieve this, a family of discrete, dielectric metamaterial structures that exhibit an abrupt change in phase of any angle between 0 and 2π has been developed. These structures are broken down into two groups: posts and holes, with all structures having approximately the same height (or etching depth). In various aspects, when the minimum height from Eq. (7.2) is achieved, control over the full $\Delta\phi = 2\pi$ phase control is possible, leading to a large number of new applications.

The period of these dielectric elements should be less than or equal to approximately(7.3)

$$period \leq \frac{\lambda_0}{n_{high}} \tag{7.3}$$

to behave as an effective metamaterial and avoid higher-order modes, and therefore scattering.

Here, posts refer to solid high-index dielectric elements surrounded by low-index medium, and holes are a high-index medium filled with "holes" of the low-index medium. As the size of the posts increases (or size of holes decreases), the filling fraction of high-index material increases, increasing the phase delay caused by the metasurface. Additionally, structures that are *entirely* high-index or low-index materials (neither holes nor posts) can be used. The size of posts and holes can be precisely modulated, allowing almost any sized hole or post to be fabricated (only limited by fabrication methods and periodicity from Eq. (7.3)). Using this precision, structures with a smooth gradient in size can be created.

The geometry and filling fraction of each structure changes the phase differently, producing a smooth gradient and large distribution in phase for variously sized posts and holes with vertical sidewalls. Figure 7.3 demonstrates one example - using silicon and air as high- and low-index materials (respectively), equation (7.2) defines the minimum height for full-phase modulation to be 626nm when the incident wavelength (λ_0) is 1.55 μm. Using a slightly larger height of 650nm, simulations show that a phase difference ($\Delta\phi$) of more than 2π can be achieved. The various structures have been modeled and their reflections have been calculated to be between 0.4% and 30%.

One significant difference between these dielectric metamaterial structures, compared to their plasmonic counterparts [154] is the drastic improvement in efficiency.

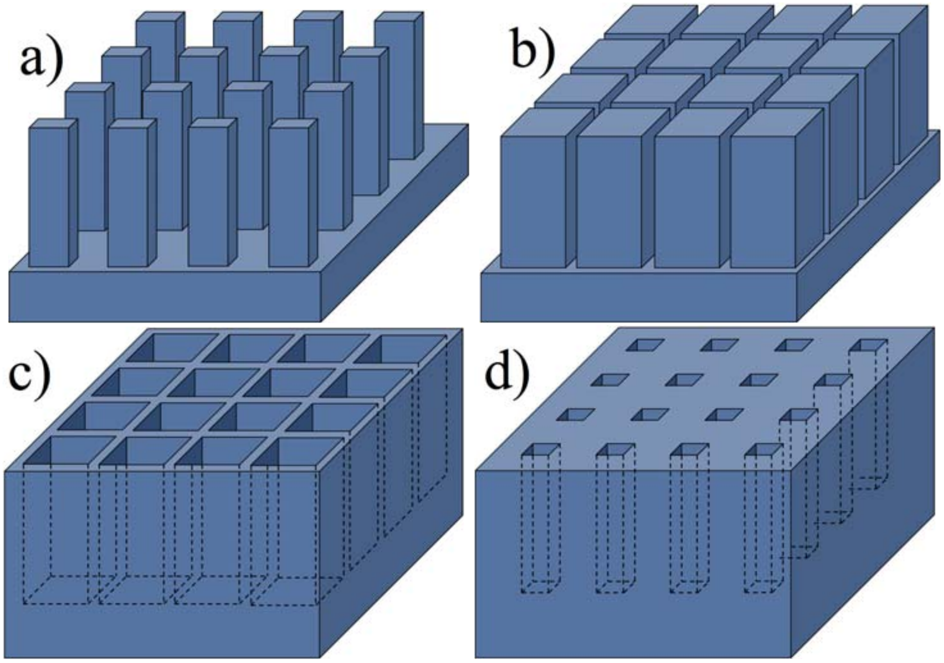

Fig. 7.2. Periodic arrays of 4 different dielectric metasurface element types (a) Large Posts, (b) Small Posts, (c) Large Holes, (d) Small Holes. Each element type has a corresponding phase accumulation associated with it. In general, the phase shift corresponds with the filling fraction of high-index to low index materials in the structures. Generally, (a) - (d) corresponds with the phase accumulation from least to greatest. In addition to these 4 structures, purely low-index, or purely high-index elements can be implemented - corresponding with smallest and largest phase displacement (respectively).

Because these structures do not require a metal (plasmonic) response, they are neither subject to the inherent losses in metals, nor do they depend on any resonance - making them broadband. In fact, these dielectric structures have virtually no losses. The metasurface can be designed to be either dependent or independent of polarization. Furthermore, these structures can have a reduced impedance mismatch between planar high-index to low-index interfaces, which can lower reflections and increase throughputs if desired. Even lower reflections can be achieved by creating structures with non-vertical tapered sidewalls, further reducing the impedance mismatch.

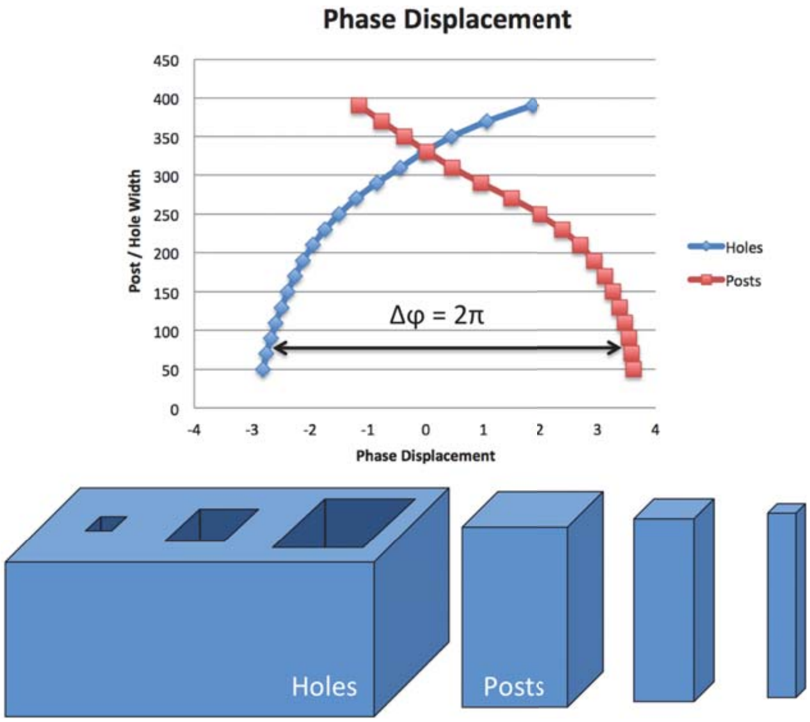

Fig. 7.3. Phase displacement corresponding with various post / hole structures. Posts and holes on the bottom are schematic sketches of holes and posts of different sizes

7.3 Anomalous Refraction with Dielectric Metasurfaces

Applications for these dielectric metasurfaces include *any* optical element that utilizes 2π (or close to 2π) phase modulation. Just a few applications this technology is applicable towards include wave-plates, aberration free lenses, spatial light modulators, photonic computing devices, polarization dependent & independent extraordinary reflection & refraction, improved Total-Internal Reflection (TIR) coupler/decoupler, optical vortexes, wavefront shaping, beam shaping, 3-D full-wave Holograms, integrated optics, tunable, adaptive & tunable optics, birefringence, display technologies, energy harvesting, photovoltaics, and many others. The remaining part of this chapter is devoted to extraordinary reflection and refraction (as seen in Fig. 7.4)

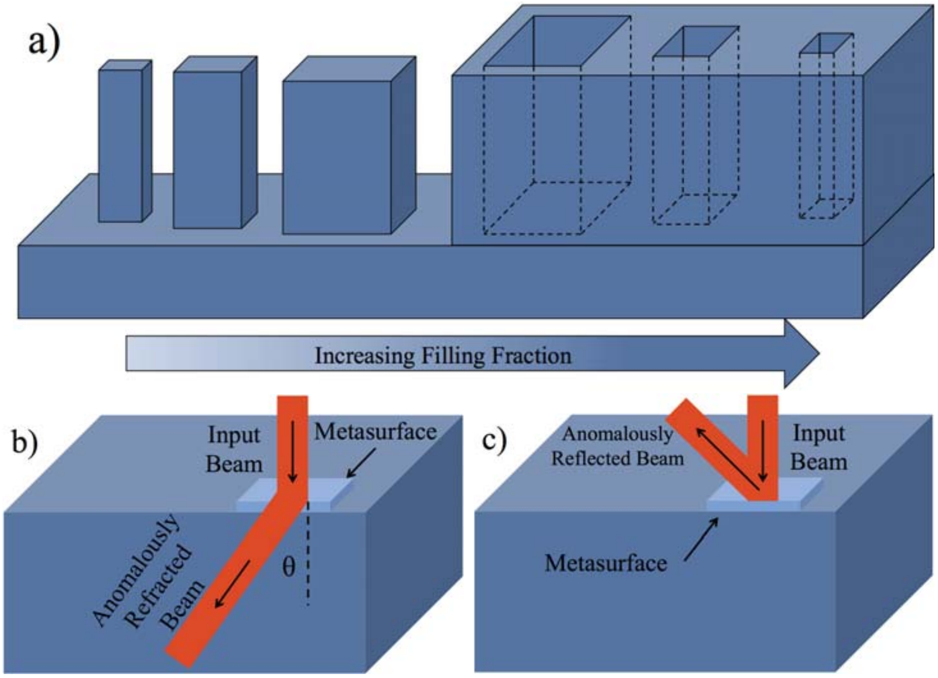

Fig. 7.4. Extraordinary refraction arising from the distribution in phase accumulation along the dielectric metasurface. The top figure shows one unit cell of the extraordinary reflection / refraction array. The bottom figure shows a beam entering a metasurface and undergoing extraordinary reflection or refraction. A similar approach can be taken for reflecting light at extraordinary angles.

One example of using dielectric metasurfaces to modulate the phase and direct the direction of incoming light is a blazed grating structure. Operating at 1.55μm, such silicon post and hole structures can refract incoming light anomalously.

As previously discussed, a series of binary post/hole structures can be used to linearly alter the phase of the transmitted light by increments of 2π by altering the structures filling fraction of high-index and low-index materials

The array of post structures were fabricated in the following manner (schematic in Fig. 8.3). First, a 500μm × 500μm array of square and square-with-hole structures were patterned into AEP resist on a double-side-polished (DSP) wafer. These patterned structures are for the mask for the host and hole structures. Next, a 45nm layer of Al was deposited in a standard deposition and lift-off procedure. This Al Layer was used as the mask for later etching. Etching was performed on these structures using the Panasonic Reactive Ion Etcher (RIE) with SF_6 gas. In total, 4 consecutive etches were performed on the structure. In between each etch, the sample was examined in the SEM, and the bias power in following etching recipes was adjusted to maintain vertical walls through the etching process. After the final etching depth was achieved (∼600nm), the remaining Al mask was removed with "NanoStrip" (Piranha) and the final structures can be seen in Fig 7.6

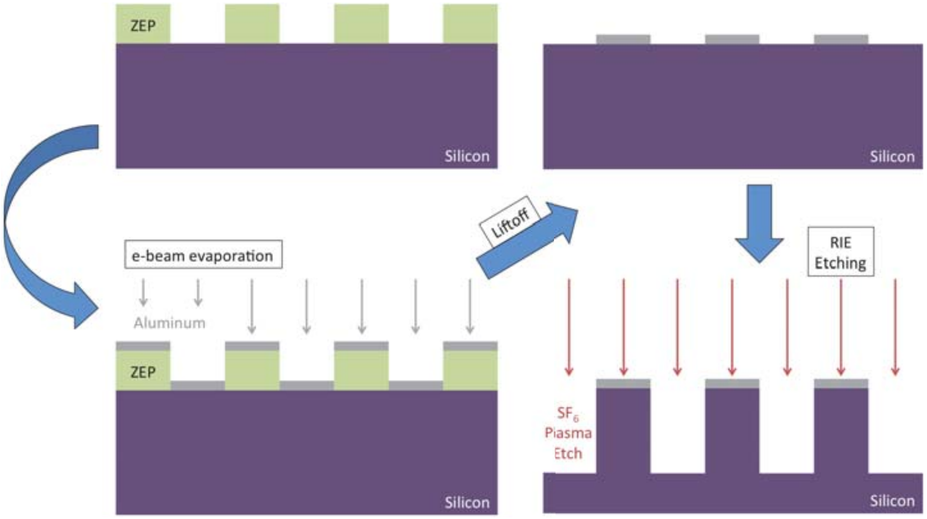

Fig. 7.5. Schematic showing the major steps of the fabrication process.

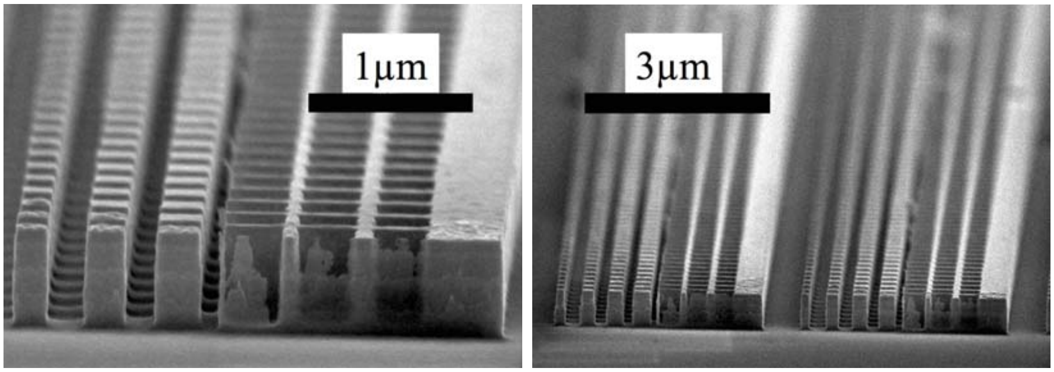

Fig. 7.6. Sideview of the post and hole structures fabricated for anomalous refraction.

Here, we see that indeed the binary dielectric metasurface layer does refract light at anomalous angles very efficiently. While only 6.2% of light travels straight through the sample, as predicted by traditional Snell's law, 46.8% refracts at an anomalous angle (calculated), and 33.88% exits the sample at an anomalous angle of 23° (measured).

Angular measurements of the sample were taken using the spectroscopic ellipsometer. Focusing probes were used to focus the incident light down to a 500μm diameter. The sample was illuminated normal to the substrate on the etched side of the sample. Transmission measurements were taken by sweeping the detector between -5 and 30° from the substrate normal. Measurements at 1.55μm were taken with both p-polarization (along the surface gradient) and s-polarization (perpendicular to the surface gradient). The results are shown below in Figure 7.7. While the structure was designed to operate at 1.55μm, the optical transmission was measured in a broadband range from 1μm to 2.3μm. As expected, the silicon absorbs light with wavelength below $\sim 1.2\mu$m, and anomalously refracts light at a very broad range of wavelengths at a range of angles very efficiently, as can be seen in Fig. 7.8.

Upon this first demonstration of refracting light at anomalous angles, these same principles are applied in the Chapter 8 "All-Dielectric Metasurface Focusing Lens" for creating a dielectric metasurface focusing lens.

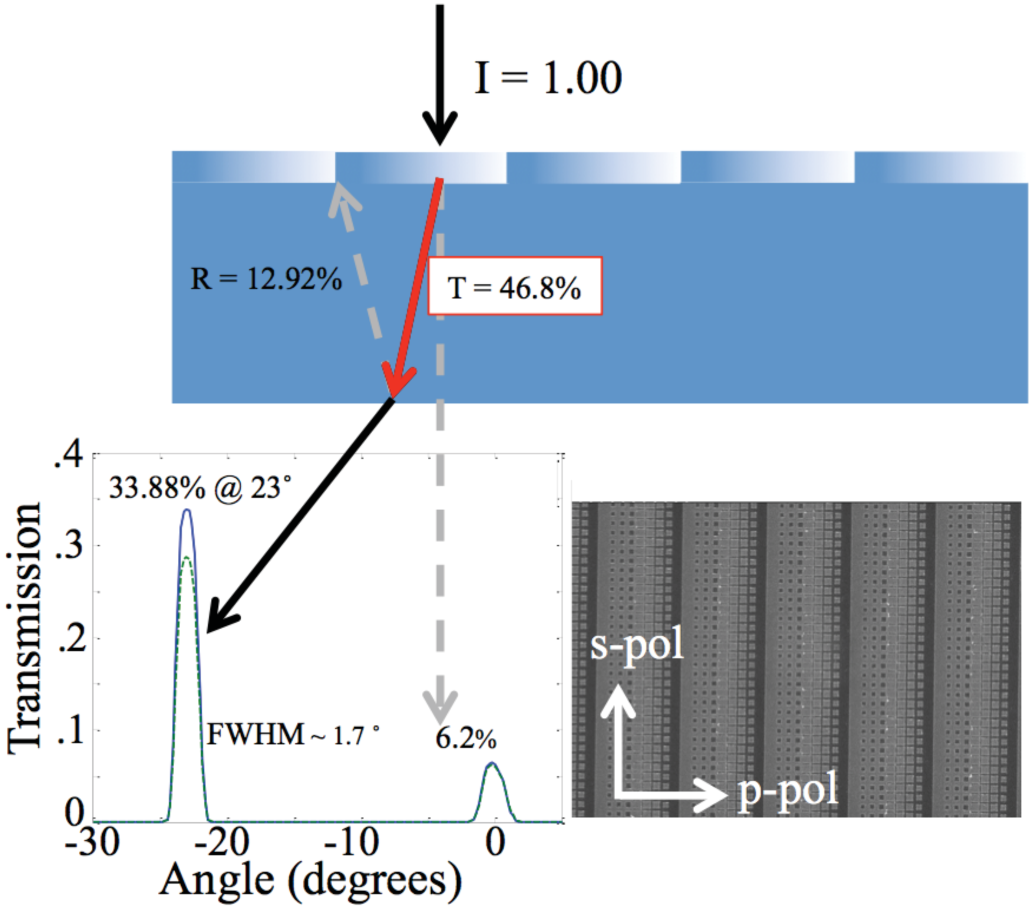

Fig. 7.7. Angular transmission measurements at $\lambda = 1.55\mu$m.

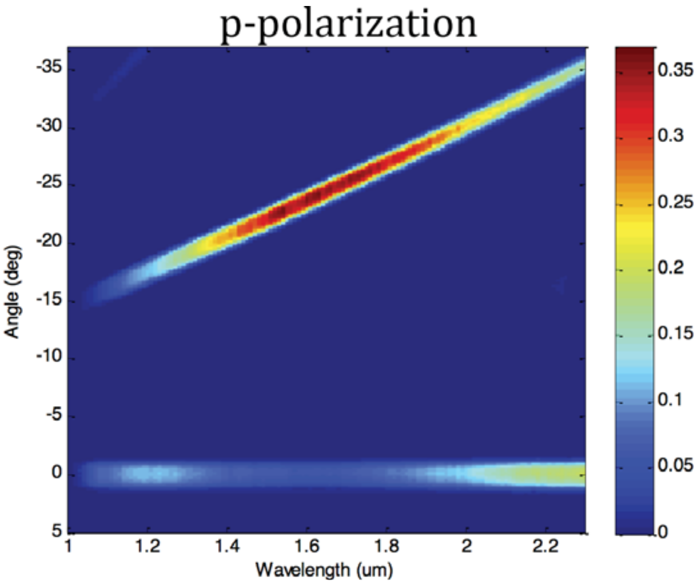

Fig. 7.8. Spectroscopic angular scan of the transmission through the silicon metasurface for p-polarization (Results are almost identical for s-polarization).

8. ALL-DIELECTRIC METASURFACE FOCUSING LENS

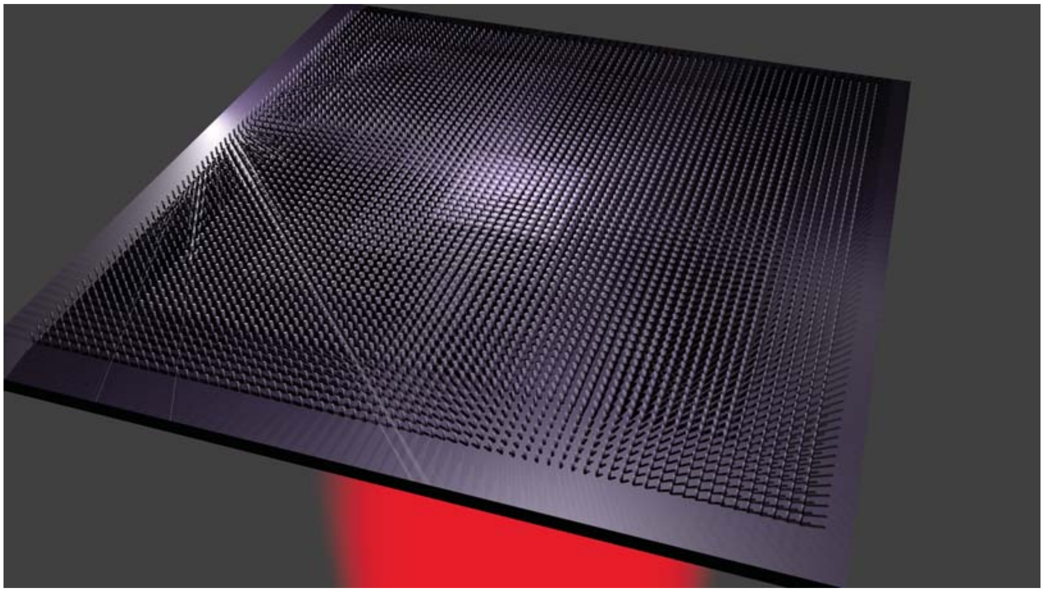

We have proposed, designed, manufactured and tested low loss dielectric microlenses for infrared (IR) radiation based on a dielectric metamaterial layer. This metamaterial layer was created by patterning a dielectric surface and etching to sub-micron depths. For a proof-of-concept lens demonstration, we have chosen a fine patterned array of nano-pillars with variable diameters. Gradient index (GRIN) properties were achieved by engineering the nano-pattern characteristics across the lens, so that the effective optical density of the dielectric metamaterial layer peaks around the lens center, and gradually drops at the lens periphery. A set of lens designs with reduced reflection and tailorable phase gradients have been developed and tested - demonstrating focal distances of a few hundred microns, beam area contraction ratio up to three, and insertion losses as low as 11%.

8.1 Introduction

Flat and compact micro-lens arrays can be used for many applications including imaging systems, displays, and detectors. In contrast to conventional curved lenses and lens arrays, dielectric metasurface lenses can be readily wafer-level integrated and manufactured using processes compatible with CMOS technology. These lenses can be designed to improve the effective array filling factor by being tightly mapped on a surface. Size, weight, and other packaging characteristics for optical sensors, as well as assembly cost, can be improved significantly. Making binary surface GRIN lenses as a metamaterial layer can be more efficient, compared with conventional methods of micro-lens manufacturing (such as surface profiled Fresnel lenses, geometric micro-machined lenses, or an assembly of separate discrete micro-lenses into arrays).

Planar binary surfaces with sub-wavelength patterns have been used for reducing the reflection [160] from high index materials, as well as modulating the phase [161] of the transmitted wave. While this phase modulation can be accomplished using plasmonic surfaces, dielectric metasurfaces have the huge advantage of reducing or even eliminating insertion losses. Strong intrinsic absorption within an operational spectral band located in the vicinity of the plasmonic resonances results in very low transmission through plasmonic metasurfaces, at a level of a few percent at best. This makes the plasmonic approach impractical for transmission optics applications. Conversely, the sub-wavelength structures of metasurfaces are virtually dissipation free (even near polaritonic resonances), if a transparent dielectric is used as the lens material. Lack of material dissipation and reduced reflectivity avoids the problem of insertion loss for these meta-lenses.

Similar dielectric diffractive structures have been used for designing physically thin versions of various optical components, including blazed gratings [162–165], waveguide couplers [166–168], and computer generated holograms [169,170]. Flat lenses based on diffractive structures have also been proposed [165,171,172] and demonstrated [171]. For example, a TiO_2 blazed grating lens has been developed for a wavelength of 860 nm, with a demonstrated focal length of 400 μm [164, 173]. Other similar lenses were proposed for on-axis and off-axis imaging [161, 164, 174]. A similar lens operating in the visible range (650nm) has been proposed using silicon pillars on an oxide substrate. Although silicon is absorbing in the visible and NIR range, losses in the proposed lens are on the order of 20% at an operational wavelength of 650nm when using a transparent substrate, due to the small volume fraction of Si in the structure [175]. Hence, the phase mask depth variation $\Delta\phi \approx 2\pi\delta n h/\lambda_0 \sim 2\delta n \cdot rad < 2\pi$

8.2 Approach

We have developed a simple design for a thin dielectric meta-surface lens that can be easily manufactured with relaxed tolerance, compared to precision diffractive structures. The objective was to create a sub-wavelength, fine-patterned meta-surface as a phase mask with a smooth radial dependence of phase increment on transmission, avoiding 2π phase steps. Quasi-parabolic radial gradients of phase along the surface were created by slow variation of geometric parameters of the fine pattern. The meta-surface thickness is approximately one-third of the free-space wavelength ($\lambda = 1.55\mu$m, and height $\approx 0.5\mu$m), in our specific case. Hence, the phase mask depth variation, $\Delta\phi \approx 2\pi\delta n(h/\lambda_0) \sim 2 \cdot \delta n \cdot rad < 2\pi$ across the lens area is relatively small. Therefore, the mask covers just one single central Fresnel zone of the transmitted beam, rather than multiple Fresnel zone rings with 2 phase steps as are typical in a diffractive lens structure. As our experiments show, a mask of this type can be sufficient to reduce a laser spot diameter by a factor of about three, which can be very useful for many laser receiver applications.

For a proof-of-concept demonstration, we selected a nano-patterned regular array of pillars etched with near vertical walls over the silicon wafer surface. The periodicity of pillar positions has been chosen to be constant over the entire lens, while the pillar diameter gradually varies from the lens center to its periphery to create spatial variations in effective refractive index of the meta-layer. To obtain a phase mask with only 0th order diffraction that minimizes scattering loss into other diffraction orders of the periodic structure, the periodicity of the pillar structures must be less than the structure cutoff scale, λ_0/n, where λ_0 is the wavelength in free space, and n is the refractive index of the substrate. For the case of 1.55μm incident light with a silicon substrate, the pillar periodicity should be less than about 445nm (here, 440nm was chosen). The pillars were arranged into a square symmetry lattice in the x- and y- (in-plane) directions to guarantee polarization isotropy and the same optical characteristics under both x- and y-polarization. As a first approximation, we assume that all pillars will have approximately the same height (given by the etching depth) due to the simultaneous etching of all structures.

Before fabrication, a commercial software package utilizing Finite Element Method (FEM) was used to simulate the optical properties of various structures. A parametric three-dimensional model of periodical pillar structures was simulated, and phase increments of transmission and reflection were calculated. Parametric sweeps were run over the pillar height, diameter, and wall slope to find structures exhibiting both low reflection and large phase increments. Due to practical fabrication reasons, all of the pillar heights and wall slopes were maintained constant across the entire structure in simulations, while the pillars diameter were varied across the surface providing the required phase distribution.

The phase of a wavefront incident on a conventional lens is modulated by the lens curved profile resulting in lateral variations of the optical path due to glass thickness variations across the lens. Similarly, a dielectric meta-lens alters the optical path length (phase) of the transmitted light. The lens thickness is constant, and it is the effective index of the layer that varies, as takes place for conventional gradient index (GRIN) lenses. Using pillars of different diameters while maintaining the same periodicity, the volumetric fill factor of the substrate material (vs. air) can be tailored across the metalayer surface. Extended dynamic range of the phase variations in the transmitted light requires a large variation in the effective refractive index of the sub-wavelength thin modified layer. The dielectric metamaterial forming the desired meta-layer provides this capability. A plane wave incident on this lens will exit the surface with the curved phase profile characteristic of a positive focusing lens are shown in Fig. 8.1

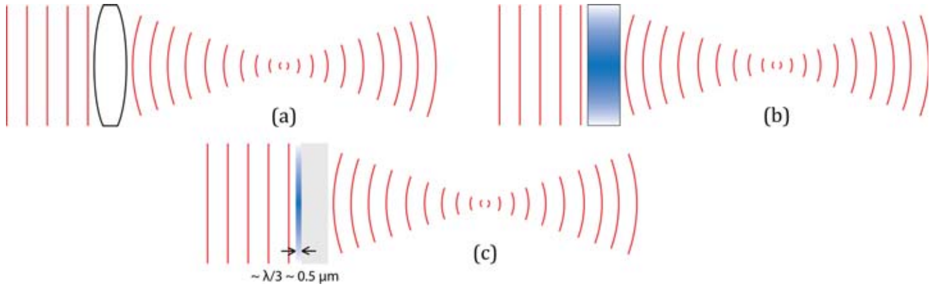

Fig. 8.1. Plane wave-fronts (shown in red) travelling through a conventional thick, curved lens (a), compared to a thick gradient index (GRIN) lens (b), and to a thin, flat meta-surface lens (c).

8.3 Design

Pillars with a small diameter will result in a low fill factor, mostly dominated by the air between the pillars; and the effective index will approach that of air, index $n = 1.0$. Such areas of the pattern will accumulate a small leading phase, and are placed at the periphery of the lens. Thicker pillars with larger diameters result in a higher volumetric fill factor with a higher attendant effective index; and these will accumulate a large lagging phase, slowing the wave-front of the incident field.

Our models show that the effective index of actual meta-layer-induced deviates from the simple direct proportionality to volumetric filling factor. As an example, interactions of transmitted light with localized polaritons in the nano-structures results in pushing more light into volumes occupied by the high index substrate dielectric. In general, dielectric meta-layers can be designed to provide sharper spatial phase gradients than ones anticipated from simplified fill-factor effective medium model. Fabri-Perrot type of spectral resonances created by incident light multi-bouncing between two interfaces bordering the meta-layer one at the air side, another at the substrate side should also be accounted for. In particular, transmission and reflection characteristics of the metalayer become dependent on wavelength and on angle of incidence.

The lenses examined in this paper are each 30μm × 30μm in size, and square-shaped. The nano-pattern for every lens consists of five concentric “belts. The belts are formed by a discrete collection of square tiles, each 3μm x 3μm in size. The pillars diameter is constant over the whole surface for every tile, see Fig. 8.2. Thus, the belts were formed by pillars with constant diameter. We explored two designs square and rounded lenses, both shown on the images in Fig. 8.2. The diameter of the pillars changes from belt to belt (see Fig. 8.4), and belts are arranged with thick pillars near the lens center and thin pillars towards the periphery.

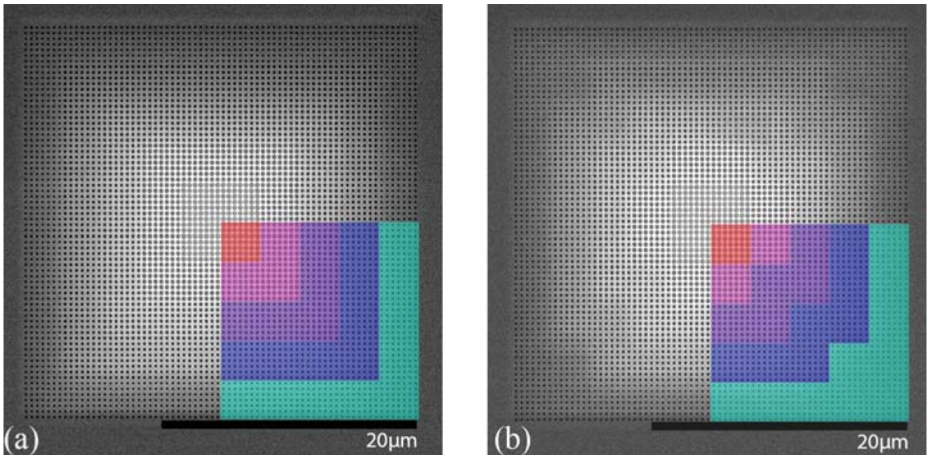

Fig. 8.2. Top-view of the two realizations of the lens designs: a square lens (left), and the rounded lens (right), with notched belt corners. The colored region shows the arrangement of the belts for each lens.

8.4 Fabrication Method

The pillar structures were fabricated by first patterning the circular discs used as a mask for dry etching, (Fig. 8.3). The lithography was done using a Leica VB6 electron beam writer on a double-side-polished silicon substrate with ZEP resist.

Upon lithography and development, a 45nm thick aluminum mask was deposited, preceded by a 2nm titanium adhesion layer via electron beam evaporation. The ZEP resist was removed via lift-off, leaving the aluminum mask on the substrate - used for etching. The etching was performed over the entire substrate, leaving behind only the small areas protected by the aluminum mask. Upon plasma etching, these aluminum circular discs leave behind cylindrical silicon pillars rising up from the flat, etched substrate. Three alternating steps of Reactive Ion Etching (RIE) and Scanning Electron Microscopy (SEM) were performed. In each step, the etching recipe was altered to ensure vertically etched sidewalls, and precise etching depths. After reaching a depth of 550nm, the aluminum mask was removed using Nanostrip, leaving behind the array of vertical silicon pillars of different diameters.

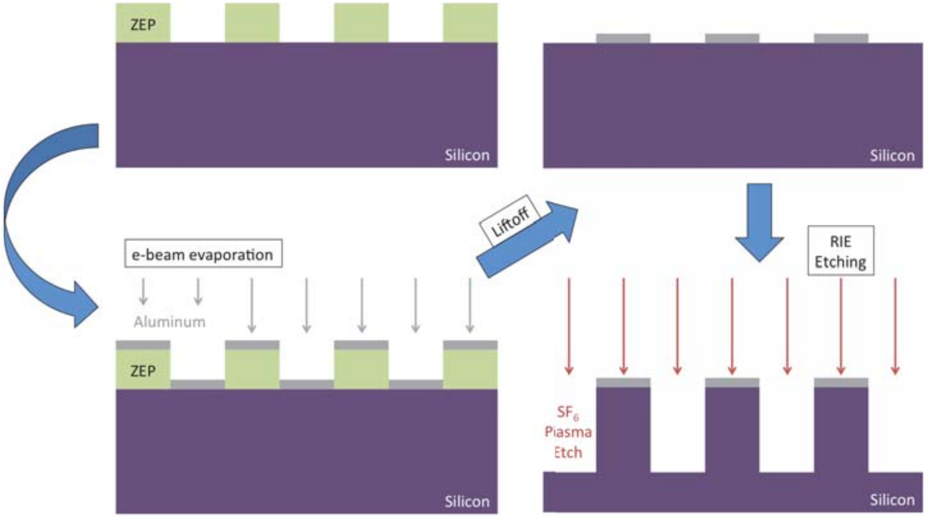

Fig. 8.3. Schematic showing the major steps of the fabrication process.

In total, three different combinations of five nano-patterns for every lens were selected to provide gradual variation of transmitted phase increments using preliminary modeling predictions. Altogether, 15 different nano-patterns for tiles were used to design all the lenses. SEM photos for two of the 15 of nano-patterns are shown in Fig. 8.4. For every combination of the belt patterns, both square and rounded lens tile geometries (see Fig. 8.2) were applied to design 30μm x 30μm lenses. Moreover, to reduce the risk of manufacturing accuracy, every lens design was implemented in three versions: one was patterned with an optimal pillar diameter, while another two had small deviations from the optimum, both larger and smaller values. So, in total, 18 different lens realizations were patterned and fabricated on the same wafer.

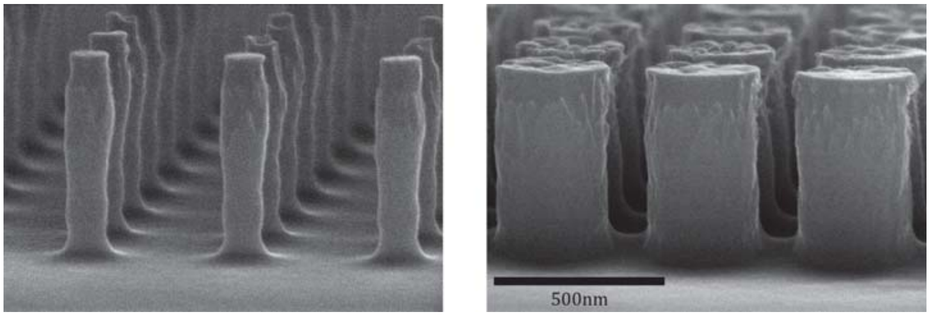

Fig. 8.4. Side-view of the pillar structures that modulate the phase of light passing through the lens. Pillars of large and small diameter etched to similar depths.

Along with the lenses, 15 (120μm x 120μm) arrays of pillars were fabricated simultaneously on the same wafer. These 15 arrays were patterned uniformly, each containing pillars with the same diameter over the entire area. These replicate the nano-patterns for all 15 elementary tiles we used for the lens designs. The additional arrays allowed independent measurements of transmission through such patterns, which were required to validate the model.

8.5 Phase Increment Measurement

Upon fabrication, SEM images of the 15 large (120μm x 120μm) arrays were monitored to measure the final dimensions of the pillars in each array. These parameters were fed into the original 3D FEM model, simulating predictions for the reflection and phase of the field passing through each uniformly patterned tile. To experimentally validate our model, the phase acquired upon crossing the pillar arrays was experimentally measured using the shearing interferometer technique setup shown in Fig. 8.5. The incident beam spot straddled the interface between the patterned region and the bare silicon surface, so that each half of the beam experienced different phase shifts crossing the wafer. The position of the interference fringes (formed by interfering these two parts of the illuminating laser beam) were compared to fringe positions when the sample was laterally shifted so that both parts of the beam crossed the un-patterned area of the wafer. As a result, a phase increment accumulated upon passing through each pillar array was compared to the increment accumulated upon passing through the surrounding flat substrate of the same thickness.

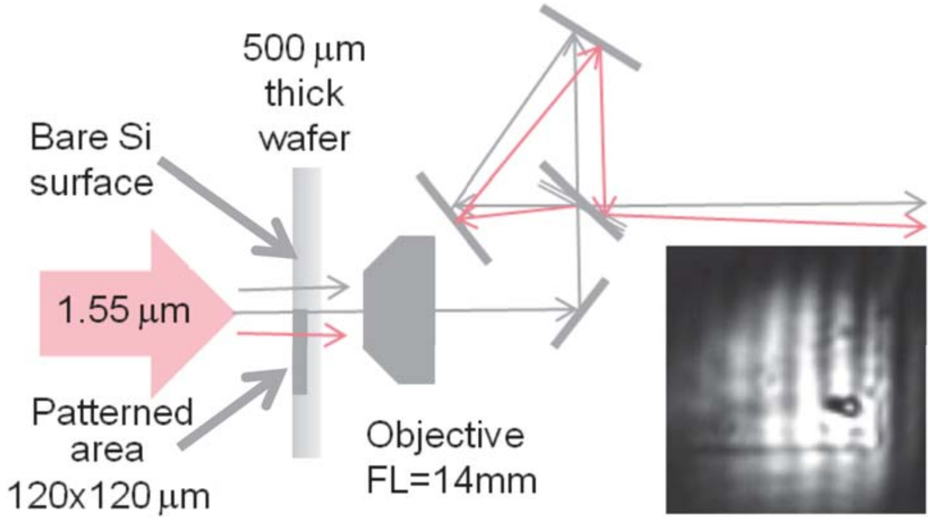

Fig. 8.5. Experimental setup for optical phase measurements. The phase of each uniform array was measured by detecting the lateral shift in the interference pattern created between the beam passing through the patterned surface and the bare silicon surface.

The experimentally measured phase shift of each uniform array is shown and compared to the computer simulations in Fig. 8.6. We clearly see a close correspondence between the simulated and measured phase, and the simulations are well within the margin of experimental error.

The arrays in the set we tested were enumerated using the following convention. Of these 15 structures, arrays 1-5 were used to form the 5 sequential concentric belts, starting from the lens center. Patterns 1-5 were used for lens design #1. Arrays 6-10, similarly, refer to the concentric belts of lens design #2. Finally, the arrays 11-15 form

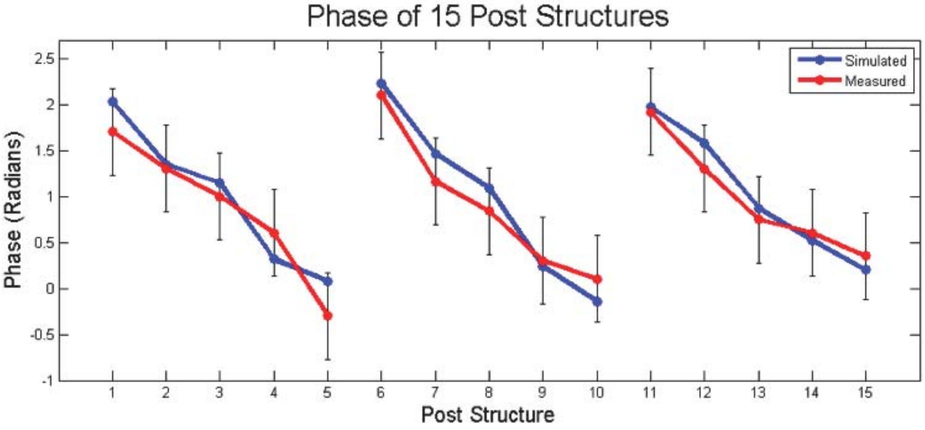

Fig. 8.6. Simulation (blue) and experimental measurements (red) for phase increments added by patterned meta-surfaces for the 15 pillar structures. The black error bars represent the 15% margin of error in the experimental measurements.

the concentric rings of the lens #3 design. Collectively, the gradual phase variations from belt to belt of the lens will shape the wavefront, producing the focusing behavior of the lens (as sketched in Fig. 8.1).

8.6 Focusing Effect

Focusing properties of the meta-lenses were experimentally studied in a separate set of experiments. The surface of the silicon wafer lens was illuminated from the patterned side with a collimated 1.55μm laser beam, shown in Fig. 8.7. The goal for this experiment was to monitor the spatial structure of the beam spot after the light had been transmitted through the lens. Different beam cross sections were imaged behind the lens with a high magnification onto an InGaAs camera (with a magnification factor of about 1:30). The evolution of the diffraction pattern (which is induced by the nano-patterned phase mask) was captured by displacing the position of the imaging plane along the z-direction. A large diameter uniform beam (that overfilled the lens), or a Gaussian beam approximately matching the size of the lenses were used. The small diameter Gaussian beam was deliberately tilted at a small angle (about 10°), with respect to the normal. This tilt helped avoid interference of the transmitted light with secondary reflections from the 0.5mm thick silicon wafer surfaces that could potentially interfere with the primary images. A microscope objective placed directly behind the silicon wafer collected light and used for imaging. The position of the imaged cross-sections was varied in small increments by displacing the microscope objective position, or by moving the camera along the z-direction.

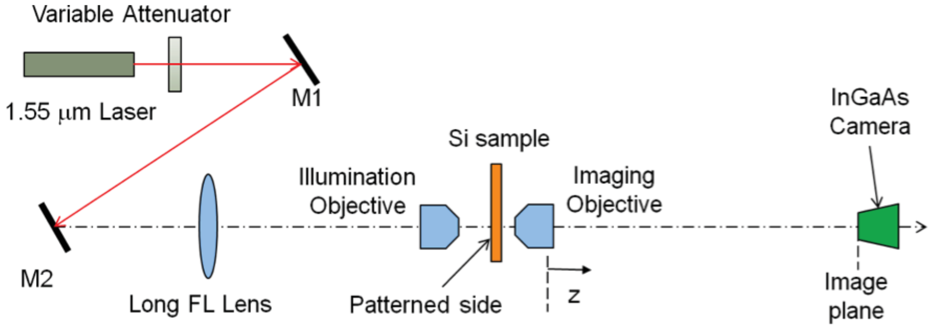

Fig. 8.7. Schematic of the focusing effect demonstration. The single mode radiation from an Er fiber laser was tightly focused on the Si sample surface to monitor beam diffraction behind the surface micro-lens using a simple imaging system.

Fig. 8.8 illustrates the dynamics of the focal spot evolution along the z-axis behind one of the micro-lenses. Here, the wafer was illuminated by a large beam at normal incidence. The spatial fluctuations seen in the background of the figure are artifacts typical in coherent imaging. Imaging the wafer surface plane where the lens is located ($z = 0$) provides a reasonably flat intensity profile. At a distance of about 160μm behind the micro-lens (inside the wafer), the light is focused to a round spot of highest concentration. This spot is much smaller than the 30μm x 30μm size of the micro-lens (which is depicted as a yellow box in Fig. 8.8). The positions of the image plane have been calculated to account for refraction of the imaging light at the output Si/air interface. When shifting the image plane further into the wafer bulk, the spot size increases. The beam spreading continues more rapidly when light escapes from the Si wafer into air.

Fig. 8.9 shows the intensity distribution at different imaging planes for the case when a 24μm diameter tilted Gaussian beam illuminated the square micro-lens (left photo in Fig. 8.2). Right at the micro-lens location (i.e. at input interface of the wafer) plane, the original Gaussian profile is seen. The plane of minimal spot size (which we call the focusing plane) is shown in the middle, along with the plane one focal length behind the focusing plane, shown on the right. The plot in Fig. 8.9 compares the original Gaussian intensity profile with the profile at the focal spot. It can be seen that the lens reduces the beam spot size by nearly a factor of three - the FWHM of the incident light is decreased from 32μm to 11μm. The on-axis intensity increases by a factor of 1.87 in this case (compared to input beam intensity).

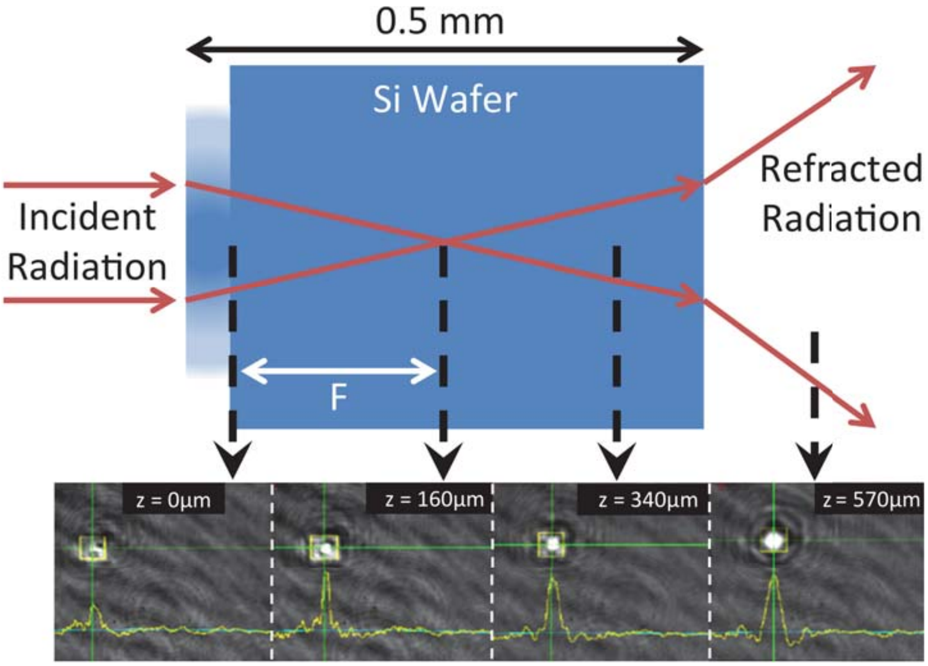

Fig. 8.8. Intensity profiles taken at different image planes behind the micro-lens surface measured from the input surface of the wafer. The micro-lens is strong enough to focus light inside the wafer. The yellow-color frame depicts a 30μm x 30μm box equivalent to the size of the micro-lens.

The photos in Fig. 8.9 demonstrate that along with the tightly focused spots, a halo pattern around the spots is present near the focus. The light power distributed

Table 8.1
Lens Characteristics

	Bare Si Wafer	Circular Design	Square Design
Front Surface Reflectivity	30%	11%	14%
Portion of Input Power in $15\mu m \times 15\mu m$ spot	17.5%	35%	35%
Distance (μm) to the position with maximal concentration in $15\mu m \times 15\mu m$ spot	N/A	450	510
Focal distance defined by a minimal spot size	N/A	122	221

over the halo around the spots explains why the peak intensity increase at the focal spot center is less than would be expected from just beam area reduction. The halo carries imprints of the square symmetry of the lens design, which indicates that the halo is an aberration effect associated with the discrete tiled square lens design. Another plausible explanation is insufficient amplitude of the phase mask for this first realization of the micro-lens design. Perfecting the lens design, making the phase mask deeper and the step size more gradual could increase the light intensity at the tight focal spot, as compared to intensity of the incident light, by an order of magnitude.

Table 1 shows examples of the optical characteristics for two different microlenses, along with a comparison to a bare, flat silicon wafer (with unmodified surface). First, the surface reflection is reduced from 30% for a planar silicon surface to only 11% or 14% for the nano-patterned surfaces (due to improved impedance matching). Second, lens focusing power for this microlens should be characterized by two different parameters: distance to a plane of minimal spot size, and a distance to a plane with maximal power concentration within a smaller square, (such as a quarter of the original square lens area). In particular, more than one-third of the input beam power can be concentrated into a half-pixel size square, $15\mu m$ x $15\mu m$, near the center of a beam passing through the lens. Meanwhile, peak intensity can be doubled (Fig. 8.9) at the plane of smallest spot size when compared to the flat silicon wafer. Focal distances observed for our 18 micro-lenses varied from about $160\mu m$ (see Fig. 8.8), up to approximately half a millimeter, $450\mu m$ and $510\mu m$ for the two lenses with a circular and square design, respectively (as listed in Table 8.1). This variation is due to both the variety of lens designs tested, as well as to finite tolerance of manufacturing process used.

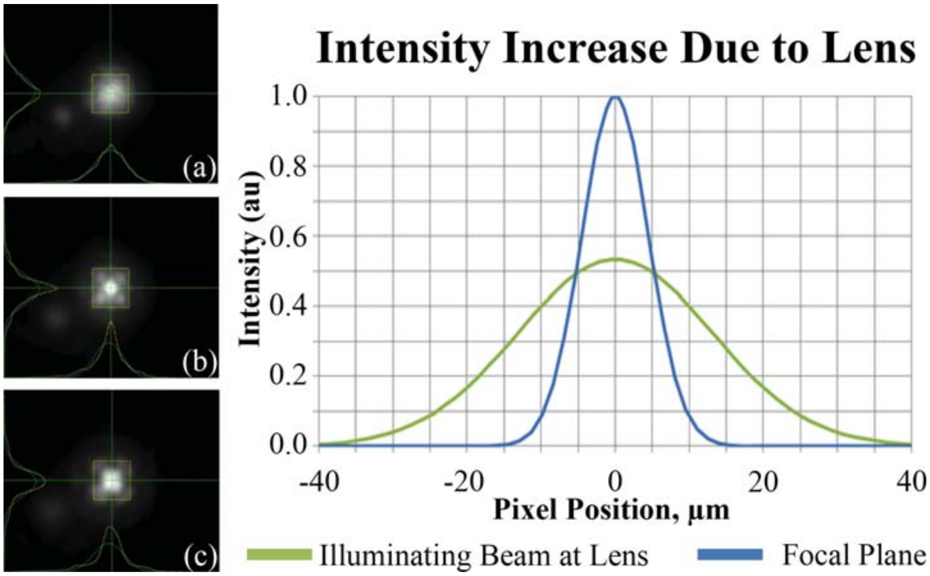

Fig. 8.9. The light intensity distribution at the micro-lens surface (a), at the minimal spot size focusing plane (b), and at two focal lengths behind the focusing plane (c). The yellow frame depicts a 30μm × 30μm square representing the size of the original lens. Secondary reflection spots are visible near left lower corner of the photos. The intensity of the Gaussian beam at the micro-lens input (green) is compared to the measured intensity at the focusing plane (blue) for one of the micro-lenses (d). This particular micro-lens increased the axial intensity by a factor of 1.87.

8.7 Conclusion

In conclusion, we have demonstrated a sub-wavelength thin planar all-dielectric metamaterial lens patterned on a silicon wafer surface. A transparent dielectric substrate with no metal elements avoids light absorption as light passes through the metamaterial layer (in contrast to plasmonic meta-surfaces). One key advantage of this micro-lens design is a reduction in the insertion loss for wafer-level integrated microlenses down to about 10%, making this approach suitable for a variety of narrow-band and moderate bandwidth transmitting lens applications. Although the focusing surface layer was only about 0.5 μm thin, the resulting lens demonstrated a focusing distance of less than 0.5 mm with an attendant reduction in spot size by a factor of three. To design such lenses, we have created a parametric computer model that can calculate the phase of a plane wave passing through pillar structures of varying geometric parameters (including height, slope and diameter). These computer simulations show close correspondence with experimental measurements on fabricated structures.

9. STUDIES OF METAL/DIELECTRIC COMPOSITE SUPERLENS

9.1 Motivation

There is a great deal of interest to utilize an enhanced near-field EM signal. However, as close proximity to a metal surface can provide adverse effects to the sample in question, there is strong interest in creating this strong evanescent enhancement away from the metal surface. For this reason, we have studied the ability of a lamellar near-field superlens to transfer an enhanced electromagnetic field to the far side of the lens. In this work, we have experimentally and numerically investigated superlensing in the visible range. By using the resonant hot-spot field enhancements from optical nanoantennas as sources, we investigated the translation of these sources to the far side of a layered silver-silica superlens operating in the canalization regime. Using near-field scanning optical microscopy (NSOM), we have observed evidence of superlens-enabled enhanced-field translation at a wavelength of about 680 nm. Specifically, we discuss our recent experimental and simulation results on the translation of hot spots using a silver- silica layered superlens design. We compare the experimental results with our numerical simulations and discuss the perspectives and limitations of our approach. In this scheme, the localized and enhanced electromagnetic fields (or hot spots) could be created by optical nanoantennas [15, 18, 176, 177], and the hot-spot transfer with a superlens could be useful in applications such as surface-enhanced Raman spectroscopy (SERS) [178] or enhanced fluorescence microscopy [23]. Optical hot spots are important for a range of important bio-, chemical- and medical-sensing applications, including surface-enhanced Raman scattering [179] and enhanced fluorescence [177]. It has also been shown theoretically that an optical hot spot can be translated through a near-field superlens [180]. Such a setup is preferable to direct contact with a metal, which has been shown to cause structural and functional changes in biomolecules [181], including denaturation of proteins [182]. Furthermore, very close proximity with metal nanoparticles can cause fluorescence to be quenched rather than enhanced [183].

9.2 Background

In 1873, Ernst Abbe postulated that it is impossible to focus light below a certain limit due to diffraction effects. Termed the Abbe limit or the diffraction limit, this idea was fundamentally challenged in 2000 with the proposal of a sub-diffraction superlens by Pendry [7], which was based on the 1968 paper on negative-index materials by Veselago [6]. Pendrys initial superlens would, in principle, work for propagating (or far-field) waves and would allow unlimited resolution in the image of an object. This superlens design required some rather strict conditions on the permittivity and permeability of the superlens material, however. Pendrys proposal also included a simplified, near-field superlens design that required only a negative permittivity, rather than simultaneously negative permittivity and permeability. Near-field superlensing was experimentally demonstrated in 2005 by Fang and coworkers [26] and nearly simultaneously by Melville and Blaikie [27], followed by others [184]. However, the practical applications of near-field superlenses are still quite limited due to the fact that the permittivities of the lens and the surrounding medium must be equal in sign and opposite in magnitude. Because many metals have negative permittivities in the visible range, they are a natural choice for superlenses. For superlensing operation, the matching condition $\epsilon_{metal} = -\epsilon_{dielectric}$ must be satisfied [7] for the real parts of the permittivities. For dispersive materials, this condition means that superlens operation can only be achieved at a single wavelength for each material system. In the case of the silver-polymer combination used in many of the initial near-field superlens demonstrations, the matching condition is met at a wavelength of around 365 nm [6, 26, 27]. However, superlensing in the visible or near-infrared wavelength range promises a number of exciting applications. Several solutions have been proposed to bring superlensing to this spectral range, including the use of metaldielectric composites (MDCs) [28, 185–187] and multilayer lens structures. These solutions allow the designer to select or tune the superlens operational wavelength by adjusting the fabrication procedure appropriately. Note that in using the term tune here we mean that the operational wavelength of the superlens can be selected prior to fabrication. If such a tunable near-field superlens could be achieved, it would open up many promising applications based on the spatial translation (or transfer) of highly localized, enhanced electromagnetic fields [188–195] to the other side of a superlens [196].

Although we have studied both MDCs and multilayer superlens designs in our research, here we focus on the latter category, specifically lamellar, multilayer metal-dielectric devices for superlensing in the visible range. Therefore, as a side note, we briefly mention some of the experimental [197] and numerical simulation [198] results on our work with MDC films. Metal-dielectric composites or MDCs are materials that consist of a random mixture of subwavelength metallic in a dielectric host (or alternatively, small dielectric particles in a metallic host); such materials are sometimes called cermets. In principle, according to effective-medium theories, MDCs permit a designer to adjust the effective permittivity of the mixture through selecting the constituent materials and the relative volume fractions. Ideally, such a MDC material should produce a selectable effective permittivity at any wavelength in a wide range while maintaining low loss. We have observed that it is indeed possible to adjust the real part of the permittivity of a superlens based on MDC films, and hence the superlens operational wavelength can be tailored for a particular application simply by altering the volume ratio between the metal and dielectric components in the composite. However, we also discovered that passive MDC designs are inherently too lossy to be useful in real superlens applications [197, 198]. It is due to this overwhelming loss that we turned our attention to lamellar, multilayer superlens designs.

Single-layer and multilayer near-field superlenses have been studied by a number of researchers in recent years. Most experimental studies have focused on the plasmonic operational regime, which is limited to the near-UV range for noble metals and common dielectrics. In this regime, the matching condition is met directly through the careful selection of the metal and dielectric materials, and the wavelength of operation is not adjustable once the material combination is determined. Numerical studies have also predicted the existence of a canalization regime in which superlensing occurs in a highly anisotropic, layered, metal- dielectric system at wavelengths away from the plasmon resonance and into the visible range. This canalization regime has been experimentally observed in the microwave range. In this work, we have experimentally and numerically investigated superlensing in the visible range. Using the resonant hot-spot enhancements from arrays of optical nanoantennas as sources, we investigated the translation of these sources to the far side of a layered silver-silica superlens operating in the canalization regime. With the technique of near-field scanning optical microscopy (NSOM), we have observed evidence of superlens-enabled enhanced-field translation at a wavelength of about 680 nm. The experimental evaluation of the fabricated samples included NSOM, scanning electron microscopy (SEM), atomic force microscopy (AFM) and far-field spectroscopy. We have also studied the samples extensively using FDTD simulations to evaluate their near-field electromagnetic behavior. Finally, we summarize and compare our experimental results with respective numerical simulations and discuss the perspectives and limitations of our approach.

Lamellar, multilayered metal-dielectric systems such can be used for wavelength-selectable near-field superlenses in the canalization regime. A schematic of such a multilayered lens design is shown in the left panel of Figure 9.1, and an SEM image of a prototype multilayer structure is shown in the right panel of the figure. These multilayered metal-dielectric systems can be considered to be uniaxial crystals that exhibit a flat, hyperbolic dispersion relation [33,179]. Multilayered systems have been extensively studied theoretically, and their lensing and optical properties have been discussed by a number of authors [148,179,180,199,200].

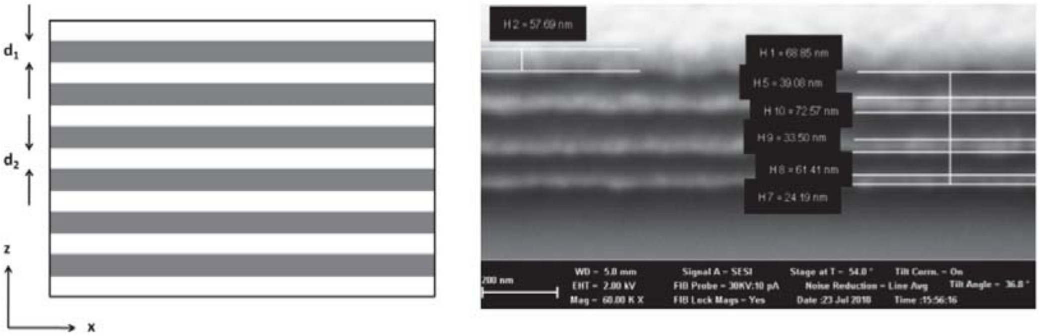

Fig. 9.1. Schematic of a lamellar, alternating multilayer metal-dielectric system (left). The metal is white, the dielectric is gray, and the layers are subwavelength in thickness. This scheme provides a method of adjusting the operational wavelength of a superlens. A cross-section SEM view of a silver- silica prototype superlens design with layer thicknesses labeled (right).

A metal-dielectric multilayered system with subwavelength layer thicknesses exhibits an anisotropic permittivity characterized by the dispersion functions (9.1) [179]

$$\epsilon_x = \epsilon_y = \frac{\epsilon_d d_1 + \epsilon_m d_2}{d_1 + d_2}, \epsilon_z = \left(\frac{\epsilon_d^{-1} d_1 + \epsilon_m^{-1} d_2}{d_1 + d_2} \right)^{-1} \tag{9.1}$$

where ϵ_d and ϵ_m are the bulk permittivities of the dielectric and metal constituents, respectively, and the thicknesses are as labeled in Fig. 9.1. In superlensing applications, we are interested in obtaining a system with a parallel permittivity of unity for impedance matching ($\epsilon_x = \epsilon_y = 1$) and an infinite perpendicular permittivity ($\epsilon_z \to \infty$). This is known as the canalization regime [179]. In practice, however, due to losses and material limitations, both conditions cannot be fulfilled simultaneously. These multilayer films are not restricted to operation at a single wavelength for a given material combination; the operational wavelength can be tuned simply by altering the relative thicknesses of the metal and dielectric layers.

9.2.1 Nanoantenna Pattern Design and Fabrication

As stated above, we were primarily interested in studying the ability of a near-field superlens to transfer field-enhanced optical hot spots, and hence our first step was to design an array of optical nanoantennas to produce these hot-spot sources. The antenna design was based on pairs of identical rhombus-shaped metal structures with a narrow gap between the two. It is in this narrow gap where electromagnetic energy is localized and where the hot spot is produced. These very high local field intensities are created between antenna pairs only when the pair is illuminated with correctly polarized light (that is, light that is polarized parallel to the long axis of the antenna pair). This antenna design choice was selected based on existing expertise from previous work [177].

Schematic designs of our antenna array are shown in Fig. 9.2. Each individual antenna has a characteristic size X, which is the length of the minor axis. In our case, X was about 80nm. The major axis is twice as long (160nm), and the second antenna is placed along this axis, with a gap of 20nm separating the two. The antenna pairs are spaced with a periodicity of 4X (320nm) along the minor axis and 8X (640nm) along the major axis (see Figure 9.2).

The nanoantenna fabrication was performed by electron-beam lithography (EBL) on a quartz substrate in large, 500μm × 500 μm arrays in order to permit far-field optical characterization the final samples. Following EBL photoresist patterning and development, a reactive-ion etch procedure was used to create 40nm holes in the quartz substrate. Next, a 1nm layer of Ge followed by a 40nm layer of Ag was deposited into these holes, resulting in a flatter topography than would be possible without etching. For simplicity, light polarized along the major axis (across the gap) will be referred to as parallel or x-polarized, while light polarized along the minor axis will be referred to as perpendicular or y-polarized light. The antenna array was designed to be resonant under parallel-polarized light at a wavelength of about 633nm.

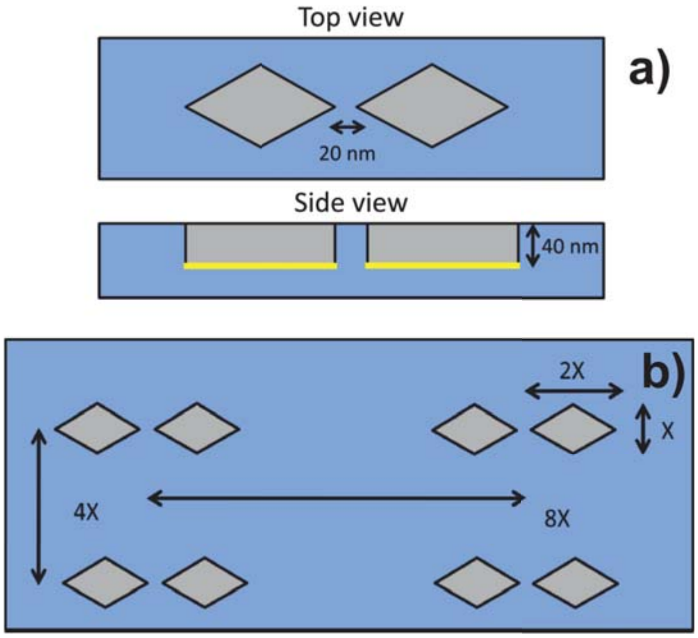

Fig. 9.2. Schematics of the basic nanoantenna design. (a) A nanoantenna pair in top view and cross section. Two 40nm thick rhombus-shaped antennas form a single pair and are spaced 20nm apart. The antenna pair is embedded into a quartz substrate. (b) The individual antenna pairs are part of larger arrays. The size of the individual antennas is related to the spacing of the array. The size parameter X can be varied in order to achieve different resonance wavelengths. In the arrays we studied in this work, X was 80nm.

9.2.2 Superlens Design

The superlens design was based on finite-element model (FEM, COMSOL Multiphysics) calculations and modeling using a chromium grating to simulate lens performance at a resolution of 100nm, which was the grating half-pitch. The results from these initial numerical simulations indicated that subwavelength resolution might be possible without impedance matching, with $\lambda/6$ resolution achieved for a single-layer silver lens with a SiO_2 host. The highest contrast was achieved for a three-layer superlens design. However, the intensity transmission through the sample was expected to be too low for NSOM measurements for this configuration. As a result, a single-layer design was chosen since it provided the best compromise between contrast and transmission. The superlens design consisted of a 20nm silver layer covered on both sides by 21nm SiO_2 layers. While not included in the model, a 1nm germanium adhesion layer was added below the silver layer in order to lower the silver roughness and decrease the loss. The germanium layer itself is not expected to add much loss due to the very low thickness and relatively low loss at 633nm.

We designed and fabricated three different types of samples for our experimental investigations. Although the three sets of samples have exactly the same nanoantenna design, the regions above samples differ in their overlayer designs (see Figure 3). The first sample type was simply uncovered or bare nanoantennas with no overlayer. In the superlens samples, the nanoantennas are covered with 21nm of silica, 20nm of silver, and another 21nm of silica. In the final type of sample, the nanoantennas were covered with a 62nm silica layer. This is an equivalent thickness to that in the superlens samples, and hence these samples were used as reference samples. The reference and bare nanoantenna samples were used to compare the near-field intensity distributions to those of the superlens samples. In all samples, the overlayers were fabricated using electron-beam evaporation. The cross-sections of the three sample types are shown schematically in Figure 9.3

9.2.3 Sample Characterization

We performed a number of tests in order to evaluate the quality of the fabricated samples and to characterize their properties. These tests were focused on the antenna shape as well as the planarization and quality of the silver layer. We first used scanning electron microscope (SEM) imaging to study the uncoated antenna arrays, an example of which can be seen in Fig. 9.4. The antenna shape was generally well reproduced, though the finite size of metallic grains does lead to a rounding of the edges. As we will show, this rounding was taken into account in our numerical simulations. In general, however, the nanoantenna elements were all generally very uniform with no missing antenna pairs.

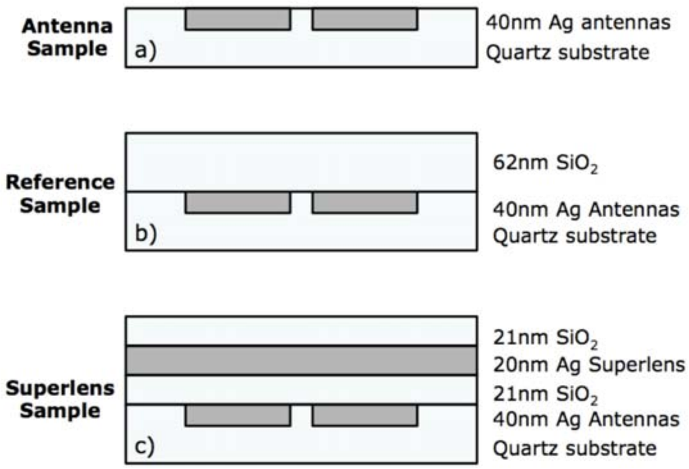

Fig. 9.3. Cross-section of the three types of samples examined in this study. a) the bare antenna sample, b) the reference sample with a dielectric spacer above the antennas, and c) the superlens sample with layered metal and dielectric films above the antenna arrays.

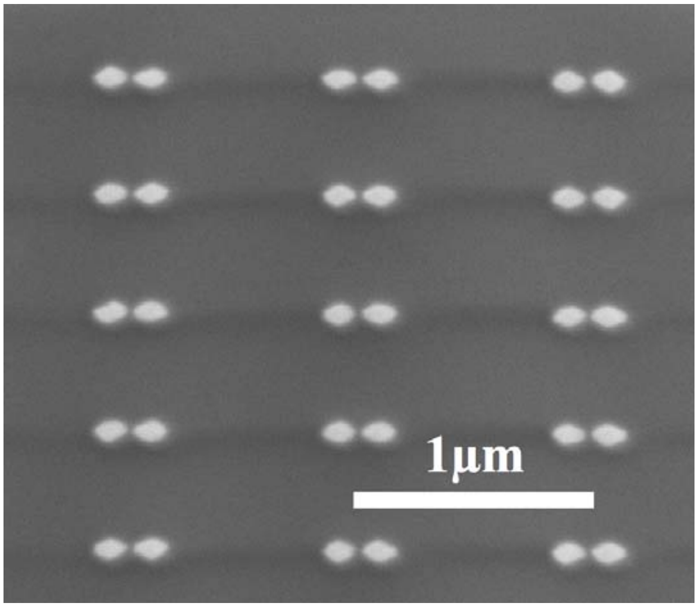

Fig. 9.4. SEM image of a nanoantenna array (X = 80nm). The pattern is well reproduced with a gap size around 20nm. Some minor variations in antenna shape can be observed, which can be ascribed to the finite metal grain size. The slight rounding of the corners of the nanoantennas is accounted for in our numerical simulations.

We also used atomic force microscope (AFM) imaging to investigate the roughness and surface quality of the embedded nanoantennas. Our goal was to produce a flat final surface with minimized height deviations between the antennas and the surrounding substrate within the antenna arrays. The AFM results (not shown here) indicate that the embedding was generally very good, and the average height variation between the antennas and the substrate was less than 5nm RMS. In addition, we studied the quality of the deposited 35nm silver / 1nm germanium superlens layers with AFM. This was done on a test sample with no SiO_2 cover layer in order to allow direct access to the silver material. The results show good film uniformity with a small grain size and a low roughness of 0.5nm RMS. For comparison purposes, we also deposited 35nm silver films directly on SiO_2 with no germanium adhesion layer. In this case, the AFM results show a much higher surface roughness of 2.7nm RMS.

9.2.4 Far-Field Characterization

The nanoantenna array was characterized optically via far-field transmission measurements using a supercontinuum light source (Koheras) with a broad emission range from 500nm to 2000nm. The light was focused on the sample with a focus size of 200-300μm, and a linear polarizer was used to adjust the incident light polarization. After passing through the sample, the light was refocused and coupled into a spectrometer. Background reference measurements were taken through the sample in an area free of visual defects and outside of the nanoantenna array. The reference intensities were then subtracted from the array intensities in order to give a relative transmission measurement.

As expected from theory [15,201], a strong resonance was seen for parallel-polarized (x-polarized) light, and it is this resonance that is of interest in our work. For the bare antenna array with a size parameter of X = 80nm, the resonance occurred at a wavelength of 620nm, which is close to the expected 633nm resonant wavelength. A weaker resonance was seen for light polarized orthogonal to the long axis of the antennas pairs (perpendicular or y polarization). This weaker resonance wavelength was blue-shifted compared to that of the parallel polarization. Optical transmission measurements were also performed after depositing the reference silica layer or the silver/silica superlens layers on top of the bare antennas, and we observed significant changes in the transmission spectra. For the reference sample, a red shift of about 40nm was observed in the resonance position. This shift was expected, since the SiO_2 covering increases the refractive index around the antennas as compared to air. For the superlens-covered sample, however, the red shift was slightly larger (45nm). In fact, when we collected spectra from nanoantenna arrays with different size parameters, we found that the resonant wavelength shift for silica-coated antennas was about 40nm for all arrays, while the shift for superlens-covered arrays depended on the initial resonance position. Antenna arrays with an initial resonance of about 500nm showed no resonance shift with the addition of the superlens, while antennas with a resonance around 700nm shifted by as much as 100nm when we added the superlens layers. We attribute this to coupling between the antennas and silver superlens layer. As a result of this shift, the reference samples have a different resonance wavelength than the superlens samples, even for otherwise identical antennas. Around our wavelength of interest ($\approx$ 633nm), the difference is slight, but for antennas outside this range the difference can be significant, which complicates any direct comparisons between the superlens and reference samples.

9.2.5 Near-Field Characterization

We performed a large number of NSOM scans in order to study the near-field intensity distribution on the samples. These measurements were carried out at The Max Planck Institute for the Science of Light and Friedrich-Alexander-Universitt (Erlangen, Germany) and at Purdue University (West Lafayette, Indiana, USA). The NSOM setup in Erlangen was equipped with an acousto-optic tunable filter in combination with a supercontinuum light source, which enabled the selection of any incident-light wavelength from 450nm to 700nm. The setup also included a linear polarizer, and NSOM measurements were taken with a highly modified Nanonics 4000 system. The NSOM setup at Purdue was a Nanonics 2000 system but was limited to 633nm light and did not have polarization control in our measurements. In both systems we used metal-coated aperture NSOM tips with sizes ranging from 150nm down to 50nm, and in both systems we also used avalanche photodiodes (APDs) for detecting the collected light intensity. Several types of NSOM scans are possible, with each type providing different near-field information about the sample. Schematics of three main NSOM modes are shown Fig. 9.5. In reflection-mode NSOM (Fig. 9.5, left panel), the sample is illuminated in the near field via the tapered-fiber NSOM tip, and the far-field reflected or scattered light is measured from the sample. In transmission-mode NSOM (Fig. 9.5, middle panel), the sample is again illuminated in the near field with the tapered-fiber tip, but in this case the transmitted light is collected in the far-field. In our measurements we used collection mode NSOM scanning (Fig. 9.5, right panel). In this case, the sample is illuminated from the bottom with far-field light that is transmitted through the sample, and the near-field intensity is collected with the NSOM tip.

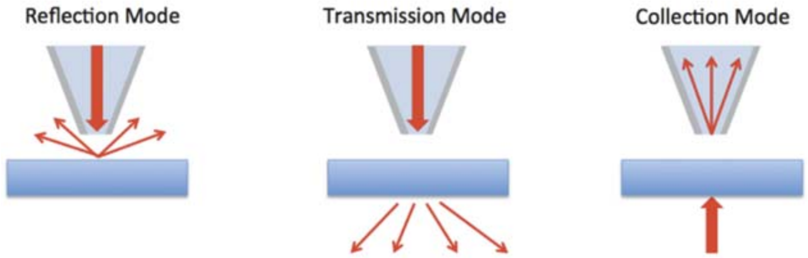

Fig. 9.5. Three types of NSOM scanning modes. The thick arrow represents illumination of the sample. The thin arrows represent the collected or measured light. In this work we focused on collection mode NSOM (right panel) for our near-field measurements.

With the NSOM system in Erlangen, we performed numerous NSOM measurements on the nanoantenna array with a size parameter X = 80 nm, and scans were taken at wavelengths ranging from 530 nm to 680 nm in steps of 10 nm and with both parallel and perpendicular light polarizations. At Purdue, measurements were done at 633 nm with unpolarized light. In both systems, the measurements were done on superlens samples as well as on reference samples and bare nanoantenna samples. The scan sizes were either 5μm × 5μm or 10μm × 10 μm. The resolution was kept constant at 128 data points per 5μm. We note that we have observed some complications in interpreting our experimental NSOM results. These issues are related to several factors, such as the fact that the fiber tips experience gradual degradation over time. In addition, there are necessary manual alignments in both of our NSOM systems, which is another source of discrepancies in comparing the data from one sample to the next. When we combine these concerns with the automatic intensity rescaling performed by the Nanonics software, we conclude that the measured intensity values cannot be compared directly between scans.

9.3 Bare Antennas

When scanning the bare antenna samples under perpendicularly polarized (y-polarized) light at 620nm, no resonance was observed, which is consistent with our far-field measurements. In this polarization, the antennas simply block part of the incoming light. Thus the antennas appear as regions with lower intensities, an example of which is shown in Figure 9.6. The resolution in the scan in Fig. 9.6 is sufficient to see individual antenna pairs, but we cannot resolve individual antenna elements.

When illuminating the array with light at the parallel polarization (x-polarized), a periodic enhancement of the intensity is observed. This resonance has a periodicity equal to the array periodicity, it overlaps with the light that is simply transmitted through the sample, and its peak intensity is well above that of the incident light. However, this is not the nanoantenna hot-spot resonance, which can be seen in two ways. First, when we compared the AFM and NSOM data we observed that the highest intensity regions are in the areas between the antenna pairs, whereas the hot-

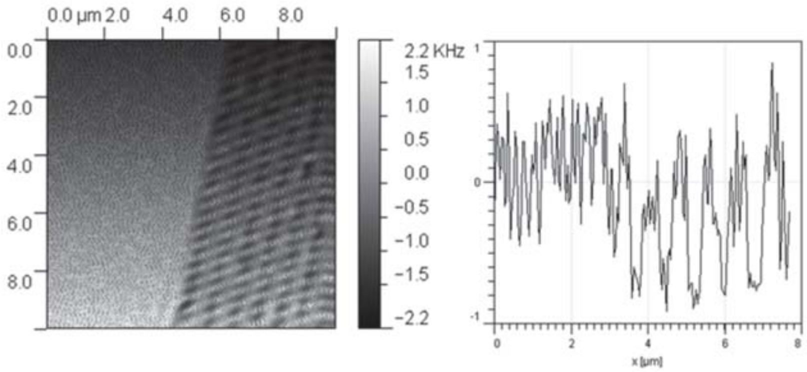

Fig. 9.6. NSOM scan (left) and intensity cross-section (right) of a bare antenna array illuminated with perpendicular-polarized light at 620 nm. The antenna pairs can be observed as dark regions because they block some of the light transmitted through the substrate.

spot resonance should occur in the gap in the middle of the antenna pair. Second, when looking at the edge of an array, we see that the periodic enhancement extends well beyond the boundaries of the antenna array, as seen in Fig. 9.7. This behavior shows that the resonance is actually a propagating mode, and thus it is not the highly localized hot-spot nanoantenna resonance. Note in Fig. 9.7 and in many of our NSOM scans that we were not able to reliably resolve the antenna pairs in the vertical direction of the image (the y-direction) because the periodicity is smaller in that direction.

At this point it is important that we note some peculiarities of our antenna array pattern with respect to the expected resonance wavelength of the reference and superlens samples. It has been shown that coupled nanoantenna resonances die out when the distance between the antenna elements exceeds 2.5 times that of the particle size [201], which is why the nanoantenna arrays used here have a spacing of three times the particle size (corresponding to center-to-center distance of four times the size parameter X, or about 320 nm for our X = 80nm array). However, for our silver nanoantennas this spacing had the unintended consequence of producing a periodicity (8 × 80nm = 640 nm) that is very close to the shifted resonance wavelength of the reference and superlens samples. As a result, the nanoantenna array acts es-

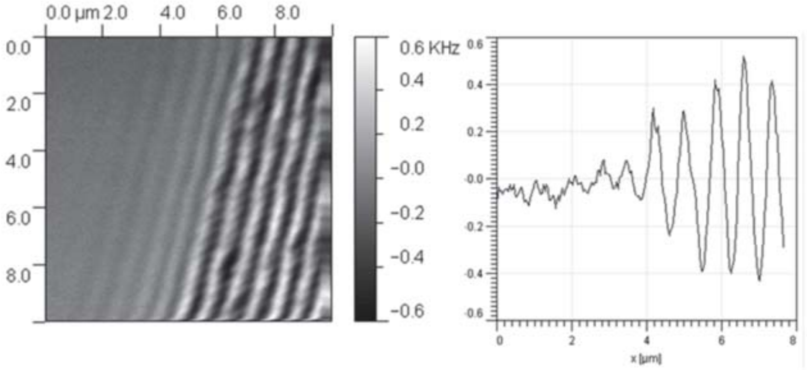

Fig. 9.7. NSOM scan (left) and cross-section (right) of a bare nanoantenna array illuminated with parallel-polarized light at 620 nm. In the cross-section scan, the antenna array boundary is at 4 μm. A periodic resonance is observed that extends well beyond the boundaries of the array and decays with distance from the array. In this resonant mode, the peak intensities are significantly higher than that of the incident light.

sentially as a grating with a periodicity of λ in one direction and a periodicity of $\lambda/2$ in the other direction; such gratings have been shown previously to couple light from free space into propagating surface or waveguide modes [202, 203]. We expect this grating-coupled propagating mode to travel inside the silica of the substrate itself, which could act as a waveguide due to its high refractive index compared to the surrounding air. We will discuss this grating-coupled mode in more detail in later sections.

9.4 Superlens and Reference Samples

Returning to our preliminary NSOM data, we observed a different field-enhancement distribution near the expected resonance wavelength of 665nm (620nm + 45nm shift) on the superlens samples. Here a second resonance appears with the same spacing as the periodic mode described earlier but shifted by half a period. As shown in Fig. 9.8, this resonance is not present at 620nm, but it can be seen as very low intensity peaks at 650nm, and it is even stronger still at 680nm. At 680nm this extra resonance mode reaches roughly the same intensity as the propagating mode, which gives it the appearance of a simple doubling in frequency. No scans were performed at longer wavelengths, since the wavelength limit of the setup had been reached, so it is not known if the intensity grows even more at longer wavelengths.

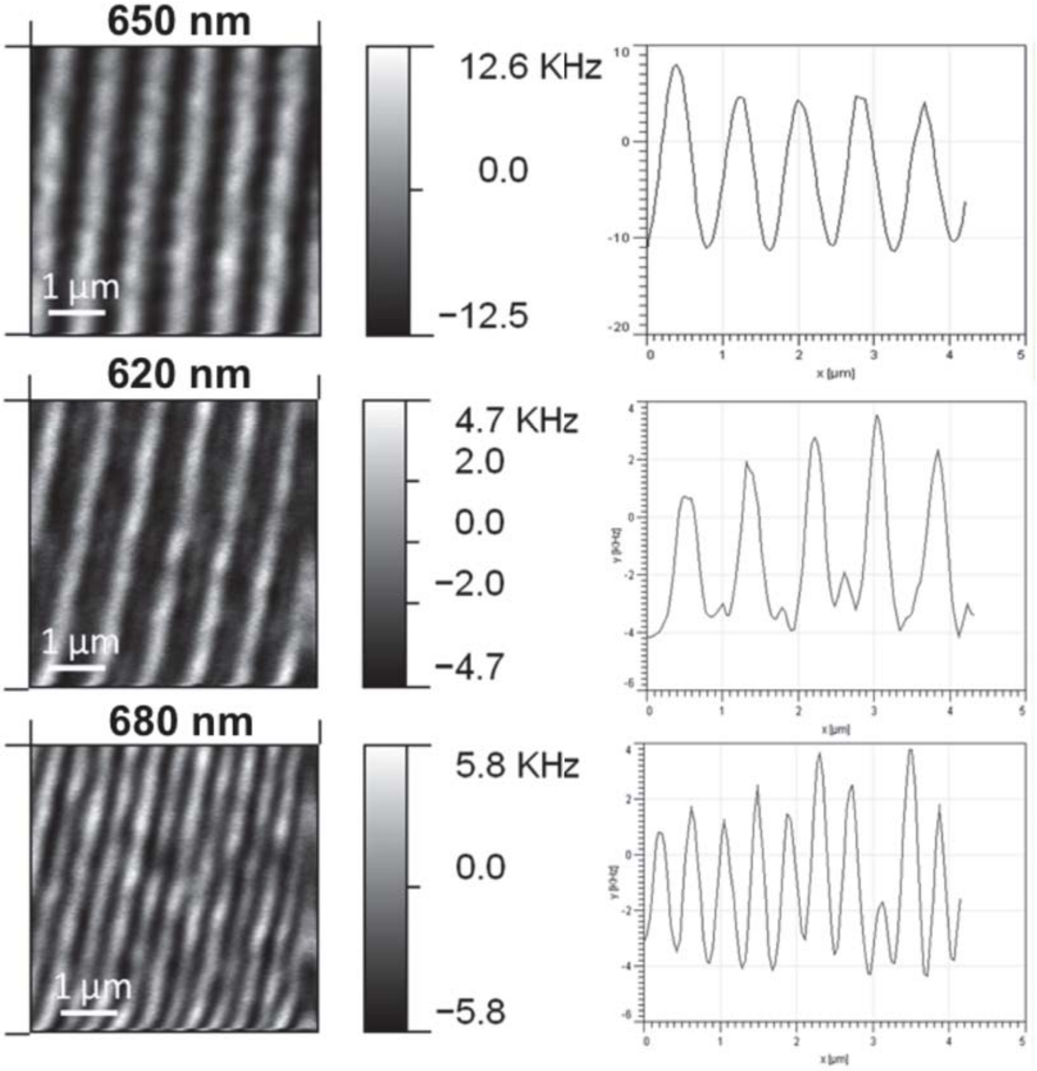

Fig. 9.8. NSOM scans of the intensity distribution (left) and intensity cross-section (right) measured on a superlens sample for three different wavelengths. At 620nm (top) only the propagating mode is seen, at 650nm (middle) a weaker second mode starts to appear, and at 680 nm (bottom) the weaker mode has grown in strength to equal the propagating mode.

In addition to the appearance of this second resonance, we also see that the widths of the intensity peaks were reduced significantly at 680nm. In order to investigate the origin of this second resonance, an NSOM scan was performed using the same wavelength (680nm) but with perpendicularly polarized light, and the results show no sign of the additional resonance. Furthermore, identical scans were taken on a reference sample to see if this effect was related to the silver superlens layer, and once again no secondary resonance was observed. These scans are shown in Fig. 9.9

With this preliminary NSOM data in mind, we conclude that there were two main phenomena occurring in our results. The first and most interesting was the appearance of the second resonance mode, which occurred only near a specific wavelength and in a particular polarization. The second phenomenon was the narrowing of the intensity peaks. We see three possible contributions to the near-field intensity patterns in our NSOM scans: (1) light transmitted through the sample in the bare areas between the antenna pairs, (2) the grating-coupled propagating mode, and (3) the localized field enhancement from the nanoantennas. Because the secondary resonance appears very close to the expected resonance frequency of the nanoantennas, and only at the correct polarization, it appears to be our sought-after nanoantenna hot-spot resonance.

Furthermore, the narrowing of the intensity peaks would be consistent with an increased extinction cross-section for the nanoantennas at resonance, which would have the effect of stealing light from the surrounding area. This line of reasoning suggests that this additional field enhancement is indeed the localized nanoantenna resonance, and that the superlens allows it to be resolved on the far side of the lens, which is not possible on the reference sample. However, due to the similarity of this resonance to the propagating mode, more information and additional measurements are needed to confirm this hypothesis. In the next section we discuss these further measurements as well as the numerical simulations we performed in support of our experimental results.

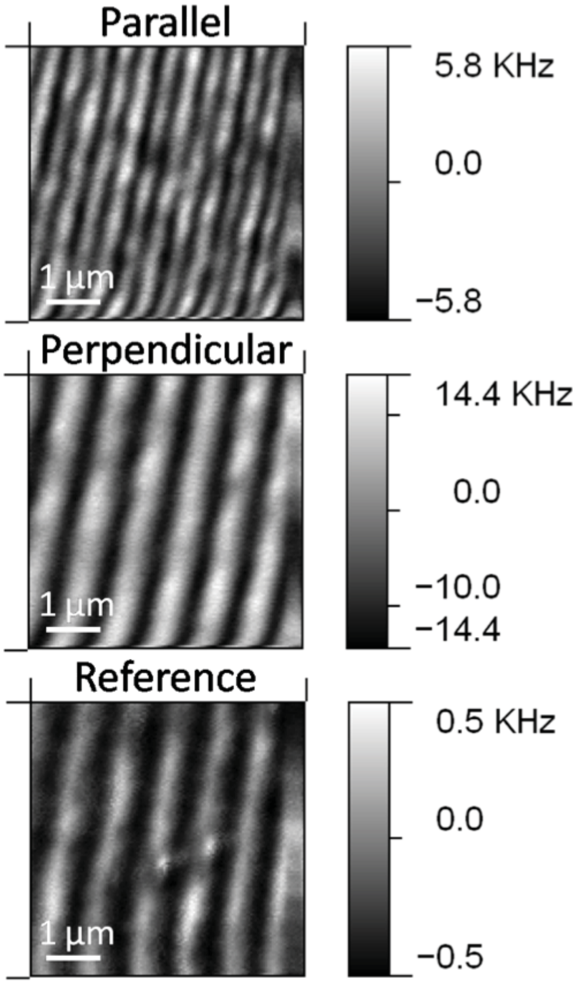

Fig. 9.9. Comparison of the NSOM intensity distributions for the same antenna array under three different conditions. In addition to the propagating mode, a second resonance mode was observed for the parallel polarization on a superlens sample (top panel), which caused the appearance of frequency doubling. No such mode was observed for the perpendicular polarization on the same sample (middle), or for the parallel polarization on a reference sample (bottom). All data was taken at an incident wavelength of 680 nm.

9.5 FDTD Simulations for Far-Field Spectra and Near-field Intensity Maps of the Superlens and Reference Samples

After obtaining our preliminary NSOM results, it was clear that numerical simulations on the antenna structures and cover layers would give us valuable insight into understanding the intensity profiles in our experimental results. We chose to use the finite-difference time-domain (FDTD) method for our simulations because the results with our new generalized dispersion model [204] are quite accurate and, with the extensive cluster computing facilities available at Purdue, full 3D simulations were possible.

As noted previously, the fabricated nanoantennas were slightly more elliptical than the initial rhombus-shaped design. Because the shape of the antenna plays a strong role in determining the overall plasmonic response, more realistic elliptical-shaped antennas were used in our simulations. The gap between antennas was fixed at 20nm, and the geometry of the simulated unit cell of the antenna array can be seen Fig. 9.10.

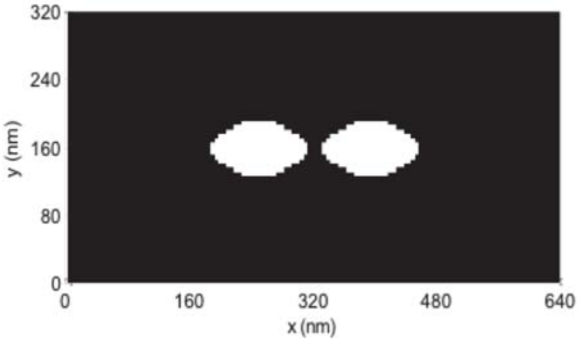

Fig. 9.10. Elliptically-shaped nanoantenna pair used as the unit cell of the array in the FDTD simulations. The shape of these antennas corresponds more closely with the actual shape of the nanoantennas, as indicated in our SEM results. In this image, white is metal (silver) and black is dielectric material (glass).

We calculated full-wave responses of the three types of samples at a variety of incident wavelengths and polarizations. Some representative near-field intensity maps are shown below. In the simulated intensity maps, many unit cells are shown in an array in order to mimic the scan area of the experimental NSOM results. The intensities were calculated at a distance of 10nm above the top surface of the sample; this was done in order to mimic the NSOM tip scanning distance. Finally, the calculated intensities were averaged with a 150nm circular averaging function in order to mimic the aperture area of the NSOM tip. For convenience, the ellipses in the lower left area of each image show the locations of the nanoantennas inside the simulated domain. The details of the material models used in our FDTD simulations can be found in our previous publication [198].

The nanoantenna structures were simulated for the three sample types (bare antenna, superlens, and reference sample) using fully 3D FDTD calculations. The bare antenna sample was simulated under 620nm and 633nm illumination schemes, corresponding to the resonance wavelength and the Purdue NSOM laser source, respectively. The superlens and reference samples were each simulated at 660nm and 680nm, corresponding to the measured far-field resonance and the wavelength of the observed double-periodicity pattern, respectively. For each wavelength, the field distributions were calculated under parallel polarization (x-polarized, resonant case) as well as under perpendicular polarization (y-polarized, off-resonant case). For each polarization, the field intensity components were calculated along each axis direction ($|E_x|^2$, $|E_y|^2$, $|E_z|^2$). The computational domain used for these simulations was 640nm and 320nm in the x- and y- directions (the z- direction is normal to the substrate surface), and was 4000nm in the z- direction. The spatial discretization was 5nm, and the time discretization was about 4.814583×10^{-18}s. We used perfectly-matched layer (PML) boundaries in the z- direction, and periodic boundary conditions (PBCs) were applied to all other sides (that is, in the x- and y- directions) of the simulation domain. The electric field (E-field) and magnetic field (H-field) for each unit cell were discretized, and thus the intensity of each cell was defined as $|E_{total}|^2 = |E_x|^2 + |E_y|^2 + |E_z|^2$. This total field intensity ($|E_{total}|^2$) corresponds with the intensity measured experimentally with NSOM. In all our FDTD simulations, the germanium layer was omitted and the 21nm and 62nm thicknesses were rounded-off to 20nm and 60nm, respectively. This was done in order to accommodate the finite-sized grid of the simulation domain. The incident wave illuminated the sample from the bottom in order to simulate the experimental situation in collection-mode NSOM measurements.

9.5.1 Representative FDTD Near-Field Intensity Maps for Bare Antenna Sample

In Fig. 9.11 we show representative FDTD near-field intensity maps resulting from our numerical simulations. These intensity maps were calculated for the bare antenna sample at an incident wavelength of 620nm for both polarizations. Since the intensities are not normalized among the maps, corresponding scale bars are included for each image. These maps indicate that in the parallel polarization the near-field intensity is dominated by the x- and z-components of the field, while in the perpendicular polarization it is the y component that dominates the total intensity. This trend is consistent for all of our calculated intensity maps at all wavelengths. Notably, the strong z-component contribution indicates a strong grating-coupled diffraction mode within the intensity distribution. This corresponds to our earlier NSOM analysis that there is a strong propagating mode in the antenna array under parallel-polarized light.

9.6 Comparing FDTD Simulations to NSOM

We can now compare the total, FDTD-calculated intensity distributions $|E_{total}|^2$ to the experimentally measured NSOM results. For each sample (bare antennas, superlens, and reference), we show images of the NSOM scans in the parallel and perpendicular incident light polarizations. The FDTD simulation results for the same polarizations are shown below the corresponding experimental scans. Schematic insets on the NSOM scans show the incident-light polarization and the orientation of the antennas (not to scale). Although all the simulations results have been averaged over an area roughly the size of the NSOM tip aperture, it is still obvious that the simulation results are much clearer than the NSOM measurements. We attribute this loss in resolution in the NSOM scans to a possible larger tip aperture due to inevitable damage during scanning, to sample/tip interactions that perturb the near-field, and/or to imperfections in fabrication. It should be noted that in most of the

NSOM measurements, the sample image is rotated roughly 15° from vertical. This slight orientation offset is due to the fact that sample alignment in the NSOM is done manually, and it is therefore quite difficult to align the sample precisely.

9.6.1 Bare Antenna Sample

We begin with our results for the bare antenna structure in Fig. 9.12. Both the simulations and the NSOM results were performed with illumination at a wavelength of 620nm, which corresponds to the transmission dip (resonance) observed in our far-field measurements.

Note that, as before, we see stripes in the NSOM images due to the inability to resolve the rows of antenna pairs, although we can resolve the columns of the array. We see very little difference between the NSOM scans for the two polarizations on the bare antenna sample (top row of Fig. 9.12). The only differences are slightly broader high-intensity stripes in the perpendicular polarization than in the parallel polarization. Comparing the FDTD results (bottom row of Fig. 9.12), we see that the parallel-polarized light is strongly confined to the antenna gap, which is expected from the previous far-field measurements, and the intensity does not extend as far in the y direction as in the x-direction. In the case of perpendicularly polarized light, the intensity is not localized to the antenna gap, and the intensity profile is broader in both the x- and y-directions. Both of these results agree reasonably well with our NSOM results.

9.6.2 Superlens Sample

In Fig. 9.13 we show the NSOM scans and simulation results for the superlens sample measured and simulated with 680nm incident light. In this case, the FDTD simulations correspond very well with the NSOM results. We clearly see that the parallel-polarized light exhibits double periodicity (two intensity peaks per antenna pair), while the perpendicularly polarized light exhibits single periodicity. The double periodicity of the parallel-polarized light can be attributed almost entirely to the $|E_z|^2$ component of the field (data not shown). This is indicative of diffraction coming from the antenna structures, rather than the antenna hot-spot transfer that we were seeking. However, the intensity profile still shows subwavelength confinement on the far side of the superlens.

To further validate this hypothesis, scans were taken at Purdue with unpolarized, 633nm light at the edge of the antenna array, as seen in Fig 9.14. The left image of Fig. 9.14 shows the AFM height profile that was measured concurrently with the NSOM scan. While the antennas cover only about 40% of the image, the intensity pattern extends throughout the whole NSOM image. This further indicates that a propagating diffraction mode dominates the near-field intensity profile on the far side of the superlens.

9.6.3 Reference Sample

Fig. 9.15 shows the experimental NSOM and corresponding simulation images for the reference sample, which has only a dielectric spacer above the nanoantenna arrays. In this case, both the simulations and the NSOM results were found using 660nm incident light. The FDTD simulations for the reference sample correspond reasonably well with the NSOM results. The simulation for parallel-polarized light shows a very wide and ill-defined profile in the high-intensity stripes, and the NSOM results show similar results with relatively wide, poorly defined stripes. For the case of perpendicularly polarized incident light, the NSOM results clearly show high intensities for the areas adjacent to the individual antenna pairs. These results also correspond quite well with the FDTD simulation, where strong intensities are predicted for the areas adjacent to the antenna pairs.

9.7 Conclusions and Final Remarks

We have studied lamellar superlens designs using experimental measurements and advanced numerical simulations. For this work, three different sample types were prepared: bare antennas, antennas with a silver superlens, and antennas with a reference dielectric layer. Each sample was designed, fabricated, and characterized to ascertain how the enhanced-field hot spot created by the antennas was translated to the top side of the sample. In-depth FDTD simulations were performed to compare with experimental measurements, and after analyzing the results, we conclude that the superlens is not strongly transferring the antenna hot spot to the top side of the sample. However, the superlens does provide the unintended consequence of transferring a diffraction grating to the far side of the superlens, and this still provides subwavelength confinement of energy that could be used in enhanced sensing applications or other devices.

In fact, this phenomenon provides a method of tailoring the localized, subwavelength near-field enhancement of a superlens-translated intensity distribution. By adjusting the sizes, shapes and periodicities of the nanoantenna array, we can apply a genetic algorithm to optimize the near-field intensity distribution on the far side of a superlens. In doing so, we can match the final near-field intensity pattern to a specific application such as sensing or nonlinear-optical studies. This will be our next step in our research on nanoantenna-superlens combinations.

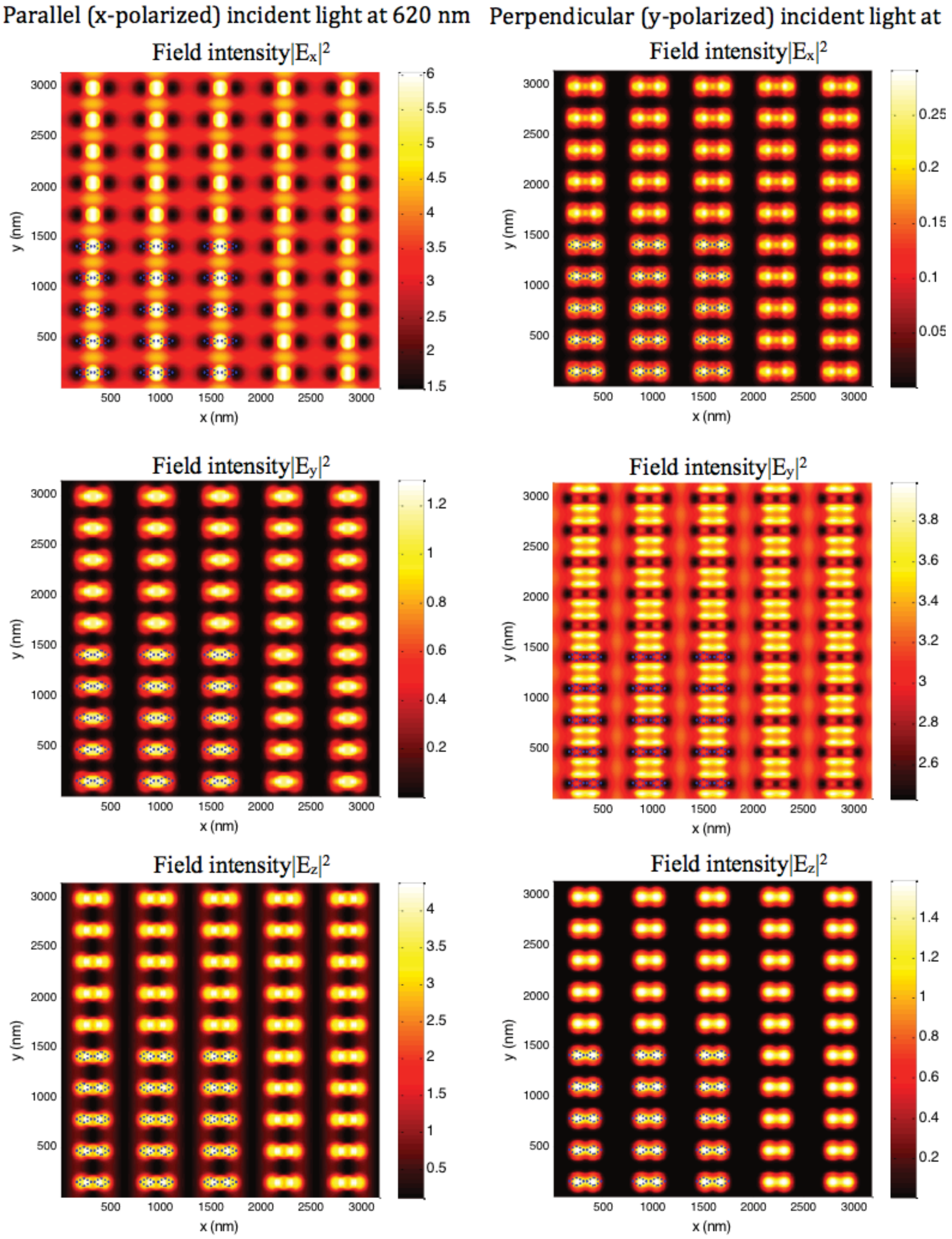

Parallel (x-polarized) incident light at 620 nm

Perpendicular (y-polarized) incident light at

Field intensity$|E_x|^2$

Field intensity$|E_x|^2$

Field intensity$|E_y|^2$

Field intensity$|E_y|^2$

Field intensity$|E_z|^2$

Field intensity$|E_z|^2$

Fig. 9.11. Representative FDTD near-field intensity maps. These maps were calculated for the bare antenna sample with 620nm illuminating light at the parallel polarization (left column) and the perpendicular polarization (right column). The maps show the intensity patterns 10 nm above the sample, averaged in a 150nm radius circle, and plotted for each field component. The corresponding intensity scales (arbitrary units) are also shown. The x- and z-components dominate in the parallel polarization, but the y-component dominates in the perpendicular polarization.

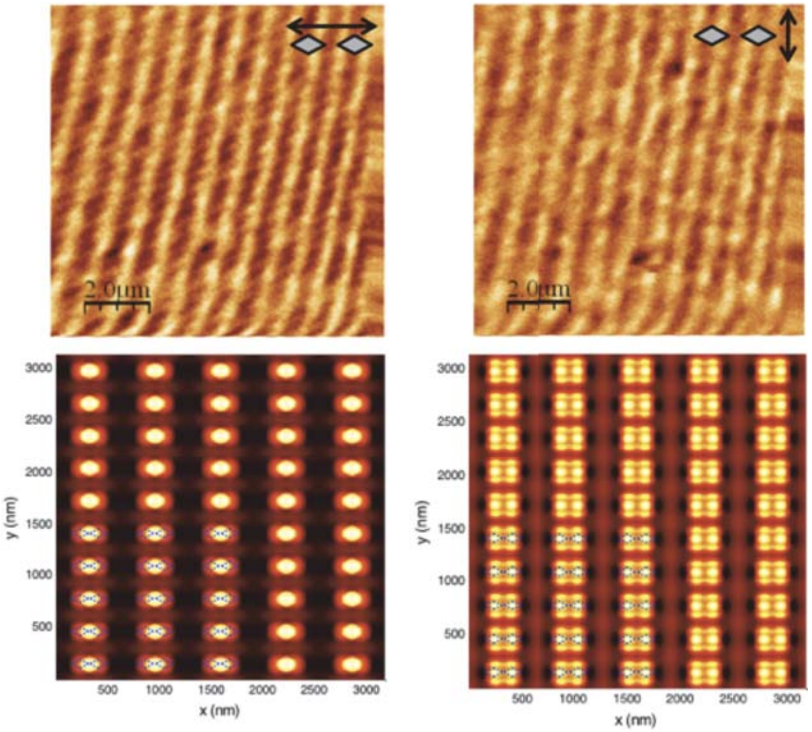

Fig. 9.12. NSOM scans and corresponding total near-field intensity simulations for the bare antenna sample in both polarizations and at an incident wavelength of 620 nm.

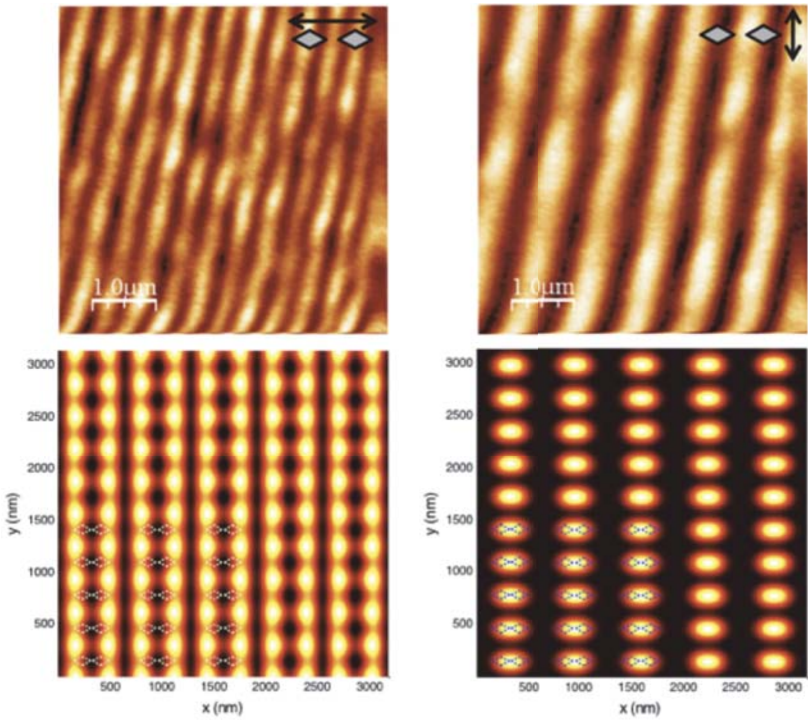

Fig. 9.13. NSOM scans (upper panels) and corresponding total near-field intensity simulations (lower panels) for the superlens sample in both polarizations and at an incident wavelength of 680 nm.

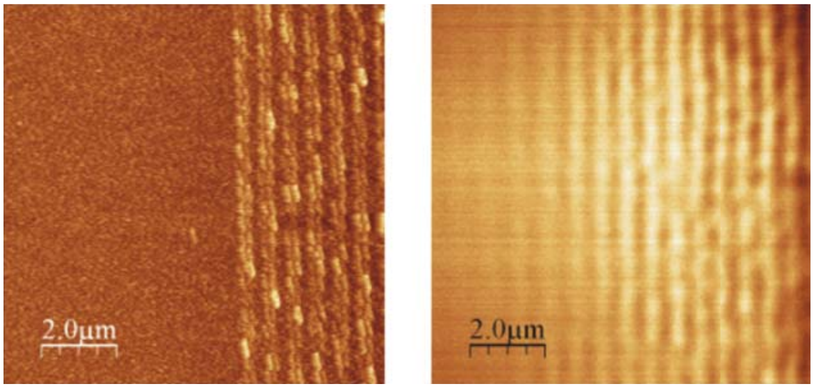

Fig. 9.14. NSOM scans with unpolarized light at the edge of an antenna array. The image on the left shows the topography (height profile) of the sample. The antennas cover roughly 40% of the image. The image on the right shows the corresponding NSOM intensity profile of the same region. The intensity pattern continues beyond the array, indicating a propagating, diffraction-based mode.

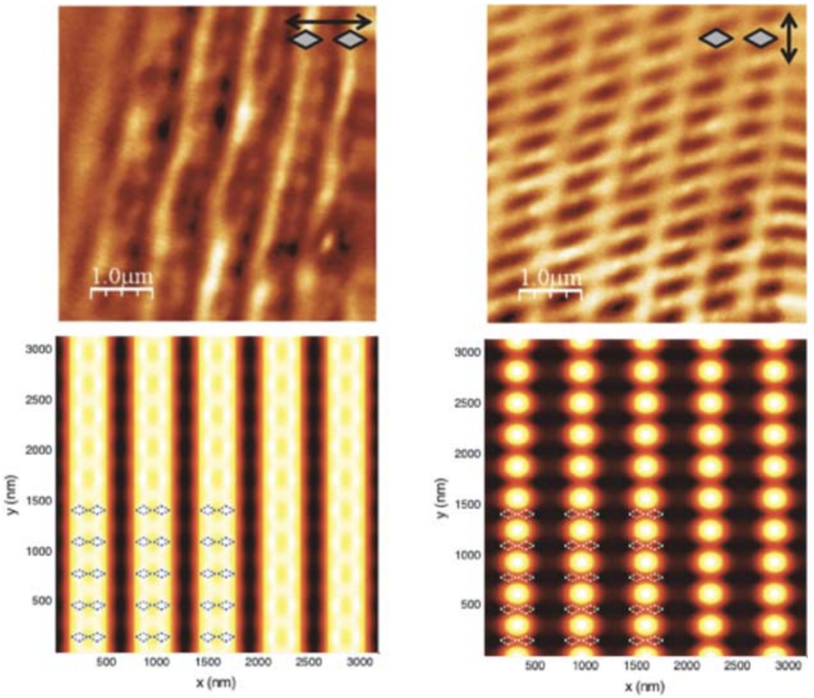

Fig. 9.15. NSOM scans (upper panels) and corresponding total near-field intensity simulations (lower panels) for the reference sample in both polarizations and at an incident wavelength of 660 nm.

LIST OF REFERENCES

LIST OF REFERENCES

[1] E. Ozbay, “Plasmonics: merging photonics and electronics at nanoscale dimensions,” *science*, vol. 311, no. 5758, pp. 189–193, 2006.

[2] R. Ritchie, “Plasma losses by fast electrons in thin films,” *Physical Review*, vol. 106, no. 5, p. 874, 1957.

[3] W. L. Barnes, A. Dereux, T. W. Ebbesen, *et al.*, “Surface plasmon subwavelength optics,” *Nature*, vol. 424, no. 6950, pp. 824–830, 2003.

[4] S. A. Maier and H. A. Atwater, “Plasmonics: Localization and guiding of electromagnetic energy in metal/dielectric structures,” *Journal of Applied Physics*, vol. 98, no. 1, pp. 011101–011101, 2005.

[5] S. Lal, S. Link, and N. J. Halas, “Nano-optics from sensing to waveguiding,” *Nature photonics*, vol. 1, no. 11, pp. 641–648, 2007.

[6] V. G. Veselago *et al.*, “The electrodynamics of substances with simultaneously negative values of ε and μ,” *Physics-Uspekhi*, vol. 10, no. 4, pp. 509–514, 1968.

[7] J. B. Pendry, “Negative refraction makes a perfect lens,” *Physical review letters*, vol. 85, no. 18, pp. 3966–3969, 2000.

[8] A. V. Kildishev and V. M. Shalaev, “Engineering space for light via transformation optics,” *Optics letters*, vol. 33, no. 1, pp. 43–45, 2008.

[9] W. Cai and V. Shalaev, *Optical metamaterials: fundamentals and applications.* Springer, 2009.

[10] A. Ward and J. Pendry, “Refraction and geometry in maxwell’s equations,” *Journal of Modern Optics*, vol. 43, no. 4, pp. 773–793, 1996.

[11] J. B. Pendry, D. Schurig, and D. R. Smith, “Controlling electromagnetic fields,” *Science*, vol. 312, no. 5781, pp. 1780–1782, 2006.

[12] V. M. Shalaev, “Transforming light,” *Science*, vol. 322, no. 5900, pp. 384–386, 2008.

[13] S. A. Maier, P. G. Kik, H. A. Atwater, S. Meltzer, E. Harel, B. E. Koel, and A. A. Requicha, “Local detection of electromagnetic energy transport below the diffraction limit in metal nanoparticle plasmon waveguides,” *Nature materials*, vol. 2, no. 4, pp. 229–232, 2003.

[14] S. I. Bozhevolnyi, V. S. Volkov, E. Devaux, J.-Y. Laluet, and T. W. Ebbesen, “Channel plasmon subwavelength waveguide components including interferometers and ring resonators,” *Nature*, vol. 440, no. 7083, pp. 508–511, 2006.

[15] W. Rechberger, A. Hohenau, A. Leitner, J. Krenn, B. Lamprecht, and F. Aussenegg, “Optical properties of two interacting gold nanoparticles,” *Optics Communications*, vol. 220, no. 1, pp. 137–141, 2003.

[16] D. P. Fromm, A. Sundaramurthy, P. J. Schuck, G. Kino, and W. Moerner, “Gap-dependent optical coupling of single bowtie nanoantennas resonant in the visible,” *Nano Letters*, vol. 4, no. 5, pp. 957–961, 2004.

[17] T. Atay, J.-H. Song, and A. V. Nurmikko, “Strongly interacting plasmon nanoparticle pairs: from dipole-dipole interaction to conductively coupled regime,” *Nano Letters*, vol. 4, no. 9, pp. 1627–1631, 2004.

[18] P. Mühlschlegel, H.-J. Eisler, O. Martin, B. Hecht, and D. Pohl, “Resonant optical antennas,” *Science*, vol. 308, no. 5728, pp. 1607–1609, 2005.

[19] A. Sundaramurthy, K. Crozier, G. Kino, D. Fromm, P. Schuck, and W. Moerner, “Field enhancement and gap-dependent resonance in a system of two opposing tip-to-tip au nanotriangles,” *Physical Review B*, vol. 72, no. 16, p. 165409, 2005.

[20] A. K. Sarychev, G. Shvets, and V. M. Shalaev, “Magnetic plasmon resonance,” *Physical Review E*, vol. 73, no. 3, p. 036609, 2006.

[21] A. Sundaramurthy, P. J. Schuck, N. R. Conley, D. P. Fromm, G. S. Kino, and W. Moerner, “Toward nanometer-scale optical photolithography: utilizing the near-field of bowtie optical nanoantennas,” *Nano letters*, vol. 6, no. 3, pp. 355–360, 2006.

[22] O. Muskens, V. Giannini, J. Sanchez-Gil, and J. G. Rivas, “Strong enhancement of the radiative decay rate of emitters by single plasmonic nanoantennas,” *Nano letters*, vol. 7, no. 9, pp. 2871–2875, 2007.

[23] R. M. Bakker, V. P. Drachev, Z. Liu, H.-K. Yuan, R. H. Pedersen, A. Boltasseva, J. Chen, J. Irudayaraj, A. V. Kildishev, and V. M. Shalaev, “Nanoantenna array-induced fluorescence enhancement and reduced lifetimes,” *New Journal of Physics*, vol. 10, no. 12, p. 125022, 2008.

[24] R. M. Bakker, H.-K. Yuan, Z. Liu, V. P. Drachev, A. V. Kildishev, V. M. Shalaev, R. H. Pedersen, S. Gresillon, and A. Boltasseva, “Enhanced localized fluorescence in plasmonic nanoantennae,” *Applied Physics Letters*, vol. 92, no. 4, pp. 043101–043101, 2008.

[25] N. Fang and X. Zhang, “Imaging properties of a metamaterial superlens,” *Applied Physics Letters*, vol. 82, no. 2, pp. 161–163, 2003.

[26] N. Fang, H. Lee, C. Sun, and X. Zhang, “Sub–diffraction-limited optical imaging with a silver superlens,” *Science*, vol. 308, no. 5721, pp. 534–537, 2005.

[27] D. O. Melville, R. J. Blaikie, *et al.*, “Super-resolution imaging through a planar silver layer,” *Opt. Express*, vol. 13, no. 6, pp. 2127–2134, 2005.

[28] W. Cai, D. A. Genov, and V. M. Shalaev, “Superlens based on metal-dielectric composites,” *Physical Review B*, vol. 72, no. 19, p. 193101, 2005.

[29] D. Schurig, J. Mock, B. Justice, S. A. Cummer, J. Pendry, A. Starr, and D. Smith, “Metamaterial electromagnetic cloak at microwave frequencies,” *Science*, vol. 314, no. 5801, pp. 977–980, 2006.

[30] U. Leonhardt, “Optical conformal mapping,” *Science*, vol. 312, no. 5781, pp. 1777–1780, 2006.

[31] W. Cai, U. K. Chettiar, A. V. Kildishev, and V. M. Shalaev, “Optical cloaking with metamaterials,” *Nature photonics*, vol. 1, no. 4, pp. 224–227, 2007.

[32] A. Alù and N. Engheta, “Multifrequency optical invisibility cloak with layered plasmonic shells,” *Physical review letters*, vol. 100, no. 11, p. 113901, 2008.

[33] Z. Jacob, L. V. Alekseyev, and E. Narimanov, “Optical hyperlens: Far-field imaging beyond the diffraction limit,” *Optics express*, vol. 14, no. 18, pp. 8247–8256, 2006.

[34] A. Salandrino and N. Engheta, “Far-field subdiffraction optical microscopy using metamaterial crystals: Theory and simulations,” *Physical Review B*, vol. 74, no. 7, p. 075103, 2006.

[35] Z. Liu, H. Lee, Y. Xiong, C. Sun, and X. Zhang, “Far-field optical hyperlens magnifying sub-diffraction-limited objects,” *Science*, vol. 315, no. 5819, pp. 1686–1686, 2007.

[36] I. I. Smolyaninov, Y.-J. Hung, and C. C. Davis, “Magnifying superlens in the visible frequency range,” *Science*, vol. 315, no. 5819, pp. 1699–1701, 2007.

[37] D. Schurig, J. Pendry, and D. Smith, “Transformation-designed optical elements,” *Optics Express*, vol. 15, no. 22, pp. 14772–14782, 2007.

[38] Y. Xiong, Z. Liu, and X. Zhang, “A simple design of flat hyperlens for lithography and imaging with half-pitch resolution down to 20 nm,” *Applied Physics Letters*, vol. 94, no. 20, pp. 203108–203108, 2009.

[39] P. B. Johnson and R. Christy, “Optical constants of the noble metals,” *Physical Review B*, vol. 6, no. 12, p. 4370, 1972.

[40] J. Marton and B. Jordan, “Optical properties of aggregated metal systems: Interband transitions,” *Physical Review B*, vol. 15, no. 4, p. 1719, 1977.

[41] A. Sudarkin and P. Demkovich, “Excitation of surface electromagnetic waves on the boundary of a metal with an amplifying medium,” *Sov. Phys. Tech. Phys*, vol. 34, pp. 764–766, 1989.

[42] C. Sirtori, C. Gmachl, F. Capasso, D. L. Sivco, A. L. Hutchinson, A. Y. Cho, *et al.*, “Long-wavelength (λ 8–11.5 μm) semiconductor lasers with waveguides based on surface plasmons,” *Optics letters*, vol. 23, no. 17, pp. 1366–1368, 1998.

[43] M. Nezhad, K. Tetz, and Y. Fainman, “Gain assisted propagation of surface plasmon polaritons on planar metallic waveguides,” *Optics Express*, vol. 12, no. 17, pp. 4072–4079, 2004.

[44] A. Tredicucci, C. Gmachl, F. Capasso, A. L. Hutchinson, D. L. Sivco, and A. Y. Cho, “Single-mode surface-plasmon laser,” *Applied physics letters*, vol. 76, no. 16, pp. 2164–2166, 2000.

[45] D. J. Bergman and M. I. Stockman, “Surface plasmon amplification by stimulated emission of radiation: quantum generation of coherent surface plasmons in nanosystems,” *Physical review letters*, vol. 90, no. 2, p. 27402, 2003.

[46] N. Lawandy, “Localized surface plasmon singularities in amplifying media,” *Applied physics letters*, vol. 85, no. 21, pp. 5040–5042, 2004.

[47] J. Seidel, S. Grafström, and L. Eng, “Stimulated emission of surface plasmons at the interface between a silver film and an optically pumped dye solution,” *Physical review letters*, vol. 94, no. 17, p. 177401, 2005.

[48] M. Noginov, G. Zhu, M. Bahoura, J. Adegoke, C. Small, B. Ritzo, V. Drachev, and V. Shalaev, “Enhancement of surface plasmons in an ag aggregate by optical gain in a dielectric medium,” *Optics letters*, vol. 31, no. 20, pp. 3022–3024, 2006.

[49] T. A. Klar, A. V. Kildishev, V. P. Drachev, and V. M. Shalaev, “Negative-index metamaterials: Going optical,” *Selected Topics in Quantum Electronics, IEEE Journal of*, vol. 12, no. 6, pp. 1106–1115, 2006.

[50] M. Noginov, V. Podolskiy, G. Zhu, M. Mayy, M. Bahoura, J. Adegoke, B. Ritzo, and K. Reynolds, “Compensation of loss in propagating surface plasmon polariton by gain in adjacent dielectric medium,” *Optics express*, vol. 16, no. 2, pp. 1385–1392, 2008.

[51] M. Noginov, G. Zhu, M. Mayy, B. Ritzo, N. Noginova, and V. Podolskiy, “Stimulated emission of surface plasmon polaritons,” *Physical review letters*, vol. 101, no. 22, p. 226806, 2008.

[52] M. Ambati, S. H. Nam, E. Ulin-Avila, D. A. Genov, G. Bartal, and X. Zhang, “Observation of stimulated emission of surface plasmon polaritons,” *Nano letters*, vol. 8, no. 11, pp. 3998–4001, 2008.

[53] N. I. Zheludev, S. Prosvirnin, N. Papasimakis, and V. Fedotov, “Lasing spaser,” *Nature Photonics*, vol. 2, no. 6, pp. 351–354, 2008.

[54] M. Noginov, G. Zhu, A. Belgrave, R. Bakker, V. Shalaev, E. Narimanov, S. Stout, E. Herz, T. Suteewong, and U. Wiesner, “Demonstration of a spaser-based nanolaser,” *Nature*, vol. 460, no. 7259, pp. 1110–1112, 2009.

[55] R. F. Oulton, V. J. Sorger, T. Zentgraf, R.-M. Ma, C. Gladden, L. Dai, G. Bartal, and X. Zhang, “Plasmon lasers at deep subwavelength scale,” *Nature*, vol. 461, no. 7264, pp. 629–632, 2009.

[56] G. V. Naik, V. M. Shalaev, and A. Boltasseva, “Alternative plasmonic materials: beyond gold and silver,” *Advanced Materials*, vol. 25, no. 24, pp. 3264–3294, 2013.

[57] V. P. Drachev, U. K. Chettiar, A. V. Kildishev, H.-K. Yuan, W. Cai, and V. M. Shalaev, “The ag dielectric function in plasmonic metamaterials,” *Optics Express*, vol. 16, no. 2, pp. 1186–1195, 2008.

[58] N. Ashcroft and N. Mermin, *Solid Stale Physics*. Saunders College, Philadelphia, 1976.

[59] H. Ehrenreich and H. Philipp, “Optical properties of ag and cu,” *Physical Review*, vol. 128, no. 4, p. 1622, 1962.

[60] B. Cooper, H. Ehrenreich, and H. Philipp, “Optical properties of noble metals. ii.,” *Physical Review*, vol. 138, no. 2A, p. A494, 1965.

[61] H. Ehrenreich, H. Philipp, and B. Segall, “Optical properties of aluminum,” *Physical Review*, vol. 132, no. 5, p. 1918, 1963.

[62] R. LaVilla and H. Mendlowitz, “Optical constants of aluminum in vacuum ultraviolet,” *Physical Review Letters*, vol. 9, no. 4, pp. 149–150, 1962.

[63] H. Hövel, S. Fritz, A. Hilger, U. Kreibig, and M. Vollmer, “Width of cluster plasmon resonances: Bulk dielectric functions and chemical interface damping,” *Physical Review B*, vol. 48, no. 24, p. 18178, 1993.

[64] B. N. J. Persson, “Surface resistivity and vibrational damping in adsorbed layers,” *Phys. Rev. B*, vol. 44, pp. 3277–3296, Aug 1991.

[65] M. Dressel and G. Grüner, *Electrodynamics of solids: optical properties of electrons in matter*. Cambridge University Press, 2002.

[66] A. D. Rakic, A. B. Djurišic, J. M. Elazar, and M. L. Majewski, “Optical properties of metallic films for vertical-cavity optoelectronic devices,” *Applied Optics*, vol. 37, no. 22, pp. 5271–5283, 1998.

[67] D. Thomas, J. Hopfield, and C. Frosch, “Isoelectronic traps due to nitrogen in gallium phosphide,” *Physical Review Letters*, vol. 15, no. 22, pp. 857–860, 1965.

[68] C. Kittel and P. McEuen, *Introduction to solid state physics*, vol. 7. Wiley New York, 1996.

[69] J. Hopfield, “Theory of the contribution of excitons to the complex dielectric constant of crystals,” *Physical Review*, vol. 112, no. 5, p. 1555, 1958.

[70] J. D. Dow and D. Redfield, “Electroabsorption in semiconductors: the excitonic absorption edge,” *Physical Review B*, vol. 1, no. 8, p. 3358, 1970.

[71] W. Dumke, “Optical transitions involving impurities in semiconductors,” *Physical Review*, vol. 132, no. 5, p. 1998, 1963.

[72] G. Dolling, M. Wegener, C. M. Soukoulis, and S. Linden, “Negative-index metamaterial at 780 nm wavelength,” *Optics letters*, vol. 32, no. 1, pp. 53–55, 2007.

[73] T. W. Ebbesen, H. Lezec, H. Ghaemi, T. Thio, and P. Wolff, “Extraordinary optical transmission through sub-wavelength hole arrays,” *Nature*, vol. 391, no. 6668, pp. 667–669, 1998.

[74] V. M. Shalaev, W. Cai, U. K. Chettiar, H.-K. Yuan, A. K. Sarychev, V. P. Drachev, and A. V. Kildishev, “Negative index of refraction in optical metamaterials,” *Optics Letters*, vol. 30, no. 24, pp. 3356–3358, 2005.

[75] S. A. Maier, *Plasmonics: Fundamentals and Applications: Fundamentals and Applications*. Springer, 2007.

[76] P. Tobiška, O. Hugon, A. Trouillet, and H. Gagnaire, “An integrated optic hydrogen sensor based on spr on palladium,” *Sensors and Actuators B: Chemical*, vol. 74, no. 1, pp. 168–172, 2001.

[77] S. Baldelli, A. S. Eppler, E. Anderson, Y.-R. Shen, and G. A. Somorjai, “Surface enhanced sum frequency generation of carbon monoxide adsorbed on platinum nanoparticle arrays,” *The Journal of Chemical Physics*, vol. 113, p. 5432, 2000.

[78] E. D. Palik, *Handbook of optical constants of solids*, vol. 3. Academic press, 1998.

[79] M. Blaber, M. Arnold, N. Harris, M. Ford, and M. Cortie, “Plasmon absorption in nanospheres: A comparison of sodium, potassium, aluminium, silver and gold,” *Physica B: Condensed Matter*, vol. 394, no. 2, pp. 184–187, 2007.

[80] T. Lewowski, “Photoelectron spectroscopy of thin discontinuous silver films deposited onto a sapphire substrate, near the percolation threshold,” *Thin solid films*, vol. 259, no. 1, pp. 53–58, 1995.

[81] H. Wei and H. Eilers, “From silver nanoparticles to thin films: Evolution of microstructure and electrical conduction on glass substrates,” *Journal of Physics and Chemistry of Solids*, vol. 70, no. 2, pp. 459–465, 2009.

[82] T. Oates and A. Mücklich, “Evolution of plasmon resonances during plasma deposition of silver nanoparticles,” *Nanotechnology*, vol. 16, no. 11, p. 2606, 2005.

[83] D. D. Smith, Y. Yoon, R. W. Boyd, J. K. Campbell, L. A. Baker, R. M. Crooks, and M. George, “Z-scan measurement of the nonlinear absorption of a thin gold film,” *Journal of applied physics*, vol. 86, no. 11, pp. 6200–6205, 1999.

[84] Y. Yagil, P. Gadenne, C. Julien, and G. Deutscher, “Optical properties of thin semicontinuous gold films over a wavelength range of 2.5 to 500 μm,” *Physical Review B*, vol. 46, no. 4, p. 2503, 1992.

[85] K. Seal, M. A. Nelson, Z. C. Ying, D. A. Genov, A. K. Sarychev, and V. M. Shalaev, “Metal coverage dependence of local optical properties of semicontinuous metallic films,” *journal of modern optics*, vol. 49, no. 14-15, pp. 2423–2435, 2002.

[86] A. K. Sarychev and V. M. Shalaev, *Electrodynamics of metamaterials*. World Scientific Publishing Company Incorporated, 2007.

[87] G. H. Chan, J. Zhao, E. M. Hicks, G. C. Schatz, and R. P. Van Duyne, “Plasmonic properties of copper nanoparticles fabricated by nanosphere lithography,” *Nano Letters*, vol. 7, no. 7, pp. 1947–1952, 2007.

[88] C. Langhammer, M. Schwind, B. Kasemo, and I. Zoric, “Localized surface plasmon resonances in aluminum nanodisks,” *Nano letters*, vol. 8, no. 5, pp. 1461–1471, 2008.

[89] G. H. Chan, J. Zhao, G. C. Schatz, and R. P. V. Duyne, “Localized surface plasmon resonance spectroscopy of triangular aluminum nanoparticles,” *The Journal of Physical Chemistry C*, vol. 112, no. 36, pp. 13958–13963, 2008.

[90] J. Quail, J. Rako, and H. Simon, “Long-range surface-plasmon modes in silver and aluminum films,” *Optics letters*, vol. 8, no. 7, pp. 377–379, 1983.

[91] J. R. Lakowicz, C. D. Geddes, I. Gryczynski, J. Malicka, Z. Gryczynski, K. Aslan, J. Lukomska, E. Matveeva, J. Zhang, R. Badugu, *et al.*, “Advances in surface-enhanced fluorescence,” *Journal of fluorescence*, vol. 14, no. 4, pp. 425–441, 2004.

[92] K. Ray, M. H. Chowdhury, and J. R. Lakowicz, “Aluminum nanostructured films as substrates for enhanced fluorescence in the ultraviolet-blue spectral region,” *Analytical chemistry*, vol. 79, no. 17, pp. 6480–6487, 2007.

[93] T. Dörfer, M. Schmitt, and J. Popp, “Deep-uv surface-enhanced raman scattering,” *Journal of Raman Spectroscopy*, vol. 38, no. 11, pp. 1379–1382, 2007.

[94] A. Taguchi, N. Hayazawa, K. Furusawa, H. Ishitobi, and S. Kawata, “Deep-uv tip-enhanced raman scattering,” *Journal of Raman Spectroscopy*, vol. 40, no. 9, pp. 1324–1330, 2009.

[95] V. Guritanu, A. Kuzmenko, D. Van der Marel, S. Kazakov, N. Zhigadlo, and J. Karpinski, “Anisotropic optical conductivity and two colors of mgb_ {2},” *Physical Review B*, vol. 73, no. 10, p. 104509, 2006.

[96] Y. Fudamoto and S. Lee, “Anisotropic electrodynamics of mgb_ {2} detected by optical reflectance,” *Physical Review B*, vol. 68, no. 18, p. 184514, 2003.

[97] R. A. Kaindl, M. A. Carnahan, J. Orenstein, D. S. Chemla, H. M. Christen, H.-Y. Zhai, M. Paranthaman, and D. H. Lowndes, “Far-infrared optical conductivity gap in superconducting mgb_ {2} films,” *Physical review letters*, vol. 88, no. 2, p. 27003, 2001.

[98] J. Tu, G. Carr, V. Perebeinos, C. Homes, M. Strongin, P. Allen, W. Kang, E.-M. Choi, H.-J. Kim, and S.-I. Lee, “Optical properties of c-axis oriented superconducting mgb_ {2} films,” *Physical review letters*, vol. 87, no. 27, p. 277001, 2001.

[99] M.-O. Mun, Y. J. Kim, Y. Park, J. H. Kim, S. Moon, H. Lee, H. Kim, and B. Oh, “Normal-state optical response functions of mgb 2 superconductor,” *Journal of superconductivity*, vol. 15, no. 5, pp. 475–477, 2002.

[100] J.-T. Lue, S.-J. Mu, and I.-C. Wu, “Ellipsometry and structure studies of chromium, molybdenum, and platinum silicides,” *Physical Review B*, vol. 36, no. 3, pp. 1657–1661, 1987.

[101] A. Borghesi, L. Nosenzo, A. Piaggi, G. Guizzetti, C. Nobili, and G. Ottaviani, “Optical properties of tantalum disilicide thin films,” *Physical Review B*, vol. 38, no. 15, p. 10937, 1988.

[102] A. Borghesi, A. Piaggi, G. Guizzetti, F. Nava, and M. Bacchetta, “Optical properties of vanadium silicide polycrystalline films,” *Physical Review B*, vol. 40, no. 5, p. 3249, 1989.

[103] M. Amiotti, A. Borghesi, G. Guizzetti, and F. Nava, “Optical properties of polycrystalline nickel silicides,” *Physical Review B*, vol. 42, no. 14, p. 8939, 1990.

[104] V. Antonov, V. N. Antonov, O. Jepsen, O. Andersen, A. Borghesi, C. Bosio, F. Marabelli, A. Piaggi, G. Guizzetti, and F. Nava, “Optical properties of wsi_ {2},” *Physical Review B*, vol. 44, no. 16, p. 8437, 1991.

[105] Z.-C. Wu, E. Arakawa, J. Jimenez, and L. Schowalter, “Optical properties of epitaxial cosi_ {2} on si from 0.062 to 22.3 ev,” *Physical Review B*, vol. 47, no. 8, p. 4356, 1993.

[106] D. Bobb, G. Zhu, M. Mayy, A. Gavrilenko, P. Mead, V. Gavrilenko, and M. Noginov, "Engineering of low-loss metal for nanoplasmonic and metamaterials applications," *Applied Physics Letters*, vol. 95, no. 15, pp. 151102–151102, 2009.

[107] M. Blaber, M. Arnold, and M. Ford, "Optical properties of intermetallic compounds from first principles calculations: a search for the ideal plasmonic material," *Journal of Physics: Condensed Matter*, vol. 21, no. 14, p. 144211, 2009.

[108] M. Zwilling, P. Schmidt, and A. Weiss, "Experimental and theoretical studies of optical properties on alloys of the intermetallic systems li2ag2- x in x and li2cd2- x in x," *Applied physics*, vol. 16, no. 3, pp. 255–269, 1978.

[109] K. H. Kim, K. C. Park, and D. Y. Ma, "Structural, electrical and optical properties of aluminum doped zinc oxide films prepared by radio frequency magnetron sputtering," *Journal of Applied Physics*, vol. 81, no. 12, pp. 7764–7772, 1997.

[110] I. Hamberg and C. G. Granqvist, "Evaporated sn-doped in2o3 films: basic optical properties and applications to energy-efficient windows," *Journal of Applied Physics*, vol. 60, no. 11, pp. R123–R160, 1986.

[111] A. J. Hoffman, L. Alekseyev, S. S. Howard, K. J. Franz, D. Wasserman, V. A. Podolskiy, E. E. Narimanov, D. L. Sivco, and C. Gmachl, "Negative refraction in semiconductor metamaterials," *Nature materials*, vol. 6, no. 12, pp. 946–950, 2007.

[112] J. A. Schuller, R. Zia, T. Taubner, and M. L. Brongersma, "Dielectric metamaterials based on electric and magnetic resonances of silicon carbide particles," *Physical review letters*, vol. 99, no. 10, p. 107401, 2007.

[113] T. Taubner, D. Korobkin, Y. Urzhumov, G. Shvets, and R. Hillenbrand, "Near-field microscopy through a sic superlens," *Science*, vol. 313, no. 5793, pp. 1595–1595, 2006.

[114] C. Wolfe and G. Stillman, "Self-compensation of donors in high-purity gaas," *Applied Physics Letters*, vol. 27, no. 10, pp. 564–567, 2008.

[115] X. Cao, C. Abernathy, R. Singh, S. Pearton, M. Fu, V. Sarvepalli, J. Sekhar, J. Zolper, D. Rieger, J. Han, *et al.*, "Ultrahigh si+ implant activation efficiency in gan using a high-temperature rapid thermal process system," *Applied physics letters*, vol. 73, no. 2, pp. 229–231, 1998.

[116] P. Robusto and R. Braunstein, "Optical measurements of the surface plasmon of indium-tin oxide," *physica status solidi (a)*, vol. 119, no. 1, pp. 155–168, 1990.

[117] M. Xu, M. Alam, A. Zilkie, K. Zeaiter, and J. Aitchison, "Surface plasmon polaritons mediated by ito at near infrared wavelength," in *Lasers and Electro-Optics, 2008 and 2008 Conference on Quantum Electronics and Laser Science. CLEO/QELS 2008. Conference on*, pp. 1–2, IET, 2008.

[118] F. Michelotti, L. Dominici, E. Descrovi, N. Danz, and F. Menchini, "Thickness dependence of surface plasmon polariton dispersion in transparent conducting oxide films at 1.55 μm," *Optics letters*, vol. 34, no. 6, pp. 839–841, 2009.

[119] C. Rhodes, M. Cerruti, A. Efremenko, M. Losego, D. Aspnes, J.-P. Maria, and S. Franzen, "Dependence of plasmon polaritons on the thickness of indium tin oxide thin films," *Journal of Applied Physics*, vol. 103, no. 9, p. 093108, 2008.

[120] S. Franzen, "Surface plasmon polaritons and screened plasma absorption in indium tin oxide compared to silver and gold," *The Journal of Physical Chemistry C*, vol. 112, no. 15, pp. 6027–6032, 2008.

[121] S. H. Brewer and S. Franzen, "Erratum to optical properties of indium tin oxide and fluorine-doped tin oxide surfaces: correlation of reflectivity, skin depth, and plasmon frequency with conductivity:[j. alloys comp. 338 (2002) 73–79]," *Journal of Alloys and Compounds*, vol. 343, no. 1, p. 244, 2002.

[122] A. Solieman and M. A. Aegerter, "Modeling of optical and electrical properties of in¡ sub¿ 2¡/sub¿ o¡ sub¿ 3¡/sub¿: Sn coatings made by various techniques," *Thin Solid Films*, vol. 502, no. 1, pp. 205–211, 2006.

[123] K. Ellmer and R. Mientus, "Carrier transport in polycrystalline ito and zno: Al ii: the influence of grain barriers and boundaries," *Thin Solid Films*, vol. 516, no. 17, pp. 5829–5835, 2008.

[124] F. Lai, L. Lin, R. Gai, Y. Lin, and Z. Huang, "Determination of optical constants and thicknesses of in2o3:sn films from transmittance data," *Thin Solid Films*, vol. 515, no. 18, pp. 7387 – 7392, 2007.

[125] M. Hiramatsu, K. Imaeda, N. Horio, and M. Nawata, "Transparent conducting zno thin films prepared by xecl excimer laser ablation," *Journal of Vacuum Science & Technology A*, vol. 16, no. 2, pp. 669–673, 1998.

[126] H. Kim, A. Pique, J. Horwitz, H. Murata, Z. Kafafi, C. Gilmore, and D. Chrisey, "Effect of aluminum doping on zinc oxide thin films grown by pulsed laser deposition for organic light-emitting devices," *Thin Solid Films*, vol. 377, pp. 798–802, 2000.

[127] H. Agura, A. Suzuki, T. Matsushita, T. Aoki, and M. Okuda, "Low resistivity transparent conducting al-doped zno films prepared by pulsed laser deposition," *Thin Solid Films*, vol. 445, no. 2, pp. 263–267, 2003.

[128] A. Singh, R. Mehra, N. Buthrath, A. Wakahara, and A. Yoshida, "Highly conductive and transparent aluminum-doped zinc oxide thin films prepared by pulsed laser deposition in oxygen ambient," *Journal of Applied Physics*, vol. 90, no. 11, pp. 5661–5665, 2001.

[129] J. Lu, Z. Ye, Y. Zeng, L. Zhu, L. Wang, J. Yuan, B. Zhao, and Q. Liang, "Structural, optical, and electrical properties of (zn, al) o films over a wide range of compositions," *Journal of Applied Physics*, vol. 100, no. 7, p. 073714, 2006.

[130] M. Yoon, S. Lee, H. Park, H. Kim, and M. Jang, "Solid solubility limits of ga and al in zno," *Journal of materials science letters*, vol. 21, no. 21, pp. 1703–1704, 2002.

[131] K. S. Novoselov, A. K. Geim, S. Morozov, D. Jiang, Y. Zhang, S. Dubonos, I. Grigorieva, and A. Firsov, "Electric field effect in atomically thin carbon films," *science*, vol. 306, no. 5696, pp. 666–669, 2004.

[132] K. Novoselov, A. K. Geim, S. Morozov, D. Jiang, M. Katsnelson, I. Grigorieva, S. Dubonos, and A. Firsov, "Two-dimensional gas of massless dirac fermions in graphene," *nature*, vol. 438, no. 7065, pp. 197–200, 2005.

[133] F. Schedin, A. Geim, S. Morozov, E. Hill, P. Blake, M. Katsnelson, and K. Novoselov, "Detection of individual gas molecules adsorbed on graphene," *Nature materials*, vol. 6, no. 9, pp. 652–655, 2007.

[134] K. V. Emtsev, A. Bostwick, K. Horn, J. Jobst, G. L. Kellogg, L. Ley, J. L. McChesney, T. Ohta, S. A. Reshanov, J. Röhrl, *et al.*, "Towards wafer-size graphene layers by atmospheric pressure graphitization of silicon carbide," *Nature materials*, vol. 8, no. 3, pp. 203–207, 2009.

[135] F. Stern, "Polarizability of a two-dimensional electron gas," *Physical Review Letters*, vol. 18, pp. 546–548, 1967.

[136] E. Hwang and S. D. Sarma, "Dielectric function, screening, and plasmons in two-dimensional graphene," *Physical Review B*, vol. 75, no. 20, p. 205418, 2007.

[137] S. D. Sarma and E. Hwang, "Collective modes of the massless dirac plasma," *Physical review letters*, vol. 102, no. 20, p. 206412, 2009.

[138] V. Ryzhii, A. Satou, and T. Otsuji, "Plasma waves in two-dimensional electron-hole system in gated graphene heterostructures," *Journal of applied physics*, vol. 101, no. 2, pp. 024509–024509, 2007.

[139] H. Wang, J. H. Strait, P. A. George, S. Shivaraman, V. B. Shields, M. Chandrashekhar, J. Hwang, F. Rana, M. G. Spencer, C. S. Ruiz-Vargas, *et al.*, "Ultrafast relaxation dynamics of hot optical phonons in graphene," *Applied Physics Letters*, vol. 96, no. 8, p. 081917, 2010.

[140] V. Ryzhii, M. Ryzhii, A. Satou, T. Otsuji, A. Dubinov, and V. Y. Aleshkin, "Feasibility of terahertz lasing in optically pumped epitaxial multiple graphene layer structures," *Journal of Applied Physics*, vol. 106, no. 8, p. 084507, 2009.

[141] M. Jablan, H. Buljan, and M. Soljačić, "Plasmonics in graphene at infrared frequencies," *Physical review B*, vol. 80, no. 24, p. 245435, 2009.

[142] Z. Li, E. A. Henriksen, Z. Jiang, Z. Hao, M. C. Martin, P. Kim, H. Stormer, and D. N. Basov, "Dirac charge dynamics in graphene by infrared spectroscopy," *Nature Physics*, vol. 4, no. 7, pp. 532–535, 2008.

[143] J. D. Jackson and R. F. Fox, "Classical electrodynamics," *American Journal of Physics*, vol. 67, pp. 841–842, 1999.

[144] F. Wang and Y. R. Shen, "General properties of local plasmons in metal nanostructures," *Physical review letters*, vol. 97, no. 20, p. 206806, 2006.

[145] P. Berini, "Long-range surface plasmon polaritons," *Advances in Optics and Photonics*, vol. 1, no. 3, pp. 484–588, 2009.

[146] M. D. Arnold and M. G. Blaber, "Optical performance and metallic absorption in nanoplasmonic systems," *Optics express*, vol. 17, no. 5, pp. 3835–3847, 2009.

[147] H. Raether, *Surface plasmons on smooth surfaces.* Springer, 1988.

[148] S. A. Ramakrishna, J. Pendry, M. Wiltshire, and W. Stewart, "Imaging the near field," *Journal of Modern Optics*, vol. 50, no. 9, pp. 1419–1430, 2003.

[149] K. Robbie and M. Brett, "Sculptured thin films and glancing angle deposition: Growth mechanics and applications," *Journal of Vacuum Science & Technology A*, vol. 15, no. 3, pp. 1460–1465, 1997.

[150] Y. Zhao, D. Ye, G.-C. Wang, and T.-M. Lu, "Designing nanostructures by glancing angle deposition," in *Optical Science and Technology, SPIE's 48th Annual Meeting*, pp. 59–73, International Society for Optics and Photonics, 2003.

[151] K. Robbie, J. Sit, and M. Brett, "Advanced techniques for glancing angle deposition," *Journal of Vacuum Science & Technology B*, vol. 16, no. 3, pp. 1115–1122, 1998.

[152] M. Y. Shalaginov, S. Ishii, J. Liu, J. Irudayaraj, A. Lagutchev, A. V. Kildishev, and V. M. Shalaev, "Broadband enhancement of spontaneous emission from nitrogen-vacancy centers in nanodiamonds by hyperbolic metamaterials," *Applied Physics Letters*, vol. 102, no. 17, p. 173114, 2013.

[153] W. D. Newman, C. L. Cortes, and Z. Jacob, "Enhanced and directional single-photon emission in hyperbolic metamaterials," *JOSA B*, vol. 30, no. 4, pp. 766–775, 2013.

[154] N. Yu, P. Genevet, M. A. Kats, F. Aieta, J.-P. Tetienne, F. Capasso, and Z. Gaburro, "Light propagation with phase discontinuities: generalized laws of reflection and refraction," *Science*, vol. 334, no. 6054, pp. 333–337, 2011.

[155] F. Aieta, P. Genevet, M. A. Kats, N. Yu, R. Blanchard, Z. Gaburro, and F. Capasso, "Aberration-free ultrathin flat lenses and axicons at telecom wavelengths based on plasmonic metasurfaces," *Nano letters*, vol. 12, no. 9, pp. 4932–4936, 2012.

[156] A. V. Kildishev, A. Boltasseva, and V. M. Shalaev, "Planar photonics with metasurfaces," *Science*, vol. 339, no. 6125, 2013.

[157] N. Yu, F. Aieta, P. Genevet, M. A. Kats, Z. Gaburro, and F. Capasso, "A broadband, background-free quarter-wave plate based on plasmonic metasurfaces," *Nano letters*, vol. 12, no. 12, pp. 6328–6333, 2012.

[158] M. A. Kats, P. Genevet, G. Aoust, N. Yu, R. Blanchard, F. Aieta, Z. Gaburro, and F. Capasso, "Giant birefringence in optical antenna arrays with widely tailorable optical anisotropy," *Proceedings of the National Academy of Sciences*, vol. 109, no. 31, pp. 12364–12368, 2012.

[159] E. S. Bahaa and C. T. Malvin, "Fundamentals of photonics," *New York/A WILEY-INTERSCIENCE PUBLICATION*, 1991.

[160] S. Wilson and M. Hutley, "The optical properties of'moth eye'antireflection surfaces," *Journal of Modern Optics*, vol. 29, no. 7, pp. 993–1009, 1982.

[161] P. Lalanne, S. Astilean, P. Chavel, E. Cambril, and H. Launois, "Design and fabrication of blazed binary diffractive elements with sampling periods smaller than the structural cutoff," *JOSA A*, vol. 16, no. 5, pp. 1143–1156, 1999.

[162] M.-S. L. Lee, S. Bansropun, O. Huet, S. Cassette, B. Loiseaux, A. Wood, C. Sauvan, and P. Lalanne, "Sub-wavelength structures for broadband diffractive optics," in *ICO20: Materials and Nanostructures*, pp. 602919–602919, International Society for Optics and Photonics, 2006.

[163] C. Sauvan, P. Lalanne, and M.-S. L. Lee, "Broadband blazing with artificial dielectrics," *Optics letters*, vol. 29, no. 14, pp. 1593–1595, 2004.

[164] M. Kuittinen, J. Turunen, and P. Vahimaa, "Rigorous analysis and optimization of subwavelength-structured binary dielectric beam deflector gratings," *Journal of Modern Optics*, vol. 45, no. 1, pp. 133–142, 1998.

[165] P. Lalanne, J.-C. Rodier, P. H. Chavel, E. Cambril, A. Talneau, and Y. Chen, "Applications of index-gradient artificial dielectrics," in *Optical Science and Technology, SPIE's 48th Annual Meeting*, pp. 1–7, International Society for Optics and Photonics, 2003.

[166] P. Lalanne and M. Hutley, "The optical properties of artificial media structured at a subwavelength scale," *Encyclopedia of Optical Engineering*, pp. 62–71, 2003.

[167] J. Feng and Z. Zhou, "Polarization beam splitter using a binary blazed grating coupler," *Optics letters*, vol. 32, no. 12, pp. 1662–1664, 2007.

[168] J. Feng and Z. Zhou, "High efficiency compact grating coupler for integrated optical circuits," in *Asia-Pacific Optical Communications*, pp. 63511H–63511H, International Society for Optics and Photonics, 2006.

[169] P. Lalanne, "Waveguiding in blazed-binary diffractive elements," *JOSA A*, vol. 16, no. 10, pp. 2517–2520, 1999.

[170] W. Freese, T. Kämpfe, E.-B. Kley, and A. Tünnermann, "Design and fabrication of a highly off-axis binary multi-phase-level computer-generated hologram based on an effective medium approach," in *SPIE MOEMS-MEMS*, pp. 792710–792710, International Society for Optics and Photonics, 2011.

[171] W. Yu, K. Takahara, T. Konishi, T. Yotsuya, and Y. Ichioka, "Fabrication of multilevel phase computer-generated hologram elements based on effective medium theory," *Applied optics*, vol. 39, no. 20, pp. 3531–3536, 2000.

[172] V. Raulot, B. Serio, P. Gérard, P. Twardowski, and P. Meyrueis, "Modeling of a diffractive micro-lens by an effective medium method," in *SPIE Photonics Europe*, pp. 77162J–77162J, International Society for Optics and Photonics, 2010.

[173] B. Kleemann, "Blazed diffractive optical element and projection objective for a microlithographic projection exposure apparatus," Aug. 28 2007. US Patent 7,262,915.

[174] M.-S. L. Lee, P. Lalanne, J. Rodier, P. Chavel, E. Cambril, and Y. Chen, "Imaging with blazed-binary diffractive elements," *Journal of Optics A: Pure and Applied Optics*, vol. 4, no. 5, p. S119, 2002.

[175] D. Fattal, J. Li, Z. Peng, M. Fiorentino, and R. G. Beausoleil, "A silicon lens for integrated free-space optics," in *Integrated Photonics Research, Silicon and Nanophotonics*, p. ITuD2, Optical Society of America, 2011.

[176] J. N. Farahani, D. W. Pohl, H.-J. Eisler, and B. Hecht, "Single quantum dot coupled to a scanning optical antenna: a tunable superemitter," *Physical Review Letters*, vol. 95, no. 1, p. 017402, 2005.

[177] Z. Liu, A. Boltasseva, R. H. Pedersen, R. Bakker, A. V. Kildishev, V. P. Drachev, and V. M. Shalaev, "Plasmonic nanoantenna arrays for the visible," *Metamaterials*, vol. 2, no. 1, pp. 45–51, 2008.

[178] K. Kneipp, M. Moskovits, and H. Kneipp, *Surface-enhanced Raman scattering: physics and applications*, vol. 103. Springer, 2006.

[179] P. A. Belov and Y. Hao, "Subwavelength imaging at optical frequencies using a transmission device formed by a periodic layered metal-dielectric structure operating in the canalization regime," *Physical Review B*, vol. 73, no. 11, p. 113110, 2006.

[180] B. Wood, J. Pendry, and D. Tsai, "Directed subwavelength imaging using a layered metal-dielectric system," *Physical Review B*, vol. 74, no. 11, p. 115116, 2006.

[181] R. E. Holt and T. M. Cotton, "Surface-enhanced resonance raman and electrochemical investigation of glucose oxidase catalysis at a silver electrode," *Journal of the American Chemical Society*, vol. 111, no. 8, pp. 2815–2821, 1989.

[182] M. Yang, F. L. Chung, and M. Thompson, "Acoustic network analysis as a novel technique for studying protein adsorption and denaturation at surfaces," *Analytical Chemistry*, vol. 65, no. 24, pp. 3713–3716, 1993.

[183] P. Anger, P. Bharadwaj, and L. Novotny, "Enhancement and quenching of single-molecule fluorescence," *Physical review letters*, vol. 96, no. 11, p. 113002, 2006.

[184] C. Jeppesen, R. B. Nielsen, A. Boltasseva, S. Xiao, N. Mortensen, and A. Kristensen, "Thin film ag superlens towards lab-on-a-chip integration," *Optics express*, vol. 17, no. 25, pp. 22543–22552, 2009.

[185] A. V. Kildishev, W. Cai, U. K. Chettiar, H.-K. Yuan, A. K. Sarychev, V. P. Drachev, and V. M. Shalaev, "Negative refractive index in optics of metal-dielectric composites," *JOSA B*, vol. 23, no. 3, pp. 423–433, 2006.

[186] L. Shi, L. Gao, S. He, and B. Li, "Superlens from metal-dielectric composites of nonspherical particles," *Physical Review B*, vol. 76, no. 4, p. 045116, 2007.

[187] L. Shi, L. Gao, and S. He, "Tunable negative refraction and subwavelength imaging in the metal-dielectric composites of nonspherical particles," in *Biophotonics, Nanophotonics and Metamaterials, 2006. Metamaterials 2006. International Symposium on*, pp. 463–466, IEEE, 2006.

[188] P. Aravind, A. Nitzan, and H. Metiu, "The interaction between electromagnetic resonances and its role in spectroscopic studies of molecules adsorbed on colloidal particles or metal spheres," *Surface Science*, vol. 110, no. 1, pp. 189–204, 1981.

[189] E. Hao and G. C. Schatz, "Electromagnetic fields around silver nanoparticles and dimers," *The Journal of chemical physics*, vol. 120, no. 1, pp. 357–366, 2003.

[190] R. M. Bakker, A. Boltasseva, Z. Liu, R. H. Pedersen, S. Gresillon, A. V. Kildishev, V. P. Drachev, and V. M. Shalaev, "Near-field excitation of nanoantenna resonance," *Optics Express*, vol. 15, no. 21, pp. 13682–13688, 2007.

[191] V. Shalaev and M. Stockman, "Optical properties of fractal clusters (susceptibility, surface enhanced raman scattering by impurities)," *Sov. Phys. JETP*, vol. 65, pp. 509–522, 1987.

[192] V. Markel, L. Muratov, M. I. Stockman, and T. F. George, "Theory and numerical simulation of optical properties of fractal clusters," *Physical Review B*, vol. 43, no. 10, p. 8183, 1991.

[193] V. M. Shalaev, "Electromagnetic properties of small-particle composites," *Physics Reports*, vol. 272, no. 2, pp. 61–137, 1996.

[194] V. A. Podolskiy, A. K. Sarychev, E. E. Narimanov, and V. M. Shalaev, "Resonant light interaction with plasmonic nanowire systems," *Journal of Optics A: Pure and Applied Optics*, vol. 7, no. 2, p. S32, 2005.

[195] U. K. Chettiar, A. V. Kildishev, T. A. Klar, and V. M. Shalaev, "Negative index metamaterial combining magnetic resonators with metal films," *Optics express*, vol. 14, no. 17, pp. 7872–7877, 2006.

[196] Z. Liu, M. D. Thoreson, A. V. Kildishev, and V. M. Shalaev, "Translation of nanoantenna hot spots by a metal-dielectric composite superlens," *Applied physics letters*, vol. 95, no. 3, p. 033114, 2009.

[197] R. B. Nielsen, M. Thoreson, W. Chen, A. Kristensen, J. Hvam, V. M. Shalaev, and A. Boltasseva, "Toward superlensing with metal-dielectric composites and multilayers," *Applied Physics B*, vol. 100, pp. 93–100, 2010.

[198] M. D. Thoreson, J. Fang, A. V. Kildishev, L. J. Prokopeva, P. Nyga, U. K. Chettiar, V. M. Shalaev, and V. P. Drachev, "Fabrication and realistic modeling of three-dimensional metal-dielectric composites," *Journal of Nanophotonics*, vol. 5, no. 1, pp. 051513–051513, 2011.

[199] P. Chaturvedi and N. X. Fang, "Molecular scale imaging with a multilayer superlens," in *MRS Proceedings*, vol. 919, Cambridge Univ Press, 2006.

[200] E. Shamonina, V. Kalinin, K. Ringhofer, and L. Solymar, "Imaging, compression and poynting vector streamlines for negative permittivity materials," *Electronics Letters*, vol. 37, no. 20, pp. 1243–1244, 2001.

[201] K.-H. Su, Q.-H. Wei, X. Zhang, J. Mock, D. R. Smith, and S. Schultz, "Interparticle coupling effects on plasmon resonances of nanogold particles," *Nano Letters*, vol. 3, no. 8, pp. 1087–1090, 2003.

[202] T. W. Ebbesen, C. Genet, and S. I. Bozhevolnyi, "Surface-plasmon circuitry," *Physics Today*, vol. 61, no. 5, p. 44, 2008.

[203] V. A. Sychugov, A. V. Tishchenko, B. A. Usievich, and O. Parriaux, "Optimization and control of grating coupling to or from a silicon-based optical waveguide," *Optical Engineering*, vol. 35, no. 11, pp. 3092–3100, 1996.

[204] L. J. Prokopeva, J. D. Borneman, and A. V. Kildishev, "Optical dispersion models for time-domain modeling of metal-dielectric nanostructures," *Magnetics, IEEE Transactions on*, vol. 47, no. 5, pp. 1150–1153, 2011.

APPENDICES

A. ELECTROMAGNETIC BOUNDARY CONDITIONS FOR NANOMETER-SCALE CONFINEMENT AT METAL-DIELECTRIC INTERFACES

This chapter provides a brief outline of how plasmonics is used to confine electromagnetic waves to a very thin, planar metal interface. The principles examined in this chapter will be used to describe plasmonic materials and devices in future chapters. We will begin by exploring the metal / dielectric interface shown in Fig. A.1.

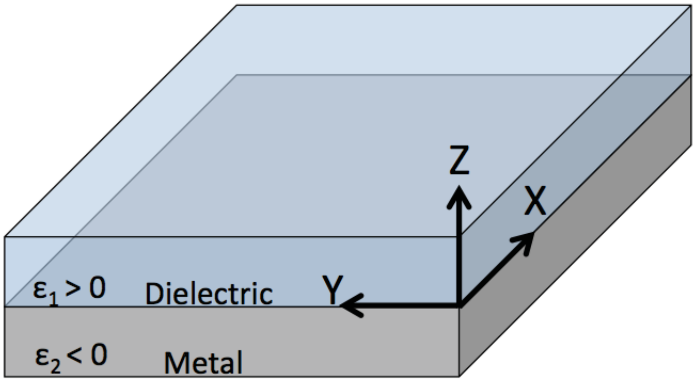

Fig. A.1. Metal / dielectric interface used for surface plasmon polariton excitation.

Let us first examine the TM mode of this wave with the geometry shown in Fig. A.1. In the region z > 0 (dielectric), we solve for this system first by finding the general solution for H_y, E_x, and E_z:

$$H_y = A_1 e^{i\beta x} e^{-k_1 z} \tag{A.1}$$

$$E_x = iA_1 \frac{k_1}{\omega \epsilon_1 \epsilon_0} e^{i\beta x} e^{-k_1 z} \tag{A.2}$$

$$E_z = -A_1 \frac{\beta}{\omega \epsilon_1 \epsilon_0} e^{i\beta x} e^{-k_1 z} \tag{A.3}$$

Likewise, in the region z < 0 (metal), we have:

$$H_y = A_2 e^{i\beta x} e^{-k_2 z} \tag{A.4}$$

$$E_x = -iA_2 \frac{k_2}{\omega \epsilon_2 \epsilon_0} e^{i\beta x} e^{-k_2 z} \tag{A.5}$$

$$E_z = -A_2 \frac{\beta}{\omega \epsilon_2 \epsilon_0} e^{i\beta x} e^{k_2 z} \tag{A.6}$$

It is important to note that the permittivities of the respective materials are not longer the permittivity of free space but include a relative permittivity term, which explains the electric fields interaction with the material. It is also important to note that the permittivity in the dielectric is positive, while the permittivity in the metal is negative. In these equations, we can see that the wave vector term (k_1, k_2) perpendicular to the metal / dielectric interface defines the exponential decay of the fields perpendicular to the interface essentially confining the field to the boundary of the two materials. Applying continuity of the fields H_y and ϵE_z at the boundary, and solving for these equations requires that $A_1 = A_2$ and

$$-\frac{k_2}{\epsilon_2} = \frac{k_1}{\epsilon_1} \tag{A.7}$$

This tells us that in order to have a propagating wave at this interface, one of the materials must have a positive permittivity (dielectric), while the other material must have a negative permittivity (metal). Furthermore, the magnetic field along the interface H_y must satisfy Eq. (A.8).

$$\frac{\delta^2 H_y}{\delta z^2} + (k_0 \epsilon_0 - \beta^2) H_y = 0 \tag{A.8}$$

Therefore,

$$k_1^2 = \beta^2 - k_0^2\epsilon_1 \tag{A.9}$$

$$k_2^2 = \beta^2 - k_0^2\epsilon_2 \tag{A.10}$$

Combining this result with Eq. (A.7), we arrive at what is known as the *"dispersion relation"* of the surface plasmon polaritons at the surface of the metal.

$$\beta = k_0\sqrt{\frac{\epsilon_1\epsilon_2}{\epsilon_1 + \epsilon_2}} \tag{A.11}$$

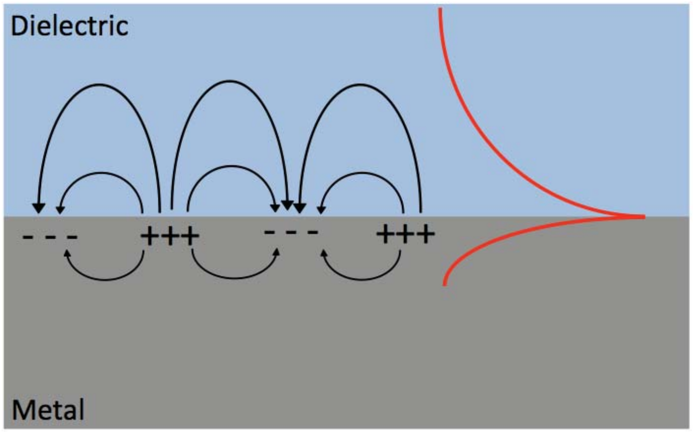

Fig. A.2. Surface Plasmon Polaritons (SPPs). Distribution of free charge carriers oscillating at the metal / dielectric boundary. The distribution of the SPP mode can be seen by the red curve.

The material acting as a metal in this case must exhibit a negative permittivity ($\epsilon < 0$). This condition is satisfied when the frequency of the incident field is below the *plasma frequency* ω_p where

$$\omega_p = \sqrt{\frac{ne^2}{\epsilon_0 m^*}} \tag{A.12}$$

In Eq. (A.12), n is the number of free electrons in the metal, e is the charge of the electron, and m^* is the effective mass of the electron in the metal. To re-emphasize, a surface wave can only exist in the condition where the permittivity of the metal is negative ($\epsilon_m < 0$), and this condition is satisfied at or below the materials plasma frequency.

A.1 Multilayer Systems and Plasmonic Waveguides

We have solved the wave equation for the case of a single metal / insulator interface, and now move on to look at three-layer systems consisting of metal- insulator-metal (MIM) and insulator-metal-insulator (IMI) structures. These structures can be used as plasmonic waveguides guiding this plasmonic mode confined to a subwavelength structure. In the IMI structure, when the thickness of the metal layer approaches the SPP decay length in the z-direction, a coupled mode will arise between the two interfaces as shown in Fig. A.3.

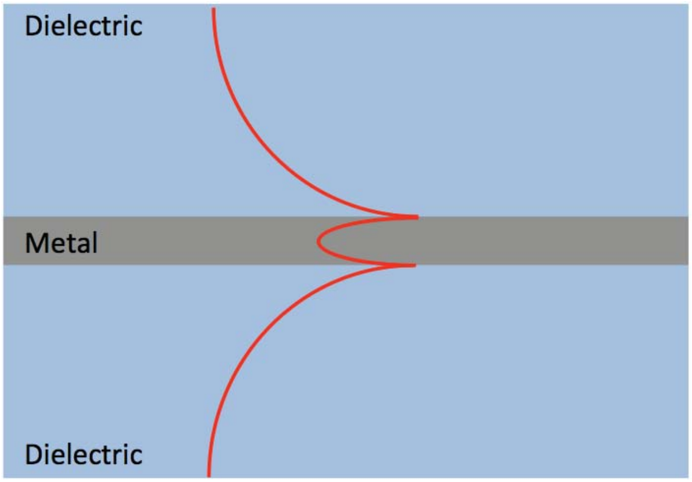

Fig. A.3. A coupled SPP mode will exist when the thickness of the metallic layer is below the decay length of the surface mode in an IMI structure.

This type of symmetric profile of the SPP mode will arise when the dielectrics have the same positive value of permittivity. These types of IMI structure have several important features worth noting. First, most of the propagating mode is not contained in the metal. For this reason, we say that the mode has weak confinement, and thus has the disadvantage of not being able to be steered well along the metal path. While this structure can be used as a waveguide, if the metal path changes direction, a large portion of the mode will not be able to follow this new path. Another disadvantage for such a structure is that in practical applications, it is desirable for these components to be grouped as densely as possible to fit more components onto a chip. Having such a mode that is spaced so far into the dielectric region prohibits such designs, as coupling to adjacent waveguides would typically produce undesirable results. However, because very little of the mode is contained within the metal, this type of structure has the advantage of very low losses for this propagating mode. While the evanescent field suffers no losses in the dielectric material, the permittivity of metals is a complex value, and must be described as:

$$\epsilon(\omega) = \epsilon' + i\epsilon'' \tag{A.13}$$

In Eq. (A.13), ϵ' describes the metals susceptibility to polarization, while the term ϵ'' describes losses in the metal. Because very little of the IMI mode is contained in the metal, it will suffer very little loss. For this reason, modes travelling in such a structure can propagate for very long distances, and are therefore known as Long Range Surface Plasmon Polaritons (LRSPP).

As previously mentioned, another type of structure can be used as a waveguide to propagate such SPPs. An alternative to the IMI structure is the metal-insulator-metal (MIM) structure shown below in Fig A.4.

Similar to the IMI structure, the MIM structure has a coupled mode between the two metal interfaces. However, in this case the metal interfaces have an insulating layer between them. As can be seen in Fig. A.4, most of the field in this MIM structure is in the metal layers. For this reason, this mode cannot propagate for long distances, as they suffer from the large losses in the metal. However, this mode is confined very well, and can thus easily follow the path of the waveguide.

By comparing these two types of waveguide designs, it can be seen that there are trade-offs to each design. For example, if an optical signal must be sent for a long distance in a straight line in a system that does not require high component density,

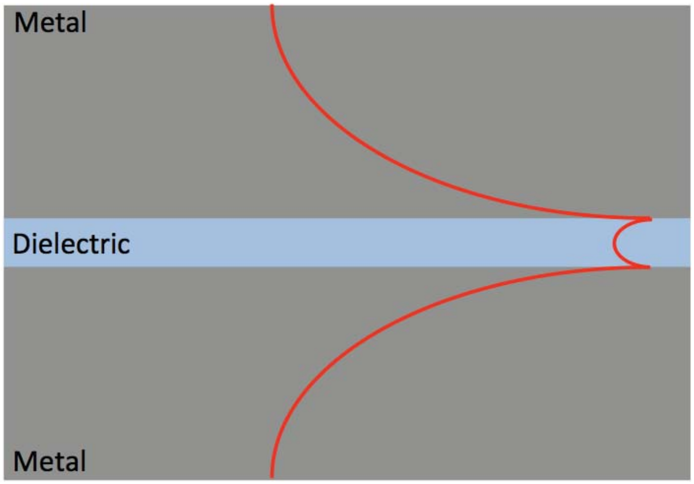

Fig. A.4. A coupled SPP mode in a MIM structure. While the mode is confined well, most of the field is in the metal, and will therefore suffer from the metallic losses.

the IMI structure is the clear choice. Alternatively, if the signal is only required to travel a short distance in a more dense system, the MIM structure may be the better choice. However, both structures have the advantage over conventional fiber optics in that they allow for subwavelength, nanometer confinement of the electromagnetic fields allowing for plasmonic integration with our current electronics.

A.2 Localized Surface Plasmon Resonance and Nano-Antennas

While the propagating mode of surface plasmon polaritons (SPPs) has been discussed, there is another type of surface plasmon known as localized surface plasmon resonance or LSPR. For this case, we consider a structure similar to the the IMI structure explained in the previous section, however we assume the metal now has a finite length such as shown below in Fig. A.5.

While in the case of the SPPs propagating on a boundary infinite in length, free charges were able to move for long distances under the influence of an oscillating field. However, when the length of this layer becomes finite, we see that under the influence of an oscillating electromagnetic wave, free charges will build up on the edges of these

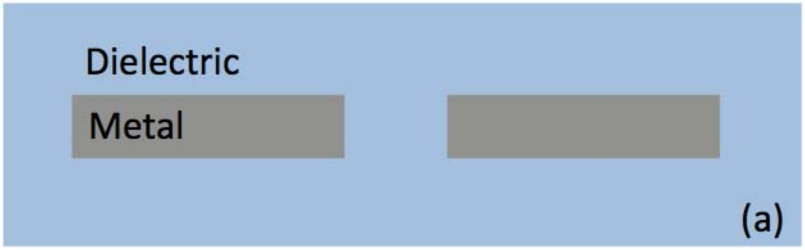

(a) The basic design of the structure.

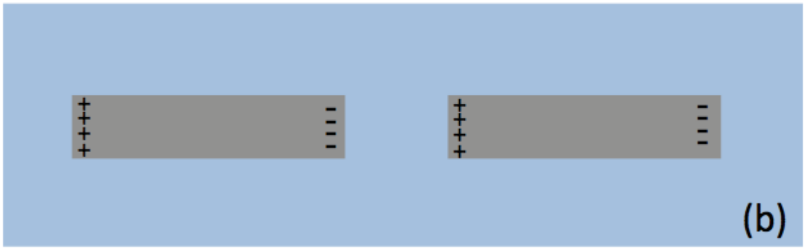

(b) The localization of charges due to the finite length of the structure.

Fig. A.5. Geometry of the localized surface plasmon resonance.

conducting metals. The incident electromagnetic wave acts as an Alternating Current (AC) source, oscillating the free charge carriers at optical frequencies. Naturally, this type of structure has a resonant frequency at which the metal pairs absorb the maximum amount of energy and confine it to the gap between metal pairs. For this reason, this type of structure is known as a nano-antenna and has a wide range of applications including enhancement of non-linear processes and improvements in solar cell efficiencies.

A.3 Conclusion

When a wave is incident on a dielectric / metal interface, our boundary conditions were able to identify the existence of a surface mode known as a surface plasmon polariton under TM polarization. However, due to losses in the metal to which these fields are confined, these fields will not propagate for long distances. To exploit this phenomenon into a practical application (such as a waveguide), the geometry can be configured into an IMI or MIM structure each with its own advantages and disadvantages. Finally, a similar technique can be used in a non-continuous structure to create a localized surface plasmon resonance which is a non-propagating mode but allows for the absorption and confinement of the field to a small volume. This type of structure can be used as a nano-antenna for various applications requiring strong field enhancement and confinement. Many of the Equations derived in this chapter, and structures discussed will have a great amount of application throughout the remainder of this dissertation.

B. GLANCING ANGLE DEPOSITION (GLAD) - NOVEL APPROACH FOR QUASI 3D FABRICATION

B.1 Glancing Angle Deposition at Purdue

B.1.1 Background

Due to the interest in creating films on non-planar surfaces and non-uniform thicknesses, we have ordered a custom designed and built Electron-Beam (e-beam) Evaporation system from PVD Products (Wilmington, MA). The system's installation was completed in February 2012, and is located in the cleanroom of the Birck Nanotechnology Center. An image of the outside of the system can be seen in Fig. B.1. While Birck has several other e-beam evaporators, this PVD GLAD system has control over the substrate's angle and rotation that make it unique to any of the other evaporation systems on Purdue's campus. Additionally, the system's deposition parameters (deposition rate, thickness) can be programmed to automate the deposition process for many-layered films.

B.1.2 Hardware

The evaporator has a four-pocket turret, and the deposition angle can be automatically controlled for each pocket. The rotational control of the substrate can be set to rotate continuously at a designated rate (RPM), or can be set to do a single angular rotation (e.g. rotate clockwise 90°) through the computer's user interface (discussed later). The valve control for loading/unloading the chamber are all manually controlled and are located on the left side of the evaporation chamber (shown in Fig. B.1). Base pressures of 5×10^{-6} can be reached in approximately 1 hour, while pressures of 2×10^{-8} Torr can be achieved by letting the cryo pump run for approximately 24 hours.

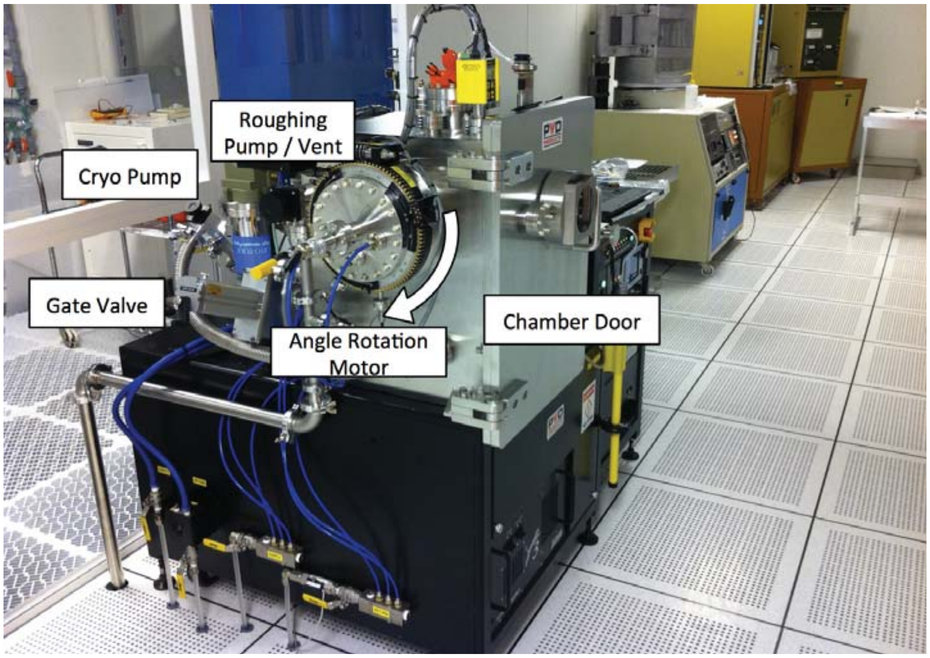

Fig. B.1. Some of the external components of the GLAD system

The inside of the evaporation chamber can be seen in Fig. B.2. While most of the internal components are standard to most e-beam evaporators, the sample holder and quartz crystal monitors (QCM) are slightly modified at should be explained in detail. The sample holder's angle can be controlled via the computer's user interface (discussed later). The motor for the angular control of the substrate is located outside the chamber, as seen in Fig. B.1, while the motor for the sample's rotational control is located internally. One of the design requirements of the GLAD system was the capability to deposit large amounts of material in a single deposition without breaking vacuum, and the system was designed accordingly. First, pockets for very large (30cc) crucibles were included to accommodate the large volume of deposited material. Secondly, because QCMs are extremely sensitive to (and deteriorate with) the amount of deposited mass, the system has two separate QCMs with independent shutters that can be opened and closed when one QCM has deteriorated. These internal components allow for long depositions of thick and multi-layered films without breaking vacuum.

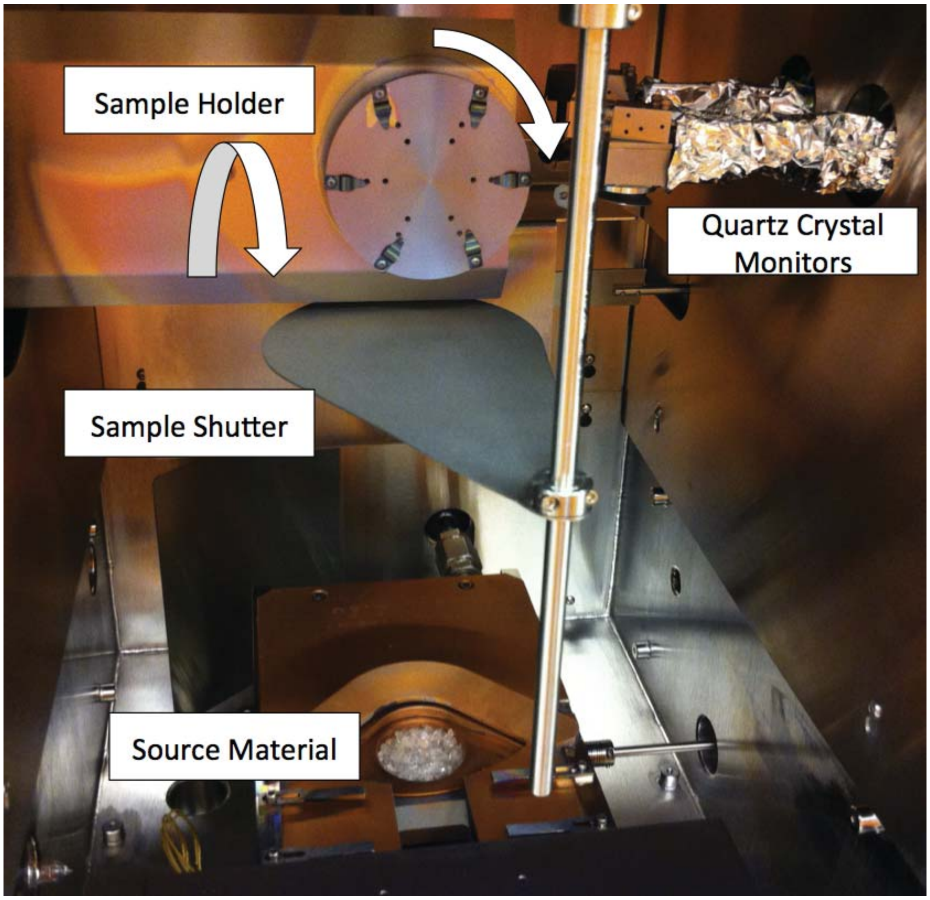

Fig. B.2. Some of the internal components of the GLAD system

The current materials in the chamber, and their respective pocket numbers are listed below:

1. Germanium (Ge)
2. Silver (Ag)
3. Silicon Dioxide (SiO_2)

Other materials that can be evaporated in the chamber (though they are not loaded) include but are not limited to:

- Aluminum (Al)
- Aluminum Oxide (Al_2O_3)
- Gold (Au)
- Chromium (Cr)
- Silicon (Si)
- Copper (Cu)
- Titanium Dioxide (TiO_2)
- Iron (Fe)

B.1.3 Automation and Computer User Interface

In order to automate the deposition of thick and multi-layered films, as well as the sample's angle and rotation, many of the system's controls can be manipulated through an external computer. Physically located next to the evaporation chamber, a laptop controls the sample's motion through a Graphical User Interface (GUI), programmed in LabView. A screenshot of this GUI, along with important controls are shown in Fig. B.3.

The bottom left box A: "Rotation Control" controls the substrates rotation. There are two basic methods of oration: 1) continuously rotating at a specified rate (RPM), or 2) rotating by an exact amount (e.g. 90°) and stopping. The rotation is done by a stepper motor, where full 360° rotation requires 20,000 steps. Therefore, 180° rotation is 10,000 steps and so forth.

The system has a 4-pocket turret, where the angle of deposition for each pocket can be independently controlled. The designated angle foe each pocket is input into box B: "Angle Control". The angles are input as degrees (not radians), and are applied to the substrate when the "Set Index Positions" button is clicked. The angle of the substrate will change only when the source material in the corresponding pocket is being evaporated.

Because the system is designed to evaporate very thick (microns) and multilayer films, the computer can save critical system information throughout the entire deposition process. This information includes chamber pressure, deposition rate, film thickness, substrate angle rotation, and so on. This data is saved in a plan-text comma separated value (CSV) format, and its collection time interval can be assigned in Box C: "System Data Collection". More detailed instructions on loading/unloading the chamber can be found in Appendix C.1 "Loading and Unloading the GLAD Chamber"

B.1.4 WORDS OF CAUTION

The systems' automation is a wonderful and essential feature for fabricating thick and many-layered structures. Depositing many-layered films can take very long amounts of time (some of the structures fabricated in this dissertation have taken in excess of 24 hours to deposit). Automating this process allows the machine to continue deposition without input from the user. However, this feature can lie users into a false sense of security, so words of caution should be considered.

Although unlikely, there are several possible problems that can arise which could lead to catastrophic system failure and destruction. A magnet failure is unlikely but unpredictable. In the case of this event, the high-powered electron beam will go off in an arbitrary direction, and can burn or melt through whatever it comes in contact. This could burn a hole in the chamber itself and/or damage any internal components in quite a short time period. The only way to catch this problem is to be present and observant during deposition. Another possible (though avoidable) problem that could arise is burning through a crucible and turret with the e-beam. This potential problem is espycially apparent with dielectric materials, as they do not "pool" like metals. This problem can be avoided by making sure the crucibles are always full, and using proper sweeping.

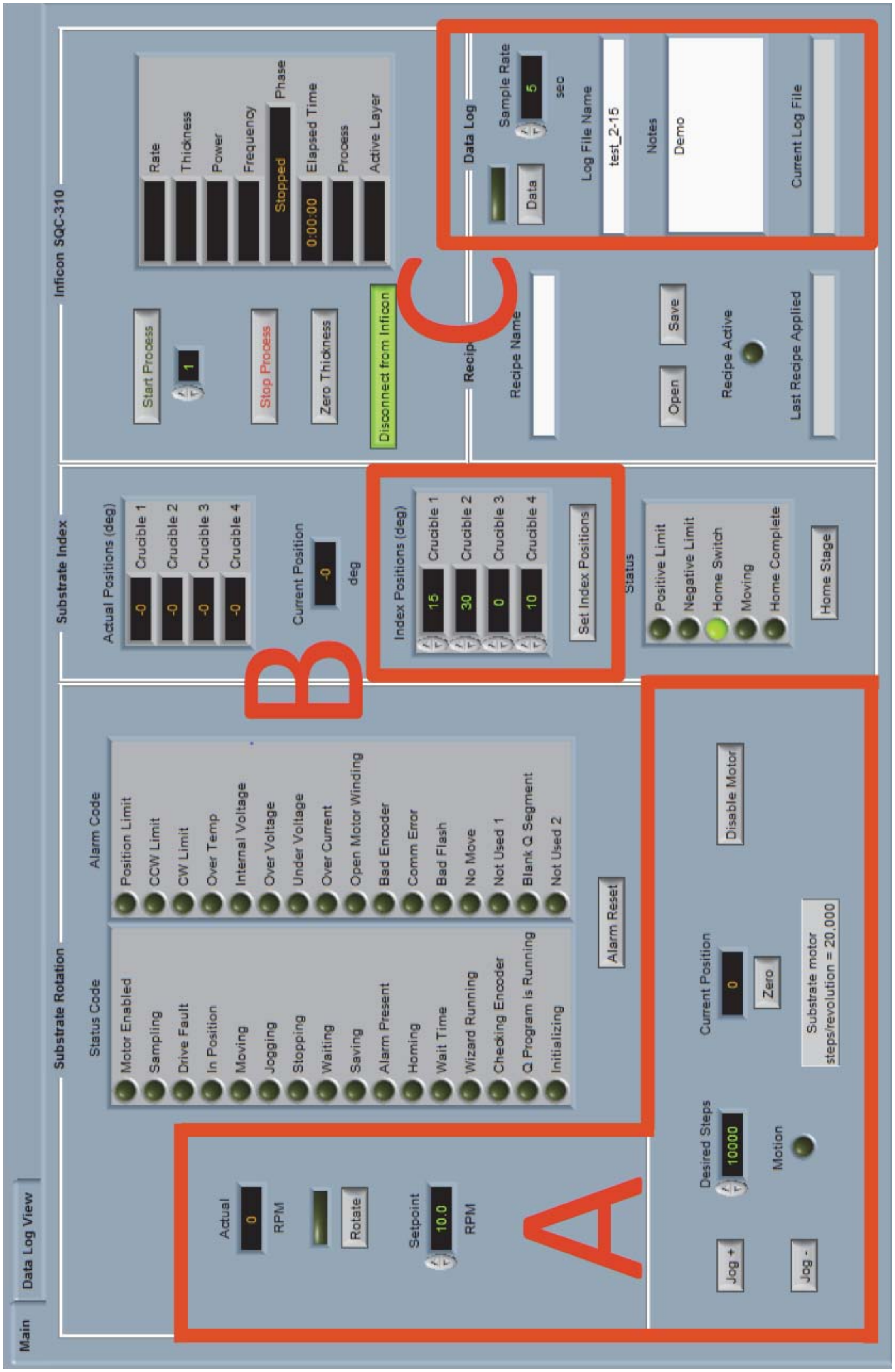

Actual: 0 RPM

Setpoint: 10.0 RPM

Desired Steps: 10000

Current Position: 0

Substrate motor steps/revolution = 20,000

Actual Positions (deg): Crucible 1: -0; Crucible 2: -0; Crucible 3: -0; Crucible 4: -0

Current Position: -0 deg

Index Positions (deg): Crucible 1: 15; Crucible 2: 30; Crucible 3: 0; Crucible 4: 10

Phase: Stopped

Elapsed Time: 0:00:00

Sample Rate: 5 sec

Log File Name: test_2-15

Notes: Demo

Fig. B.3. Screenshot of the GUI for the GLAD system.

C. STEP-BY-STEP INSTRUCTIONS FOR OPERATING GLAD

C.1 Loading and Unloading the GLAD Chamber

1. Turn off ion gauge and wait 2 minutes for it to cool
2. Close the gate valve fully
3. Open the vent valve, wait for pressure to reach 760 Torr
4. The chamber door is difficult to open. Either wait a while ($\sim$ 10 minutes) then open the door, or pull VERY hard on the door to open.
5. While the chamber is open, *double glove* and check the turret pockets have sufficientt material, chamber is clean, Quartz Crystal Monitors are in good health (above $\sim$80%)
6. The sample holder is friction-mounted in the chamber. There are two Allen wrenches on top of the chamber. Use the larger wrench to loosen the 2 screws while holding the sample holder with the other hand. Be careful not to drop the sample holder! I find the whole process is easier when the holder is rotated to 45°.
7. Mount the sample into the sample holder using the smaller Allen wrench. Tip: think ahead of time about where the shadow from the sample clips will fall - especially at clanking angles (as it will cast a long shadow).
8. Remount the sample holder as before. Be sure it is tightly secured before releasing with your hand - as to not let it fall down. Shake the sample holder slightly so as to make sure it is securely mounted and will not fall down on its own. Again, make note of the orientation of the sample and consider any shadowing from the mounting clips.

9. Close the chamber, tighten acre-mount on the side of the chamber (to make a tight seal).
10. Close the vent valve
11. Open the roughing valve, wait for pressure to drop down to below 250mTorr (0.250) Torr
12. Close the roughing valve
13. SLOWLY open the gate valve. Once the pressure begins to drop, wait 1 minute, then continue opening the valve slowly. Once the pressure is below $\sim$1e^{-4} Torr, open the valve up all the way and let the system pump down.
14. Wait $\sim$5 minutes to let the system drop in pressure.
15. Turn on the ion gauge, record the pressure in the logbook
16. Wait $\sim$1 hour for the pressure to drop to 5e^{-6} Torr
17. Wait $\sim$24 hours for the pressure to drop to 5e^{-8} Torr

C.2 Running an Evaporation

1. Turn on High Voltage switch and controller switch (bottom left - below the chamber)
2. Turn on the “Sweep Controller” switch
3. Turn on the “Evap Enable” switch and wait for $\sim$2 minutes for the light to stop blinking.
4. On the Inficon thin film deposition controller, go into the process menu to select and edit a recipe. Here, film layers can be added or removed and parameters (such as film thickness and deposition rate) can be modified.
5. Go back to the main menu, be sure the correct recipe has been selected.
6. Start the process.

7. The sample angle for the 4 crucibles can be input into the “Index Positions” box on the computer.
8. When the process finishes, turn the system off in the reverse order: evap enable, sweep controller, high voltage, and controller.
9. Make sure the ion gauge is turned off and wait 2 minutes for it to cool before venting.

C.3 Other Notes and Comments

- Get all source materials from the BNC staff (namely Dave Lubelski or Kenny Schwartz)
- The “chimney” will need to be cleaned periodically, as pieces of deposited material will flake off. Take the chimney out and scrape it with a razor blade. If further cleaning is needed, Dave Lubelski can clean it with a sandblaster.
- Clean and vacuum any material that has fallen in the chamber - especially if it is near any source crucibles.
- Keep the chamber clean! Ask BNC staff before putting any new materials inside the chamber.
- We installed a plastic shield on the outside of the chamber around the substrate angle rotation motor. This is there for safety and should never be removed. it is a “pinch-point” and can crush a person’s fingers.
- Never open any of the High-Voltage boxes - they are an electric hazard and can be lethal

VITA

VITA

Paul R. West currently works for Intel Semiconductor Manufacturing Company - Portland Technology Development as a Defect Metrology Yield Engineer in Hillsboro, Oregon. He specializes in the design and fabrication of optical materials, with emphasis on detecting and imaging of subwavelength objects. He graduated with a B.S.E.E. from Michigan Technological University in 2008, and Ph.D. from Purdue University in 2014. His primary advisors at Purdue are Dr. Alexandra E. Boltasseva and Dr. Vladimir M. Shalaev.